TUDelft

Delft University of Technology

Revealing hidden patterns

A study on ice shelf basal melting

Zinck, A.P.

Important note
To cite this publication, please use the final published version (if applicable).
Please check the document version above.

Revealing hidden patterns

A study on ice shelf basal melting

Ann-Sofie Priergaard Zinck

Revealing hidden patterns

A study on ice shelf basal melting

Ann-Sofie Priergaard Zinck

Revealing hidden patterns
A study on ice shelf basal melting

Dissertation

for the purpose of obtaining the degree of doctor
at Delft University of Technology
by the authority of the Rector Magnificus prof. dr. ir. T.H.J.J. van der Hagen,
chair of the Board for Doctorates,
to be defended publicly on Tuesday 3 June 2025 at 15:00 o'clock

by

Ann-Sofie Priergaard ZINCK

Master of Science in Physics, University of Copenhagen, Denmark
born in Odense, Denmark

This dissertation has been approved by the promoters.

Composition of the doctoral committee:

Rector Magnificus	chairperson
Prof. Dr.-Ing. habil. R. Klees	Delft University of Technology, promotor
Dr. S. L. M. Lhermitte	Delft University of Technology, promotor
Dr. ir. B. Wouters	Delft University of Technology, copromotor

Independent members:

Prof. dr. ir. H. W. J. Russchenberg	Delft University of Technology
Prof. dr. A. Wåhlin	University of Gothenburg
Prof. dr. L. S. Sørensen	Technical University of Denmark
Prof. dr. M. R. van den Broeke	Utrecht University
Prof. dr. S. C. Steele-Dunne	Delft University of Technology, reserve

iv

In the memory of Henning:
The best physics teacher ever!

Kære Henning,

Der lød rygter i byen om, at der på Tornbjerg Gymnaisum skulle være en total skør og fantastisk fysiklærer, og disse rygter fik mig til at vælge Tornbjerg. Aldrig har jeg mødt et mere inspirerende menneske end dig, og uden din indflydelse var jeg nok aldrig gået præcist den her vej. I starten af gymnasietiden var jeg overbevist om, at jeg skulle være meteorolog, men du viste mig hurtigt magien af glaciologiens verden. Du gav mig mulighed for at fordybe mig i Mars' iskappe og lånte mig en bog, som har vist sig at skulle følge mig siden da: *The Physics of Glaciers*. Du hjalp mig ikke bare med at finde min egen vej indenfor fysikken, men du hjalp også mig og alle mine klassekammerater til en sjovere hverdag igennem en 3 år lang Mat-Fys gymnasietid ved at være skolens rebellærer! Du organiserede dårlig-film-festivaler udenfor skolens lukketid i hemmeligt samarbejde med pedellen. Du tvang os til at spise nightmare hotdogs (hindbærroulade med pølse fra glas og karryketchup), inden vi kunne rykke op i 2.g. Du overbeviste os om, at man kun var værdig til at gå videre i 3.g, hvis man kunne åbne en øl ved hjælp af en anden øl. Du fik os til at dræbe utallige lemminger igennem dine hjemmelade fysikbøger og -opgaver, hvor du måske ikke altid havde regnet efter, om lemmingerne ville overleve at passere en lavvandet flod fyldt med lumske dæmninger.

Jeg savner dig - Tak for alt!

Contents

Summary

The floating extent of the Antarctic Ice Sheet – the ice shelves – play a critical role in stabilizing the ice sheet through a process known as buttressing. This effect slows the flow of grounded ice into the ocean and thereby helps regulating the ice sheet's sea level rise contribution. However, ice shelves are highly sensitive to (climate-driven) changes, which can cause thinning and structural weakening. This, in turn, can diminish their stabilizing influence and accelerate ice loss from the ice sheet. Given Antarctica's vast potential to contribute to sea level rise, understanding the processes affecting ice shelf stability is essential for predicting future changes and reducing associated uncertainties.

Ocean-driven melting at the base of an ice shelf significantly influences its stability by driving ice thinning, grounding line retreat, and through basal channel formation. These channels, formed by meltwater plumes carving pathways along the ice base, are shaped by ice draft geometry, ocean dynamics and temperature. Basal channels concentrate melting and can weaken ice shelves by acting as structural weak points and promoting fractures that may lead to calving and retreat. On the other hand, basal channels can also stabilize ice shelves by localizing melt, potentially reducing overall thinning. Their evolution – including changes in size, location, and intensity of melting – is influenced by changes in ice flow and the availability and temperature of circumpolar deep water, which is expected to increase under climate change. Understanding basal channels and their role in ice shelf (in)stability is thus essential for accurately assessing the future behavior of the Antarctic Ice Sheet and its contributions to sea level rise.

In this thesis a method for detecting basal melting at high spatial resolution, called BURGEE (Basal melt rates Using REMA and Google Earth Engine), was developed and described in Chapter 2. BURGEE combines stereo-imagery from the Reference Elevation Model of Antarctica (REMA) with CryoSat-2 elevation data to obtain high-resolution ice shelf elevation changes, which through a mass conservation approach can be translated into basal melt rates. BURGEE's 50 m posting allows for capturing detailed melt patterns previously unresolved in coarser remote sensing products. Applied to the Dotson Ice Shelf, BURGEE revealed spatial variability within a major melt channel, influenced by a pinning point that affects ocean plume pathways. This method was developed to be scalable allowing for applications to other ice shelves to better understand ice shelf melt dynamics and stability across several ice shelves.

Using BURGEE in Chapter 3, high-resolution basal melt maps revealed that melt rates

within ice shelf channels have been underestimated by 42-50% in products relying on altimetry-only. This underestimation has a significant impact on ice shelf stability assumptions, for which channel breakthrough times can be used as a proxy. As breakthrough times are highly controlled by the melt rate within the channels, these altimetry-only studies also significantly underestimate the time it would take for a channel to break through. While so far channels have not been observed to actually break through, they have been observed to cause significant fracturing once they reach a thin and vulnerable state. Channel-induced fracturing has further been observed to lead to ice shelf calving and retreat. The faster-than-previously-assumed channel breakthrough times – and thus weakening – exacerbates the vulnerability of ice shelves to channelized melting and consequent fracturing and retreat. Incorporating basal melting at high resolution into ice-sheet and ocean models is thus crucial for improving projections of ice shelf stability and global sea level rise.

In Chapter 4, BURGEE has further revealed sudden changes within the basal channel system on George VI Ice Shelf, marked by a 23 m surface lowering over just nine years. This rapid development coincided with increased ocean temperatures and salinity during the 2015 El Niño event, highlighting the influence of large-scale climate patterns on basal melting. The high resolution further revealed subtle shifts in ice flow indicative of fracturing, suggesting a combined weakening effect from basal melting and structural integrity causing changes and possible re-routing of the channel system. Such findings underscore the importance of monitoring dynamic ice shelf channels at a high resolution to better understand and predict their role in ice shelf weakening.

Together, these findings represent a significant advancement in our understanding of basal melting and its impact on ice shelf stability. This thesis has provided the tools and insights needed to detect, quantify, and analyze the spatial variability of basal melting at high spatial resolution. By uncovering the underestimation of channelized melting, identifying key drivers of channel evolution, and linking these processes to ice shelf weakening and retreat, this work has filled critical knowledge gaps. It emphasizes the importance of high-resolution observations and models in capturing the complex interactions between ocean dynamics, basal melting (especially within channels), and ice shelf integrity.

Samenvatting

De drijvende delen van de Antarctische ijskap – de ijsplaten – spelen een cruciale rol in het stabiel houden van de ijskap doordat ze de ijskap als het ware stutten. Dit effect vertraagt de stroming van landijs naar de oceaan en helpt zo het aandeel van de ijskap in de zeespiegelstijging te reguleren. IJsschotsen zijn echter zeer gevoelig voor (klimaatgedreven) veranderingen, die kunnen leiden tot dunner worden en structurele verzwakking. Dit kan vervolgens leiden tot een verminderde stabiliserende invloed en een versneld ijsverlies van de ijskap. Gezien het enorme potentiele aandeel van Antarctica in de zeespiegelstijging, is het begrijpen van de processen die de stabiliteit van de ijskappen beïnvloeden essentieel voor het voorspellen van toekomstige veranderingen en het verminderen van de bijbehorende onzekerheden.

Het smelten van ijs aan de onderkant van een ijsplaat beïnvloedt de stabiliteit ervan aanzienlijk doordat het ijs dunner wordt, de ijslijn zich terugtrekt en door de vorming van kanalen aan de onderkant van de ijsplaat. Deze kanalen, die gevormd worden door smeltwaterpluimen die hun weg vinden langs de onderkant van het ijs, worden bepaald door de geometrie van de ijskappen, de oceaandynamica en de oceaantemperatuur. De kanalen concentreren het smelten en kunnen de ijsplaten verzwakken doordat ze fungeren als structurele zwakke punten waardoor scheuren ontstaan die kunnen leiden tot afkalving van een ijsplaat. Anderzijds kunnen de kanalen ijsplaten ook stabiliseren door smelt te lokaliseren, waardoor de algehele verdunning mogelijk afneemt. De ontwikkeling van deze kanalen – inclusief veranderingen in grootte, locatie en intensiteit van het smelten – wordt beïnvloed door veranderingen in de ijsstroming en de aanwezigheid en temperatuur van circumpolair diep water, dat naar verwachting zal toenemen onder invloed van klimaatverandering. Om het toekomstige gedrag van de Antarctische ijskap en de bijdrage ervan aan de zeespiegelstijging nauwkeurig te kunnen voorspellen, is het dus van essentieel belang om de kanalen aan de onderkant van ijsplaten en hun rol in de (on)stabiliteit van de ijskappen te onderzoeken.

In dit proefschrift is in hoofdstuk 2 een methode ontwikkeld genaamd BURGEE (Basal melt rates Using REMA and Google Earth Engine) voor het detecteren van het smelten van de onderkant van ijskappen met een hoge ruimtelijke resolutie. BURGEE combineert stereobeelden van het referentiehoogtemodel van Antarctica (REMA) met CryoSat-2 hoogtedata om hoogteveranderingen van de ijsplaten met een hoge resolutie te bepalen, die via een benadering van massabehoud kunnen worden vertaald naar de hoeveelheid smeltwater op de ijsbodem. BURGEE's 50 m resolutie maakt het mogelijk

om gedetailleerde smeltpatronen in kaart te brengen die voorheen niet konden worden waargenomen met grovere remote sensing data. Wanneer BURGEE wordt toegepast op de Dotson Ice Shelf, wordt ruimtelijke variabiliteit zichtbaar binnen een belangrijk smeltkanaal, dat wordt beïnvloed door een 'pinning point' dat de routes van oceaanpluimen beïnvloedt. De methode is zo ontwikkeld dat deze schaalbaar is en kan worden toegepast op andere ijskappen om de smeltdynamiek en stabiliteit van ijskappen op meerdere ijsplaten beter te begrijpen.

In hoofdstuk 3 liet BURGEE zien dat de smeltsnelheden binnen de kanalen van de ijsplaten met 42-50% worden onderschat in producten die alleen op hoogtemeting zijn gebaseerd. Deze onderschatting heeft een significante invloed op de aannames over de stabiliteit van de ijsplaten, waarvoor de doorbraaktijden van de kanalen als een benadering kunnen worden gebruikt. Aangezien de doorbraaktijd sterk bepaald wordt door de smeltsnelheid binnen de kanalen, onderschatten de studies op basis van uitsluitend hoogtemeting ook aanzienlijk de tijd die een kanaal nodig heeft om door te breken. Hoewel er tot nu toe nog niet is waargenomen dat kanalen daadwerkelijk doorbreken, is wel waargenomen dat ze aanzienlijke scheurvorming veroorzaken wanneer ze eenmaal dun en kwetsbaar zijn. Verder is waargenomen dat door kanalen veroorzaakte breuk leidt tot het afkalven en terugtrekken van de ijsplaat. De snellere doorbraaktijden van de kanalen - en dus de verzwakking ervan - dan eerder werd aangenomen, verergert de kwetsbaarheid van ijsplaten voor gekanaliseerd smelten en de daaropvolgende scheurvorming en terugtrekking. Het opnemen van het smelten van de ijsbodem met hoge resolutie in ijskap- en oceaanmodellen is dus cruciaal voor het verbeteren van projecties van de stabiliteit van ijskappen en de wereldwijde zeespiegelstijging.

In hoofdstuk 4 toont BURGEE daarnaast plotselinge veranderingen binnen het kanaalsysteem onder de George VI ijsplaat, die in slechts negen jaar tijd 23 m verlaagd is aan het ijsoppervlak. Deze snelle ontwikkeling viel samen met verhoogde oceaantemperaturen en zoutgehalte tijdens de El Niño-gebeurtenis in 2015, waardoor de invloed van grootschalige klimaatpatronen op het smelten van de ijsbodem duidelijk werd. De hoge resolutie onthulde verder subtiele verschuivingen in de ijsstroom die duiden op breuken, wat suggereert dat een combinatie van verzwakking door afsmelting van de ijsbodem en structurele integriteit voor veranderingen en mogelijke omlegging van het kanaalsysteem zorgt. Dergelijke resultaten benadrukken het belang van het monitoren van de dynamiek van ijskanalen met een hoge resolutie om hun rol in het verzwakken van de ijsplaat beter te begrijpen en te voorspellen.

Deze bevindingen vormen samen een belangrijke stap voorwaarts in ons begrip van het smelten van de ijsbodem en de invloed ervan op de stabiliteit van ijsplaten. Deze dissertatie heeft de instrumenten en de inzichten opgeleverd die nodig zijn om de ruimtelijke variabiliteit van het smelten van de ijsbodem te detecteren, kwantificeren en analyseren met een hoge ruimtelijke resolutie. Door onderschatting van gekanaliseerd smelten aan het licht te brengen, de drijvende krachten van gekanaliseerde smelt te identificeren en deze processen te koppelen aan verzwakking en terugtrekking van de ijsplaat, heeft dit werk kritieke gaten in onze kennis gevuld. Dit werk benadrukt het belang van hoge-resolutie observaties en modellen voor het vastleggen van de complexe interacties

tussen oceaandynamica, afsmelting van de ijsplaten (vooral in kanalen) en de stabiliteit van de ijskappen.

This summary was translated to Dutch by Sophie de Roda Husman.

Résumé

De flydende dele af den antarktiske iskappe – ishylderne – spiller en afgørende rolle
i at opretholde iskappens stabilitet, da de fungerer som støtte og bremser strømmen
af indlandsisen mod havet. Denne effekt hjælper dermed med at regulere iskappens
bidrag til havniveaustigninger. Dog er ishylderne meget følsomme over for (klimadrevne)
ændringer, som kan føre til udtynding og strukturel svækkelse. Dette kan mindske deres
stabiliserende effekt og accelerere istab fra iskappen. I betragtning af Antarktis' enorme
potentielle bidrag til havniveaustigninger er det afgørende at forstå de processer, der
påvirker ishyldernes stabilitet, for at kunne forudsige fremtidige ændringer og mindske
dertilhørende usikkerheder.

Smeltning af is på undersiden af en ishylde påvirker i dens stabilitet betydeligt ved at
forårsage udtynding, tilbagetrækning af grounding-linjen og dannelsen af kanaler under
ishylden. Disse kanaler, som skabes af smeltevandsstrømme, der løber langs undersiden
af isen, formes af isens geometri, oceanets dynamik og vandtemperaturen. Kanalerne
koncentrerer smeltningen og kan svække ishylderne ved at fungere som strukturelle
svage punkter, hvor sprækker kan opstå, hvilket kan føre til kælving og tilbagetræk-
ning. Omvendt kan kanalerne også stabilisere ishylderne ved at lokalisere smeltning,
hvilket muligvis reducerer den samlede udtynding. Kanalernes udvikling – herunder
ændringer i størrelse, placering og smelteintensitet – påvirkes af ændringer i isflydning
samt forekomsten og temperaturen af det cirkumpolare dybvand, som forventes at stige
som følge af klimaforandringer. For at kunne forudsige den fremtidige evolution af den
antarktiske iskappe og dens bidrag til havniveaustigninger med større præcision, er det
derfor afgørende at undersøge kanalerne under ishylderne og deres rolle i ishyldernes
(u)stabilitet.

I denne afhandling blev der i kapitel 2 udviklet en metode med høj rummelig opløs-
ning, kaldet BURGEE (Basal melt rates Using REMA and Google Earth Engine), til
at kortlægge smeltningen på undersiden af ishylder. BURGEE kombinerer stereo-
billeder fra Reference Elevation Model of Antarctica (REMA) med CryoSat-2 højde-
data for at beregne ændringer i ishyldens højde med høj opløsning, som via princip-
per om massebevarelse kan omdannes til smeltevandsmængder af ishyldernes under-
side. BURGEE's 50 m opløsning muliggør detaljeret kortlægning af smeltemønstre, der
tidligere ikke kunne observeres med remote sensing data af grovere opløsning. Ved
at anvende BURGEE på Dotson-ishylden, blev det tydeliggjort at smeltemønstret i en
vigtig smeltekanal bliver påvirket af et "pinning point" som omdirigerer havstrømmene.

Metoden, BURGEE, er designet til at være skalerbar og kan anvendes på andre ishylder og dermed hjælpe med en bedre forståelse af dynamikken bag ishyldernes smeltning og stabilitet.

I kapitel 3 viste bruge af BURGEE, at smelteraterne inden for ishyldekanaler undervurderes med 42-50% i produkter, der kun er baseret på højdemålinger. Denne undervurdering har en betydelig indvirkning på antagelser om ishyldernes stabilitet, hvor kanalernes gennembrudstid kan bruges som en indikator. Da gennembrudstiden er stærkt påvirket af smelteraterne i kanalerne, undervurderer studier, der udelukkende er baseret på højdemålinger, også væsentligt den tid, det tager for en kanal at bryde igennem. Selvom det endnu ikke er blevet observeret, at kanaler rent faktisk bryder igennem, er det dokumenteret, at de forårsager betydelig dannelse af sprækker, når de først er tynde og sårbare. Det er desuden blevet observeret, at sprækker forårsaget af kanaler fører til kælving og tilbagetrækning af ishylderne. De hurtigere end tidligere antagede gennembrudstider for kanaler – og dermed svækkelse – forstærker ishyldernes sårbarhed over for kanaliseret smeltning og efterfølgende sprækdannelse og tilbagetrækning. Derfor er det afgørende at integrere bundsmeltning af ishylder i høj opløsning i is- og havmodeller for at forbedre prognoserne af ishyldernes stabilitet og globale havniveaustigninger.

I kapitel 4 afslørede BURGEE desuden pludselige ændringer i kanalsystemet under George VI-ishylden, hvor overfladehøjden er sunket med 23 m på blot ni år. Denne hurtige udvikling faldt sammen med højere havtemperaturer og saltholdighed under El Niño-hændelsen i 2015, hvilket fremhæver hvordan storskala klimamønstre påvirker bundsmeltning af ishylder. Den høje opløsning afslørede desuden mindre ændringer i isflydningen, et tegn på begyndende sprækker, hvilket tyder på at en kombinerende svækkende effekt fra både bundsmeltning og strukturel integritet er skyld i ændringerne og i mulig omdirigering af kanalsystemet. Disse resultater understreger vigtigheden af at overvåge kanalernes dynamik med høj opløsning for bedre at forstå og forudsige deres rolle i ishyldernes svækkelse.

Sammen repræsenterer disse fund et vigtigt skridt fremad i vores forståelse af bundsmeltning og dens indvirkning på ishyldernes stabilitet. Afhandlingen har leveret værktøjer og indsigt, der er nødvendige for at opdage, kvantificere og analysere bundsmeltning med høj rumlig opløsning. Ved at påpege undervurderingen af kanaliseret smeltning, identificere drivkræfterne bag kanaliseret smeltning og forbinde disse processer til svækkelse og tilbagetrækning af ishylderne, har denne afhandling udfyldt kritiske videnshuller. Det fremhæver vigtigheden af højopløselige observationer og modeller for at fange de komplekse interaktioner der er mellem havdynamik, bundsmeltning (især i kanaler) og ishyldernes stabilitet.

$$\frac{DH}{Dt} = -H(\nabla \cdot \bar{u}) + \dot{M}_s - \dot{M}_b$$

Chapter 1

Introduction

1.1 Sea level rise

Since the 1970s, global mean sea level has been rising at an average rate of 2.33 mm/yr (1.55 mm/yr to 3.12 mm/yr), driven by both natural and anthropogenic factors (IPCC, 2023). Human activities, particularly those contributing to increased global temperatures, play a significant role in sea level rise through ocean thermal expansion, the melting of the cryosphere (ice sheets and glaciers), and changes in land water storage (IPCC, 2023). Both temperature and sea level are rising at an accelerating rate (IPCC, 2023), and it is concerning that the Greenland and Antarctic ice sheets alone contain enough freshwater to raise sea levels by approximately 7 meters (Morlighem et al., 2017) and 58 meters (Fretwell et al., 2013), respectively.

The regional implications of rising sea levels are largely determined by the processes driving this change (Fig. 1.1, Pattyn and Morlighem, 2020; van de Wal et al., 2022). Currently, the two primary contributors to sea level rise are thermal expansion and the melting of glaciers and ice sheets, which contribute approximately 1.39 mm/yr (0.74 mm/yr to 2.05 mm/yr) and 1.62 mm/yr (1.32 mm/yr to 1.92 mm/yr), respectively, with the cryosphere representing the main driver (IPCC, 2023). While the Antarctic Ice Sheet is the largest freshwater reservoir, the Greenland Ice Sheet currently leads cryospheric contributions, adding around 0.63 mm/yr (0.51 mm/yr to 0.74 mm/yr) to sea level rise, followed by the Antarctic Ice Sheet at 0.37 mm/yr (0.24 mm/yr to 0.50 mm/yr), and glaciers at 0.62 mm/yr (0.57 mm/yr to 0.68 mm/yr) (IPCC, 2023). However, this trend may shift in the future. Under certain climate scenarios, the Antarctic Ice Sheet is projected to become the dominant cryospheric contributor (Fig. 1.1, IPCC, 2023), with the potential to drive over 1 meter of global sea level rise by the century's end, a low-probability yet high-impact outcome (Fig. 1.2, IPCC, 2023). Reducing uncertainties in the timing and magnitude of Antarctic-driven sea level rise is crucial for global and coastal communities alike (Pattyn and Morlighem, 2020).

Projected Sea Level Change Contributions under SSP1-2.6 and SSP5-8.5
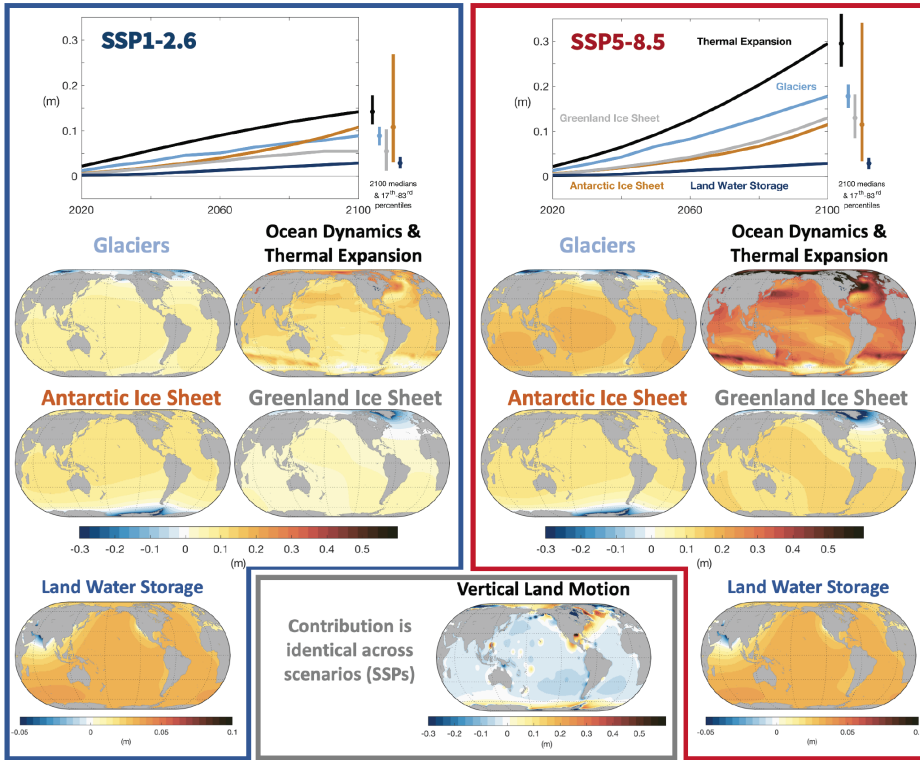
Figure 1.1: Median global mean and regional relative sea level projections (m) by contribution for the SSP1-2.6 and SSP5-8.5 scenarios. Upper time series: Global mean contributions to sea level change as a function of time, relative to 1995–2014. Lower maps: Regional projections of the sea level contributions in 2100 relative to 1995–2014 for SSP5-8.5 and SSP1-2.6. Vertical land motion is common to both Shared Socio-economic Pathways (SSPs). Figure and caption from IPCC (2023).

1.2   The Antarctic Ice Sheet and Ice Shelves

When snow accumulates in Antarctica's interior, it gradually compresses into ice, adding mass to the ice sheet (Cuffey and Paterson, 2006). Gravity drives this ice towards the ice sheet's margins, where it begins to extend over the ocean, forming ice shelves along approximately 75% of the coastline (Rignot et al., 2013). This configuration gives Antarctica the designation of a "marine ice sheet", as opposed to the Greenland Ice Sheet where most of the glaciers are land-terminating. The transition from grounded ice to floating ice is known as the grounding line or grounding zone. Ice shelves play a critical role in stabilizing the ice sheet by exerting a buttressing effect, which restricts the flow of grounded ice into the ocean (Schoof, 2007; Fürst et al., 2016). When buttressing

Global mean sea level rise relative to 1900
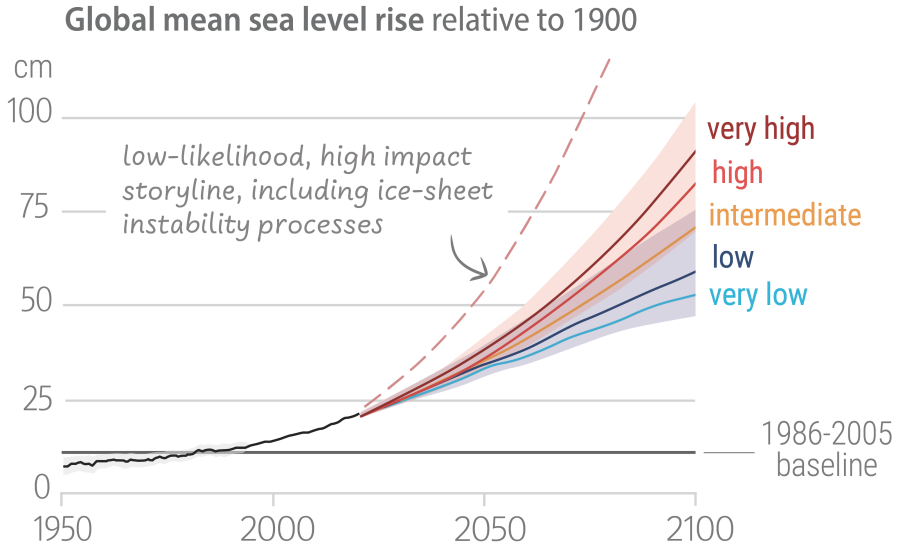
Figure 1.2: Projected global mean sea level rise under different Shared Socio-economic Pathway (SSP) scenarios (very low: SSP1-1.9; low: SSP1-2.6; intermediate: SSP2-4.5; high: SSP3-7.0; very high: SSP5-8.5). Likely global mean sea level change for SSP scenarios resulting from processes in whose projection there is medium confidence. Lightly shaded areas show the likely ranges. Black line show historical global mean sea level change. Dashed red line shows the low-likelihood, high impact storyline, which includes ice sheet instability processes. Figure and caption are adapted from IPCC (2023).

weakens, often due to thinning or structural loss in the ice shelves, ice flux across the grounding line can increase, accelerating sea level rise (Fürst et al., 2016). The uncertainty surrounding Antarctica's contribution to sea level rise stems largely from its status as a marine ice sheet, due to the key-role of the ice shelves and their uncertain response to a changing climate (Schoof, 2007; Fürst et al., 2016).

Assessing Antarctica's future contributions to sea level rise under different climate scenarios and socio-economic pathways requires a detailed understanding of the current buttressing effect of the ice shelves and, perhaps more crucially, the processes that impact this effect (Pattyn and Morlighem, 2020; van de Wal et al., 2022).

1.2.1 Ice shelf (in)stability processes

Several processes influence the stability, and therefore the buttressing effect, of an ice shelf, with more factors emerging on almost every occasion we observe ice shelves undergoing severe structural changes or collapse.

Surface melting is one such process that can weaken buttressing through mechanisms
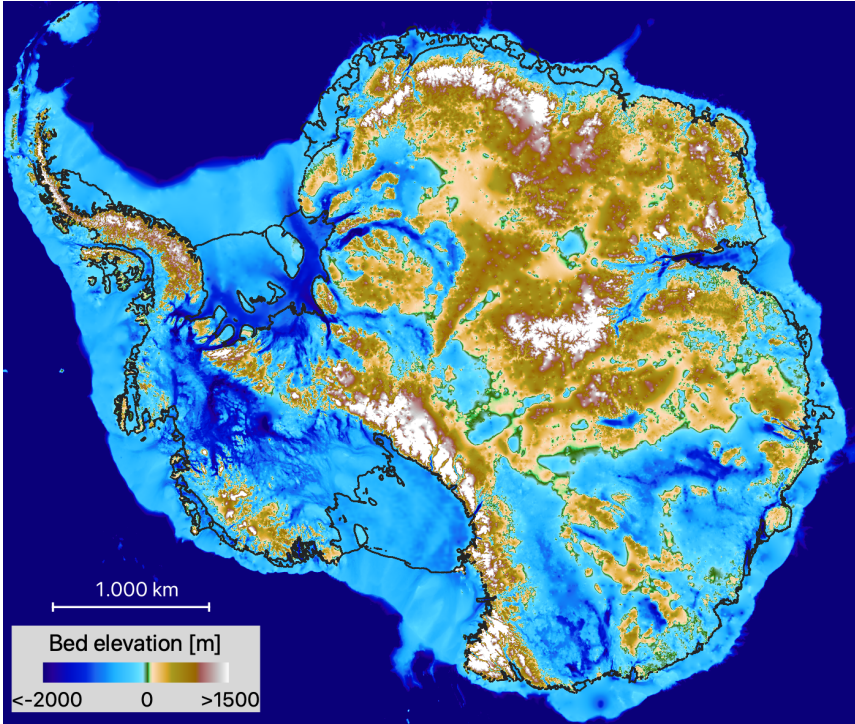
Figure 1.3: Bed elevation and ice shelf outlines (black line) from BedMachineV3 (Morlighem, 2022).

like hydrofracturing (Mobasher et al., 2016). Hydrofracturing occurs when surface melt-water collects in ponds or seeps into existing fractures, and drains through the ice, forcing cracks to rapidly widen and potentially causing partial or complete ice shelf collapse (Mobasher et al., 2016; Scambos et al., 2009; Banwell et al., 2013). A well-known example of this phenomenon is the complete collapse of the Larsen B Ice Shelf in 2002 (Banwell et al., 2013). Similarly, the Wilkins Ice Shelf experienced a partial collapse in 2008, also attributed to hydrofracturing (Scambos et al., 2009). Although most of Antarctica's climate remains cold enough to limit surface-melt-induced weakening on ice shelves that buttress the main ice sheet (van de Wal et al., 2022), projections for the end of this century indicate that many ice shelves could reach critical thresholds due to increased temperatures (van Wessem et al., 2023).

The significance of fractures and cracks in ice shelf stability becomes evident through the process of hydrofracturing. Furthermore, extensive fracturing and structural damage softens the ice, reducing its buttressing effect, and allowing greater ice flow across the grounding line (Albrecht and Levermann, 2014; Sun et al., 2017). This increased flow intensifies stresses within the ice, leading to further fracturing and creating a positive feedback loop (Lhermitte et al., 2020). Additionally, fractures may originate or propagate due to other factors beyond hydrofracturing, such as tidal forces, sea surface

slopes, and basal melting (Trusel et al., 2022; Francis et al., 2021; Dow et al., 2018).

Basal melting also compromises an ice shelf's buttressing effect by causing ice shelf thinning and grounding line retreat. Melting is generally more pronounced at greater depths (Sect. 1.2.2), and since most grounding lines are located at the deepest points of an ice shelf, these areas are particularly vulnerable (Schoof, 2007; Silvano et al., 2016; Morlighem et al., 2017). This process is especially critical for the West Antarctic Ice Sheet, where much of the ice rests on a bed significantly below sea level (Fig. 1.3, Morlighem et al., 2017, 2020). Here, basal melting can trigger grounding line retreat, potentially leading to irreversible ice loss due to the retrograde bed slope, a process known as Marine Ice Sheet Instability (Pattyn et al., 2018). Evidence suggests that marine ice sheet instability may already be underway in regions such as the Pine Island Ice Shelf and Glacier, marking basal melting as a significant threat even under current climate conditions (Reed et al., 2024). Furthermore, modelling suggest that over the twenty-first century, a tripling of ocean warming compared to historical rates, is likely already committed (Naughten et al., 2023). Such ocean warming unavoidably implies increased basal melting.

1.2.2   Ice-ocean interactions

Ice shelf basal melting occurs across the Antarctic continent and can be classified into three main modes based on the oceanic conditions driving the melting (Fig. 1.4, Jacobs et al., 1992; Silvano et al., 2016; Jenkins et al., 2016). While these modes are idealized, they provide a useful framework for understanding the distinct types of basal melting around Antarctica.

Mode 1 – Dense shelf water induced melting (Fig. 1.4a): In areas with cold surface water, sea ice formation releases salt (brine rejection), creating a dense, highly saline water mass. If this water becomes dense enough, it can sink and flow into the ice shelf cavity, where it initiates melting due to the decreasing seawater freezing point with depth. Since this dense water mass is very cold, the resulting melt rates are typically low. Mode 1 melting is thus most common in regions with high sea ice production, cold surface waters, and deep grounding zones, where the dense water mass remains above the freezing temperature set by pressure at these depths.

Mode 2 – Warm (modified) circumpolar deep water induced melting (Fig. 1.4b): This mode of melting is often referred to as warm cavity melting as the melting is caused by the intrusion of a warm water mass. That warm water mass is the circumpolar deep water (CDW), circling the entire Antarctic continent at depths around 500 m. This depth matches the depth of the continental shelf in certain areas, allowing CDW to spill over the shelf and reach ice shelf cavities, in these specific regions. With temperatures reaching $1°C$ to $1.5°C$, CDW can drive much higher basal melt rates than Modes 1 and 3. This mode thus predominates in regions where CDW crosses onto the continental shelf, with favorable shelf bathymetry enabling it to continue flowing into the ice shelf cavities.

Mode 3 – Surface water induced melting (Fig. 1.4c): During summer, surface waters
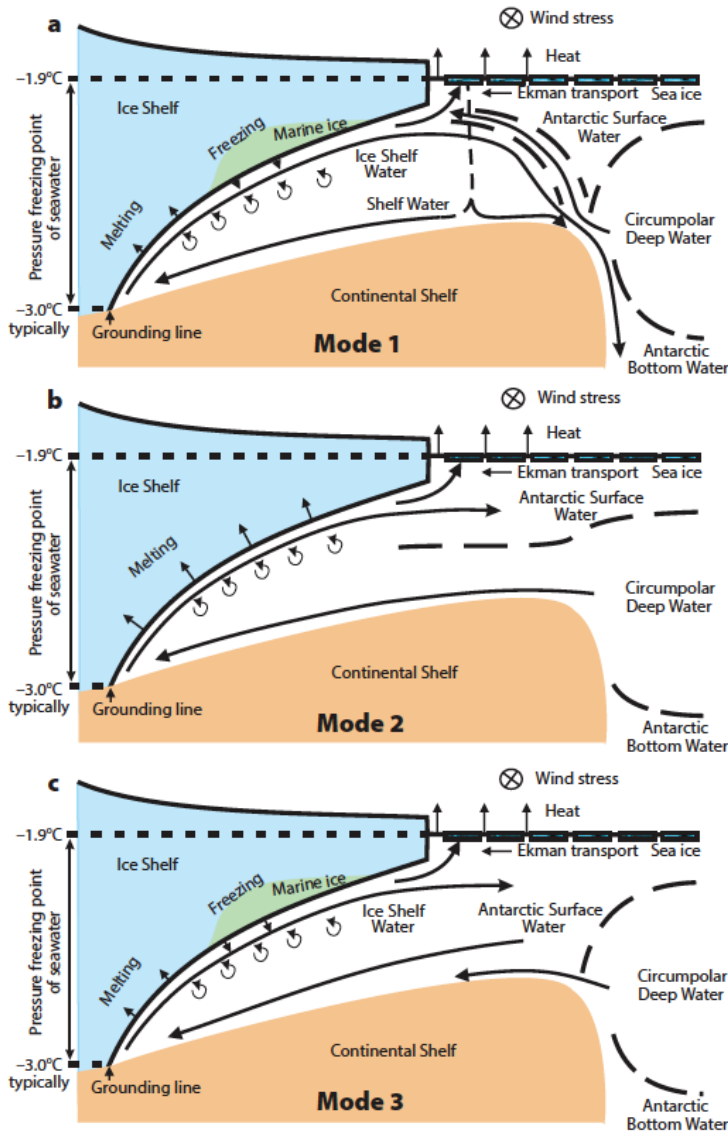
Figure 1.4: Three modes of sub-ice-shelf circulation and associated stratification on the continental shelf. The thick arrows indicate the sub-shelf circulation and the dashed lines separates the different water bodies. (a) In Mode 1, dense shelf water, formed by brine rejection beneath growing sea ice, dominates the sub-ice cavity. (b) Mode 2 dominates if shelf water is absent and circumpolar deep water spills onto the shelf driving fast melting. (c) Mode 3 dominates where both shelf water and circumpolar deep water are absent, leaving Antarctic surface water as the densest water on the shelf. Figure and caption from Jacobs et al. (1992) and Jenkins et al. (2016).
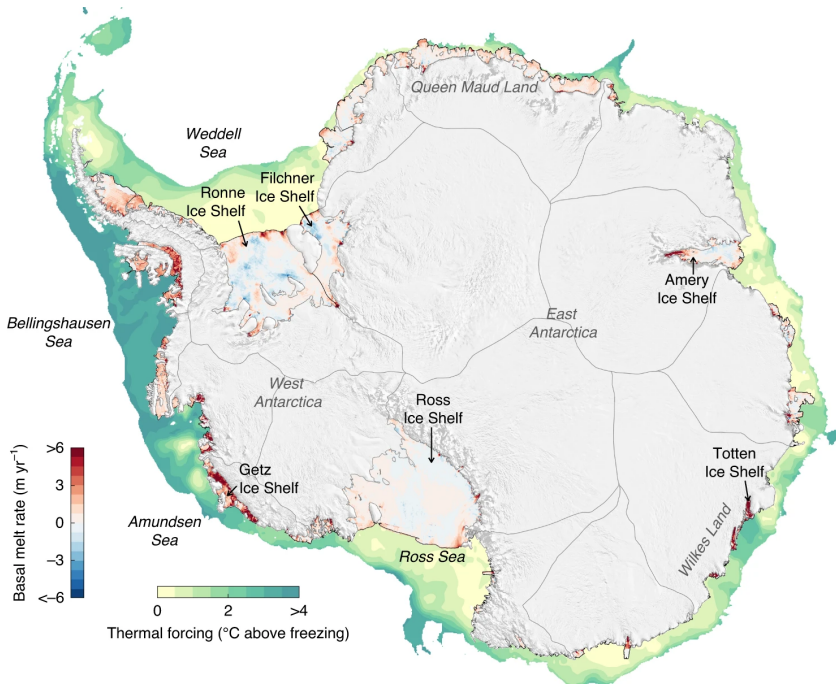
Figure 1.5: Basal melt rates averaged over 2010–2018 and thermal forcing, defined as the temperature above the in situ freezing point of seawater. The thermal forcing is mapped for water depths <1500 m. For water depths less than 200 m, the seafloor thermal forcing is shown, and for water depths >200 m, the maximum thermal forcing between 200 m and 800 m is shown. Figure and caption from Adusumilli et al. (2020).

can warm and be transported into ice shelf cavities by ocean circulation, tides, and eddies. In this mode, the relatively warm surface water becomes the primary water mass in the cavity, driving basal melting. For Mode 3 melting to be effective, the cavities must be relatively shallow, allowing the surface water to retain sufficient warmth to melt ice at depth.

As indicated in Fig. 1.5, Mode 2 melting, driven by CDW, results in the highest melt rates in Antarctica (Adusumilli et al., 2020; Silvano et al., 2016). This figure illustrates basal melt rates for most Antarctic ice shelves alongside thermal forcing, which indicates the presence of CDW. From the figure, it is evident that CDW-driven melting and high melt rates vary significantly across the continent, with particularly high melt rates in the Bellingshausen Sea, Amundsen Sea, and Wilkes Land regions. Many ice shelves in these areas buttress portions of the ice sheet that rest on beds far below sea level (Fig. 1.3), making these regions particularly vulnerable to marine ice sheet instability (Fürst et al., 2016; Silvano et al., 2016).

1.2.3 Ice shelf basal channels

Regardless of the melting mode, basal melting is typically most intense near the grounding zone due to the pressure-driven depression of seawater's freezing point (Silvano et al., 2016). From the grounding zone, the meltwater plume follows the ice shelf draft, moving towards the ice shelf front along a path shaped by the geometry of the ice shelf base and the Coriolis force. As the plume melts ice along its path, it becomes fresher and cooler, reducing its density and causing it to rise along the ice base slope. Although appearing smooth in the idealized Fig. 1.4, the ice draft is irregular in reality, and a slight trough in the ice draft presents a more favorable pathway for the plume than adjacent, deeper areas, allowing basal channels to form (Jacobs et al., 1992; Alley et al., 2022). These channels, therefore, experience the highest melt rates outside the immediate grounding zone region.

While high melt rates at the grounding zone can drive grounding line retreat, basal channels may act as structural weak points on the ice shelf. Rapidly melting basal channels can, in theory, penetrate the ice shelf, weakening its structure (Wearing et al., 2021). Research shows that basal channels can also promote fracturing within the channels themselves, as well as transverse fractures extending away from them (Vaughan et al., 2012; Dutrieux et al., 2014; Dow et al., 2018). Such fracturing can lead to calving events and ice shelf retreat, reducing the buttressing effect of the ice shelf. For instance, recent break-up and retreat events of Pine Island Ice Shelf were observed to occur along a basal channel, from which fractures were also originating (Sun and Gudmundsson, 2023; Alley et al., 2022). On the other hand, extensive networks of basal channels may help stabilize ice shelves by localizing melt to specific areas, thereby potentially reducing the overall ice shelf-wide melt rate (Alley et al., 2022). Basal channels thus pose a paradox for ice shelf stability, as they can both stabilize and destabilize the ice shelf structure.

Furthermore, basal channels can change in both size and position over time, possibly influenced by the availability of circumpolar deep water (Chartrand, 2017; Drews et al., 2020). Climate change, through its impact on ocean temperatures, affects both the volume and temperature of the circumpolar deep water (Naughten et al., 2023), as does larger climatic phenomena such as the El Niño Southern Oscillation (Dutrieux et al., 2014; Huguenin et al., 2024). More and warmer circumpolar deep water can intensify and accelerate meltwater plumes, driving changes in the size and migration of basal channels. Variations in meltwater availability may also promote fracture formation within channels (Alley et al., 2022), and basal channels have been observed to re-route along pre-existing fractures in the ice shelf (Alley et al., 2016). These processes – meltwater availability, channel melting intensity, re-routing, and fracturing – are closely interlinked but remain poorly understood, leaving many unanswered questions about basal channels (Alley et al., 2022). Understanding these features and their effects on ice shelf stability is essential for accurately assessing the current and future stability of the Antarctic Ice Sheet.

1.3   Observing and modelling ice shelf basal melting

1.3.1   Remote sensing "observations" of basal melting

Why use "observations" in quotation marks? Because basal melting cannot be directly observed using remote sensing or field-based in situ measurements – we can observe changes due to basal melting but not the process itself. One such change is the thickness of an ice shelf, which can be estimated from surface elevation measurements. Remote sensing techniques allow us to observe changes in ice shelf surface elevation, which can be translated into estimates of basal melt rates through a mass conservation using a Eulerian (fixed coordinate system) or Lagrangian (moving coordinate system that follows ice flow) framework.

In the Eulerian framework, the mass conservation equation is expressed as

$$\frac{\partial H}{\partial t} = -\nabla \cdot (H\boldsymbol{u}) + \dot{M}_s - \dot{M}_b, \tag{1.1}$$

where $\frac{\partial H}{\partial t}$ represents the Eulerian ice thickness change, H is the ice thickness, $\dot{M}_s$ is the surface mass balance, $\dot{M}_b$ is the basal melt rate (positive for melt), and $\nabla \cdot (H\boldsymbol{u})$ is the flux divergence term, with $\boldsymbol{u}$ as the average ice velocity down the ice column, assumed to be equivalent to the surface velocity for ice shelves. This equation indicates that any change in ice shelf thickness must be accounted for by changes in ice volume flux (e.g., stretching or compression), surface mass balance (e.g., surface melting or snowfall), and basal mass balance (e.g., basal melting or refreezing).

The mass conservation in a Lagrangian framework can be derived from the Eulerian framework by expanding the flux divergence term

$$\nabla \cdot (H\boldsymbol{u}) = H(\nabla \cdot \boldsymbol{u}) + \boldsymbol{u} \cdot (\nabla H) \tag{1.2}$$

and by using the relationship between Eulerian and Lagrangian thickness change

$$\frac{\mathrm{D}H}{\mathrm{D}t} = \frac{\partial H}{\partial t} + \boldsymbol{u} \cdot (\nabla H), \tag{1.3}$$

where $\frac{\mathrm{D}H}{\mathrm{D}t}$ is the Lagrangian thickness change. Combining these expressions leads to the mass conservation equation in the Lagrangian framework;

$$\frac{\mathrm{D}H}{\mathrm{D}t} = -H(\nabla \cdot \boldsymbol{u}) + \dot{M}_s - \dot{M}_b. \tag{1.4}$$

While satellite remote sensing cannot measure ice shelf thickness directly, it can provide data on surface elevation (h). Ice shelf thickness can be inferred by assuming that the ice shelf is in hydrostatic equilibrium

$$H = (h - h_f)\frac{\rho_w}{\rho_w - \rho_i}, \tag{1.5}$$

where ρ_i is the density of ice, ρ_w the density of sea water, and h_f is the firn air content. Firn refers to the (compacted) snow before it compresses fully into ice, and the firn air

content thus refers to the air space left within a column of firn, before it is compacted fully into ice. Substituting Eq. (1.5) into Eq. (1.4) and isolating the basal mass balance yields

$$\dot{M}_b = \dot{M}_s - \left(\frac{\mathrm{D}h}{\mathrm{D}t} - \frac{\mathrm{D}h_f}{\mathrm{D}t} + (h - h_f)(\nabla \cdot \boldsymbol{u})\right)\frac{\rho_w}{\rho_w - \rho_i}. \tag{1.6}$$

These equations form the foundation for deriving basal melt rates from remote sensing data. Most remote sensing basal melt products use similar data and numerical methods for many terms in Eq. (1.6). Both surface mass balance and firn air content are usually obtained from models, as field measurements are sparse. These models are usually coarse in their spatial resolution (>10 km), and remote sensing basal melt products rely on the same few models. Likewise, surface velocities are often based on the same remote sensing observations and the divergence of the velocity field ($\nabla \cdot \boldsymbol{u}$ in Eq. (1.6)) is then numerically approximated based on observations of surface velocities. This numerical solution may vary slightly in-between remote sensing basal melt products.

The primary distinction between various remote sensing basal melt products lies in the surface elevation data used. Surface elevation products used to derive basal melt rates can be categorized into three main types: altimetry, synthetic-aperture radar in tandem, and stereo imagery. Common for all satellite-based products is that high temporal resolution implies low spatial resolution, and vice versa. Each remote sensing technique offers different strengths and trade-offs, influencing the accuracy and applicability of the resulting basal melt rate estimates.

Altimetry

Altimetry provides surface elevations by measuring the two-way travel time between sending a signal (e.g., radar or laser pulse) from the altimeter towards the surface, and receiving the reflection back from the surface.

The launch of ICESat in 2003 marked a significant advancement in measuring Antarctic ice shelf surface elevations. Equipped with a laser altimeter, ICESat provided accurate year-round surface elevation data with a nadir footprint size of ∼65 m. One major benefit of laser altimetry is its ability to measure the true surface of the ice shelf, unlike radar altimetry which penetrates the snowpack. However, a notable limitation is its inability to penetrate clouds, restricting measurements to cloud-free days.

Using ICESat data from 2003 to 2008, Pritchard et al. (2012) were among the first to reveal that basal melting is the primary driver behind ice shelf thinning in Antarctica. They compared ice shelf elevation changes to surface and firn processes and glacier in-flow, indirectly applying mass conservation principles to reach this conclusion. Shortly after, Rignot et al. (2013) expanded on these findings by using similar surface elevation trends to estimate basal melt rates across most Antarctic ice shelves via an Eulerian approach. However, these estimates were limited by relatively coarse spatial and temporal resolution due to ICESat's coverage constraints (Fig. 1.6). These studies not only underscored the significant role of basal melting but also highlighted the varying melt rates across different regions.
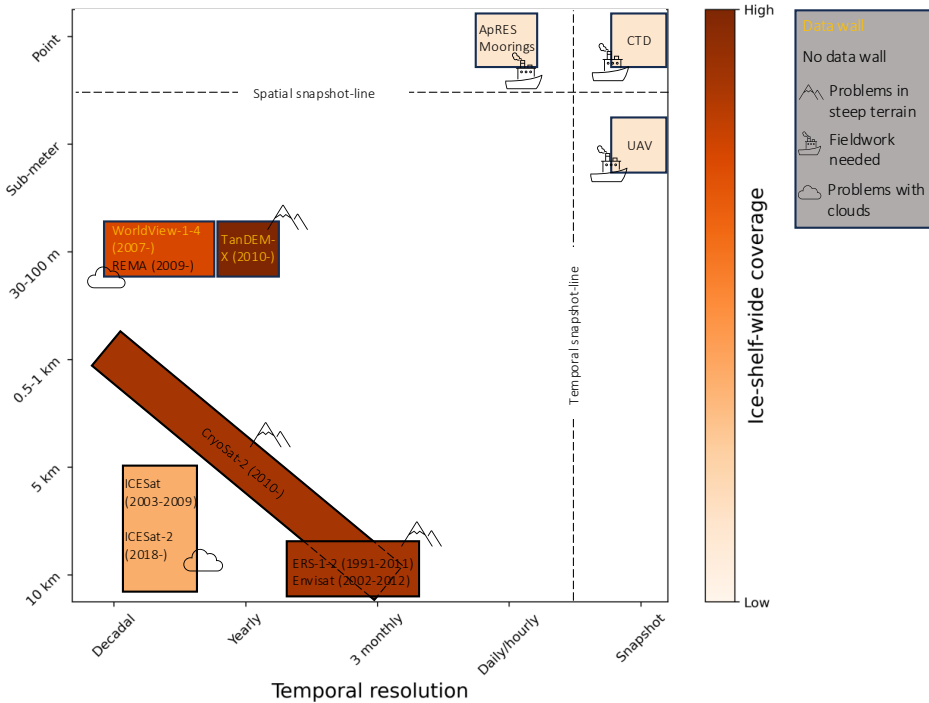
Figure 1.6: An overview of different observational sensors/methods used in deriving ice shelf basal melt rates. They are plotted with respect to the temporal and spatial resolution/grid size of the basal melt rates which can be derived from them, including coloring which indicates the ice shelf wide coverage. All satellite sensors are associated with their active years in brackets. Satellite products with restricted access are written in yellow ("Data wall").

In August 2010, just months before ICESat failed, CryoSat-2 was launched. This satellite carries a radar altimeter, which, unlike laser altimeters, can penetrate clouds, allowing for more comprehensive elevation measurements. However, radar altimeters do not always measure the true ice shelf surface; instead, the signal can reflect at different depths within the snowpack, influenced by factors such as snow density. CryoSat-2 provides elevation measurements at an approximate 400 m resolution along its track but only captures the surface closest to the satellite, meaning areas surrounded by steep slopes often remain unmeasured.

Traditionally, surface elevation from CryoSat-2 is derived using the point-of-closest-approach (POCA) method, which calculates the elevation of the point closest to the satellite for each pulse (Wingham et al., 2006). This method has been used to estimate surface elevation trends and basal melt rates for most Antarctic ice shelves from 2010 to 2020 on a 500 m grid, as shown by Adusumilli et al. (2020) (Fig. 1.5 and 1.6). They also used the POCA method to obtain high temporal resolution melt rates (e.g., 3-month

intervals), at the cost however, of reduced spatial resolution (around 10 km, Fig. 1.6). While this study allowed for relatively high spatial resolution basal melt rates, POCA-derived melt rates, however, always suffer from signal smoothing due to limited point measurements.

An alternative approach, known as swath processing, utilizes the entire measured swath to create a grid of elevation data instead of single points (Gourmelen et al., 2017, 2018). This method was first applied to derive basal melt rate trends for the Dotson Ice Shelf at a 500 m resolution from 2010–2016 (Gourmelen et al., 2017). Later, swath processing has been extended to generate melt rate trends for all Antarctic ice shelves at a 1 km resolution (Davison et al., 2023). While swath-based products have a similar or coarser grid spacing compared to POCA, they capture more detail due to comprehensive processing of the radar signal. Nevertheless, swath processing still struggles to fully capture areas with complex terrain, such as grounding zones flanked by mountains and regions near basal channels, leaving some areas unseen.

Synthetic-aperture radar

The twin satellites TerraSAR-X and TanDEM-X use radar interferometry to produce high-resolution digital elevation models (DEMs). Operating in tandem, they capture radar images of the Earth's surface from slightly different angles, allowing the phase differences between the images to be used for determining surface topography. Creating accurate DEMs involves comparing adjacent images or integrating data from other elevation sources, such as altimetry. This process of referencing the DEMs to each-other or through the use of accurate surface elevation is referred to as co-registration. By doing so, TanDEM-X can achieve a spatial resolution as fine as 12 m.

However, since TanDEM-X uses radar, it can penetrate into the snowpack, meaning the topography measured may reflect the actual surface or a few meters below it, depending on snow density and conditions. This characteristic is shared with CryoSat-2, which may lead to less accurate estimates of elevation changes.

TanDEM-X data has been employed to produce high-resolution basal melt rate maps, such as those for the Roi Baudouin Ice Shelf in East Antarctica at a 32 m grid spacing (Fig. 1.6, Berger et al., 2017). This represents one of the first detailed views of ice shelf basal melting at a fine scale, revealing variations in melt distribution within basal channels. The technique's high resolution makes it possible to identify uneven melting within these channels, offering insights that altimetry alone cannot not capture.

However, public access to TanDEM-X data is limited. Only a long-term DEM is available to the general public, while access to individual image pairs necessary for detailed surface elevation change analysis, and thus basal melt rate calculation, requires special requests and is restricted to citizens of select countries. Furthermore, TanDEM-X operates on request, which implies that the ice shelves are not necessarily covered regularly. This restricted access and acquisition pose a significant challenge for creating high-resolution remote sensing basal melt products for a wide range of ice shelves.

Stereo imagery

DEMs can also be created using optical satellite imagery through a process known as stereo imagery, which combines two images of the Earth's surface taken from slightly different angles. As for TanDEM-X, ground control points or altimetry data are required for co-registration of the DEMs. Stereo imagery needs both sunlight and clear, cloud-free conditions to be effective.

Stereo imagery from the WorldView satellites has been utilized to produce high-resolution, decade-averaged DEMs and basal melt rate trend estimates for Pine Island Ice Shelf, with a grid spacing of 32-256 m (Fig. 1.6, Shean et al., 2019). Similar to the findings from TanDEM-X for the Roi Baudouin Ice Shelf, the Pine Island study showed that basal channels play a dominant role in the melting pattern of the ice shelf.

However, access to WorldView stereo imagery is restricted and not publicly available to all nationalities. To address this, pre-processed DSMs became publicly accessible in 2018 under the Reference Elevation Model of Antarctica (REMA, Howat et al., 2019, 2022). REMA provides DEM strips at 2- or 8-meter resolution, as well as an average DEM covering most of Antarctica (excluding the polar gap). The first version of these REMA strips (the only version available when this research began) is also hosted on the cloud computing service Google Earth Engine. This platform offers significant advantages and opportunities for generating high spatial resolution basal melt rates across numerous ice shelves without requiring local data storage or local extensive computational resources.

1.3.2   Field "observations" of basal melting

As for remote sensing, direct measurements of ice shelf basal melting in the field are not possible. Instead, field studies rely on proxies to infer basal melting. These proxies are generally obtained through two primary methods: (1) sub-shelf measurements of ocean properties related to ice shelf meltwater and (2) on-shelf phase-sensitive radar measurements that track internal vertical ice displacements.

For sub-shelf measurements, properties such as temperature, conductivity, dissolved oxygen, and depth are monitored to infer the presence and impact of freshwater from ice shelf melting. These data are typically collected from ships, moorings, or under-water vehicles. Ship-based measurements use CTD (conductivity, temperature, depth) sensors along the ice shelf front and at various depths, providing snapshots that reveal inflow and outflow of water from which the ice-shelf-wide total basal melt rate can be estimated (e.g., Jenkins et al., 2018). Moorings installed through boreholes on the ice shelf continuously record data at depths below the ice base and can operate for years if maintained, offering detailed temporal data down to an hourly scale. However, because moorings rarely sample directly at the ice base, their melt rate estimates can be biased (e.g., Vaňková and Nicholls, 2022).

Underwater vehicles, capable of navigating beneath ice shelves, provide spatially de-tailed snapshots of ocean properties at various depths. Until recently, these vehicles

were deployed from ships and constrained to areas within a few kilometers of the ice shelf fronts due to communication limits, preventing them from reaching most high melting areas such as grounding zones and basal channels (e.g., Wåhlin et al., 2024). This changed with the development of ICEFIN, a cylindrical underwater vehicle deployable through boreholes. ICEFIN has already been used on Thwaites Ice Shelf to collect high-resolution melt rate data along transects near the grounding zone as well as within basal crevasses (Schmidt et al., 2023).

On-shelf measurements use (autonomous) phase-sensitive radars to monitor vertical displacements within the ice column with extreme accuracy. These radars track vertical movement throughout the ice column, allowing basal melt rates to be inferred by separating surface processes, internal ice dynamics, and basal changes, while accounting for overall ice thickness changes. Like moorings, phase-sensitive radars provide high temporal resolution at a single point and can remain operational year-round to gather continuous data (e.g., Vaňková and Nicholls, 2022).

Field measurements are valuable for their temporal or spatial details. However, direct comparisons between remote sensing and field data are challenging, due to the limited field measurement coverage (Fig. 1.6). Single-point measurements from moorings or radars differ from remote sensing-derived melt rates due to factors like ice movement (Lagrangian displacement), different observational periods, and the scale mismatch between a point and a grid cell of approximately 0.25 km^2 (for a 500 m grid size). Similarly, high-resolution transects offer only a temporal snapshot and cover just a few kilometers, aligning with few grid cells for comparison. Finally, the sporadic nature of field data, particularly measurements within basal channels, limits their utility in resolving the broader impact of channelized basal melting on ice shelf stability.

1.3.3   Modelling basal melting

Projections of sea level rise are typically made using Earth system models that integrate components such as ice, atmospheric, and ocean dynamics. Ocean models that can accurately account for the consequences of basal melting are thus essential for reducing uncertainties in predictions related to ice-shelf weakening and its contribution to sea level rise.

In general, the complexity of a model is directly proportional to its computational demand. Computationally efficient ocean models that include basal melting often lack the resolution needed to capture detailed features like channelized melting. On the other hand, high-resolution models capable of simulating these intricate structures are computationally intensive and often impractical for use in comprehensive coupled model systems. Although addressing this issue falls outside the scope of this thesis, it is important to acknowledge that all models, regardless of their complexity, rely on remote sensing and field measurements of basal melting for validation (e.g., Lambert et al., 2023; Lambert and Burgard, 2024). Therefore, it is crucial that remote sensing products accurately capture the melting patterns and structures that influence ice shelf stability. This enables ocean modelers to validate and calibrate their models with a focus on

areas most susceptible to weakening.

1.4   Research objectives and thesis outline

In summary, basal melting is crucial to the stability of Antarctic Ice Sheet. When ice shelf buttressing is reduced for instance due to basal melting, the flow of inland ice accelerates, contributing to sea level rise. A key aspect is channelized melting, where concentrated pathways of meltwater form beneath the ice shelf, creating channels of thinning that can undermine structural integrity and potentially lead to ice shelf weakening.

Despite advancements in remote sensing, field observations, and modelling, substantial research gaps persist. Some of these gaps are methodological. For instance, how well are different remote sensing products capable of capturing channelized melting? What impact does the usage of different products have on ice shelf weakening assumptions? Other gaps are related to the processes. For example, what is the general impact of channelized melting on ice shelf weakening? How do these channels evolve over time and why? Current remote sensing products face challenges related to spatial resolution, coverage, and data accessibility, making it difficult to map the fine-scale structures of channelized melting over large areas. To deepen our understanding of small-scale basal melting and its influence on ice shelf stability, efforts must focus on producing high-resolution basal melt rate maps across various ice shelves.

In this thesis the aim is **"To develop improved remote sensing methods for capturing small-scale basal melting features**, **such as basal channels**, **enhance our understanding of their impact on ice shelf weakening**, **and to explore their link to external drivers."** The hypothesis is that by combining REMA stereo imagery with altimetry data and leveraging cloud computing platforms like Google Earth Engine, it is possible to develop a scalable method for generating high-resolution basal melt maps. Furthermore, it is hypothesized that these maps enable detailed studies of basal channels and the factors driving their evolution and in that way provide critical insights into ice shelves' vulnerability to channelized melting. This objective will be achieved by addressing the following research questions:

> **RQ1**   What is the added value of using a combination of REMA stereo imagery and satellite altimetry in resolving ice shelf basal melt patterns?

> **RQ2**   What is the impact of high resolution basal melt maps in assessing basal channel melt rates and ice shelf channel vulnerability?

> **RQ3**   To which extent can changes in basal channel patterns be linked to changes in external drivers?

The three research questions are related to the thesis content as follows:

Chapter 2: *Unveiling spatial variability within the Dotson Melt Channel through high-resolution basal melt rates from the Reference Elevation Model of Antarctica* relates to RQ1. The aim is to develop a method which combines CryoSat-2 altimetry and REMA elevations to generate high-resolution basal melt maps of the Dotson Ice Shelf using the Google Earth Engine cloud computing service. Furthermore, the goal is to create a versatile method for estimating basal melt rates with improved resolution compared to altimetry-only products. A method that can be applied to any ice shelf and enables the detection of small-scale features, such as basal channels.

Chapter 3: *Exposure to Underestimated Channelized Melt in Antarctic Ice Shelves* relates to RQ2 and also expands on RQ1. The aim is to explore how well different remote sensing basal melt products resolve channelized melting and to what extend this impacts assumptions about ice shelf weakening. This is based on the hypothesis that radar-altimetry-only-derived basal melt maps generally fail to capture the full depths of basal channels due to their coarse resolution, unlike products combining altimetry with stereo imagery, and that these limitations affect assumptions about ice shelf weakening.

Chapter 4: *Ocean-Induced Weakening of George VI Ice Shelf* relates to RQ3 and explores a feature in a highly channelized area on the ice shelf, expressed by high basal melt rates. In this chapter, the causes of the high basal melt rates as well as how different external drivers may have caused its emergence are investigated. This is based on the hypothesis that inconsistencies in melt pathway of basal melt trend maps reflect shifts in meltwater pathways, which must be driven by changes in external factors.

Chapter 5: *Conclusions and Outlook* summarizes the findings of this thesis and elaborates on future possibilities and research directions based on this thesis.

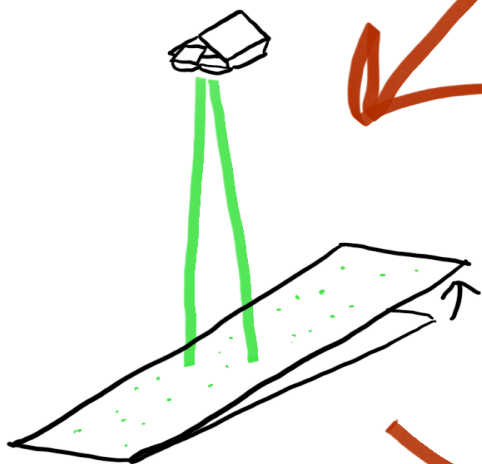*1.4 | Research objectives and thesis outline*

Chapter 2

Unveiling Spatial Variability within the Dotson Melt Channel through High-Resolution Basal Melt Rates from the Reference Elevation Model of Antarctica

The intrusion of Circumpolar Deep Water in the Amundsen and Bellingshausen Sea embayments of Antarctica causes ice shelves in the region to melt from below, potentially putting their stability at risk. Earlier studies have shown how digital elevation models can be used to obtain ice shelf basal melt rates at a high spatial resolution. However, there has been limited availability of high-resolution elevation data, a gap the Reference Elevation Model of Antarctica (REMA) has filled. In this study we use a novel combination of REMA and CryoSat-2 elevation data to obtain high-resolution basal melt rates of the Dotson Ice Shelf in a Lagrangian framework, at a 50 m spatial posting on a 3-yearly temporal resolution. We present a novel method: Basal melt rates Using REMA and Google Earth Engine (BURGEE). The high resolution of BURGEE is supported through a sensitivity study of the Lagrangian displacement. The high-resolution basal melt rates show a good agreement with an earlier basal melt product based on CryoSat-2. Both products show a wide melt channel extending from the grounding line to the ice front, but our high-resolution product indicates that the pathway and spatial variability of this channel is influenced by a pinning point on the ice shelf. This result emphasizes the importance of high-resolution basal melt rates to expand our understanding of channel formation and melt patterns. BURGEE can be expanded to a pan-Antarctic study of high-resolution basal melt rates. This will provide a better picture of the (in)stability of Antarctic ice shelves.

2

2.1 Introduction

Ice shelves in the Amundsen Sea Embayment of Antarctica are subject to intrusion of warm Circumpolar Deep Water, which is one of the processes that can cause basal melting (Noble et al., 2020). This can lead to ice shelf thinning, grounding line retreat, and a reduction in the ice shelf resistive forces on the tributary glaciers (Schoof, 2007). The thinning and force reduction put the tributary glaciers at risk, particularly in regions with a retrograde bed slope where marine ice sheet instability processes might be initiated (Schoof, 2007; Ritz et al., 2015). Furthermore, Morlighem et al. (2021) show that the location of temporal changes in basal melt of ice shelves in the Amundsen Sea sector of Antarctica matters for glacier-wide mass balances, making spatially detailed elevation changes and basal melt rates important. Therefore, it is important to monitor basal melting and ice shelf thinning to gain additional knowledge about the potential destabilization of ice shelves. Monitoring can be done in situ from ice-penetrating radar (Berger et al., 2017; Lindbäck et al., 2019), phase sensitive radars (Lindbäck et al., 2019; Vaňková and Nicholls, 2022), or direct ocean measurements of conductivity and temperature at depth (Vaňková and Nicholls, 2022) or remotely through satellite observations of changes in ice shelf surface elevation in combination with information about ice flow and surface processes (Berger et al., 2017; Adusumilli et al., 2020). The in situ measurements can provide melt and thinning rates at a high accuracy, but they are usually restricted to a few point measurements and a temporal resolution defined by fieldwork constraints, though it should be noted that autonomous phase-sensitive radars provide continuous point measurements with fewer ties to fieldwork constraints for an extended period of time. Remote sensing observations, on the other hand, can provide a high spatial and temporal resolution but come with a series of assumptions needed to turn surface elevation measurements into thinning and melt rates.

Previous studies have shown how various satellite techniques can be used to obtain ice shelf thinning and basal melt rates (Rignot et al., 2013; Adusumilli et al., 2020; Shean et al., 2019; Berger et al., 2017; Gourmelen et al., 2017). This can be done by using, e.g., stereo imagery (Shean et al., 2019), synthetic aperture radar (Berger et al., 2017), altimetry (Rignot et al., 2013; Moholdt et al., 2014; Gourmelen et al., 2017), or by a combination of the different techniques (Shean et al., 2019; Adusumilli et al., 2020). Common to all remote-sensing-based basal melt rate products is that they assume hydrostatic equilibrium to translate remotely sensed surface elevations into ice thickness, from which basal melt rate estimates can be obtained through a mass conservation approach. This is often done in a Lagrangian framework where the basal mass balance of an ice parcel is assessed, in contrast to the Eulerian framework where the basal mass balance of a given point in space is assessed. Applying a Lagrangian framework thus allows one to assess the thinning and basal melt rate of a given ice parcel over time and takes the ice flow into consideration. The study by Berger et al. (2017) was one of the first providing high-resolution Lagrangian basal melt rates of an Antarctic ice shelf. They used surface elevations based on satellite imagery from the twin synthetic aperture radar satellite mission TanDEM-X, from which digital elevation models (DEMs) were generated by co-registering the TanDEM-X elevations with a CryoSat-2 DEM (Helm et al.,

2014). This approach allowed the assessment of basal melt rates of the Roi Baudouin Ice Shelf at a 10 m spatial posting, which revealed several small-scale melt channels. Shean et al. (2019) used stereo imagery from the WorldView and GeoEye satellites to generate high-resolution digital surface models of the Pine Island Glacier ice shelf, which were converted to DEMs by co-registering with laser altimetry measurements from ICESat and NASA Operation IceBridge. The resulting DEMs from 2008 to 2015 were used to obtain 32-256 m multi-scale posting basal melt rates. Earlier, also Dutrieux et al. (2013) assessed the basal melt rate of the Pine Island Glacier ice shelf using a similar approach but using the slightly coarser resolution SPIRIT DEMs. Gourmelen et al. (2017) took on a different approach by only using altimetry measurements. They used CryoSat-2 swath measurements (Gray et al., 2013) to obtain 500 m posting melt rates of the Dotson Ice Shelf over the period from 2010-2016. They revealed a ~5 km wide channel extending from the area around the grounding zone all the way to the ice shelf front.

A general concern when assessing ice shelf basal melt rates using a mass conservation approach is the temporal and spatial resolution. This is not only determined by elevation data availability, but also by the availability and resolution of, e.g., ice velocity, firn, and surface mass balance data. Both the temporal and spatial resolution will put a constraint on the information level of the resulting basal melt rates since the basal melt pattern may vary on seasonal to inter-annual timescales (Watkins et al., 2021; Wearing et al., 2021; Dutrieux et al., 2013; Stanton et al., 2013). Unfortunately, high temporal and spatial resolution does not always go hand in hand. Altimetry can provide quasi-monthly basal melt rates (Adusumilli et al., 2020) but at the cost of the spatial resolution. In contrast, high-resolution stereo imagery is temporally currently mostly limited to inter-annual, or coarser, timescales. Focusing further on the drawbacks of the different elevation measurement techniques, there is one clear limitation to relying fully on satellite radar altimetry measurements, which is the fact that in many regions, mountainous terrain near the ice shelf margins prevents the satellite radar signal from reaching all parts of the ice shelf (Dehecq et al., 2013). On the other hand, high-resolution products come with challenges regarding data volume and availability/accessibility. For example, the TanDEM-X, WorldView, and GeoEye data are not directly publicly available, which puts a major limitation on the accessibility. Also, transforming the raw satellite imagery into digital surface models is tedious and may serve as a limit for the temporal coverage of a study. In this study, we exploit the Reference Elevation Model of Antarctica (REMA Howat et al., 2019) as an alternative. REMA provides 2 or 8 m resolution digital surface model strips generated from satellite imagery from the WorldView and GeoEye satellites from 2011-2017. In contrast to the raw satellite imagery, REMA is publicly available, thereby providing opportunities for researchers without direct access to the underlying data.

Chartrand and Howat (2020) have shown that REMA in combination with ICESat and IceBridge can be used to derive basal melt rates and study channel evolution on the Getz Ice Shelf. However, it is also evident that using REMA to derive high spatial and temporal resolution basal melt rates introduces a new set of problems, in particular the co-registration of the individual digital surface strips and the Lagrangian ice parcel

2. Unveiling Spatial Variability within the Dotson Melt Channel through High-Resolution Basal Melt Rates from the Reference Elevation Model of Antarctica

2
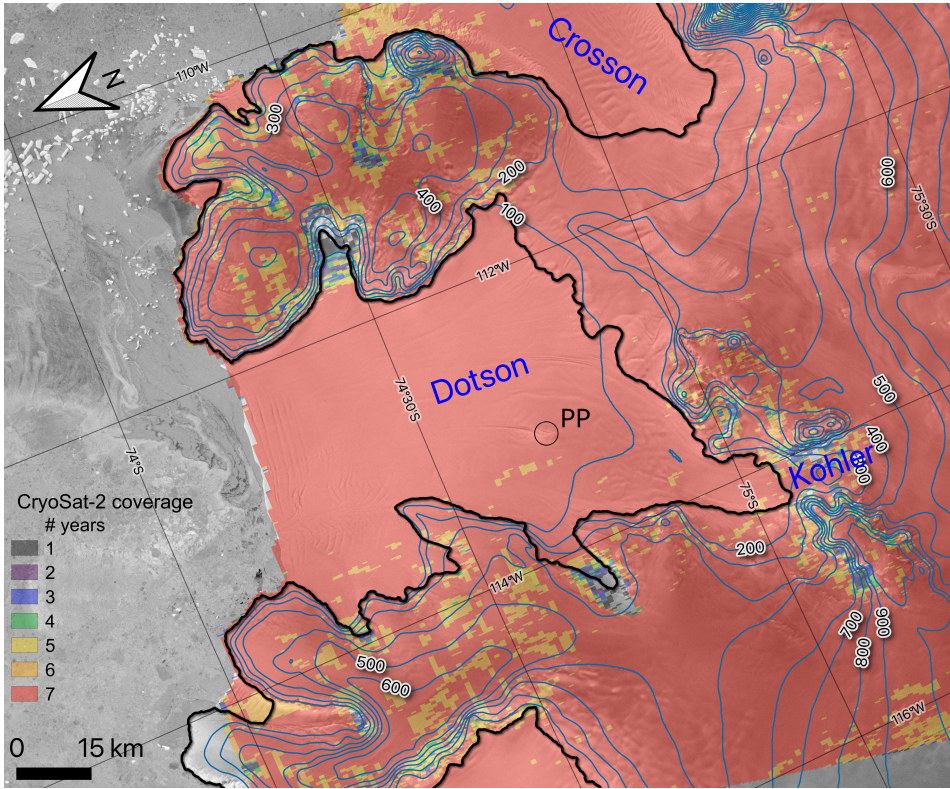
Figure 2.1: Overview of the test site with the Dotson and Crosson ice shelves marked along with the Kohler Glacier feeding the Dotson Ice Shelf. A pinning point on the ice shelf is marked with a circle and PP. The background image is the Radarsat Antarctic Mapping Project mosaic which has been overlaid with surface elevation contour lines (blue), the ASAID grounding line (black, Bentley et al., 2014), and the CryoSat-2 Swath coverage in the period from 2010-2016 with colors showing how many years are represented in each pixel (Matsuoka et al., 2021).

tracking. First, co-registering the REMA digital surface model strips and transforming them into DEM strips requires several processing steps. Absolute elevation data from, e.g., altimetry are needed to correct the relative REMA elevation data (Berger et al., 2017; Shean et al., 2019), but the REMA data are from a period at the very end of the ICESat mission (2003-2009) and before the ICESat-2 launch in 2018. In between, only Operation IceBridge and CryoSat-2 surface elevation data are available for co-registration. Operation IceBridge carries a laser altimeter among other instruments and was initialized to fill the gap between ICESat and ICESat-2 but at a drastically reduced spatial and temporal coverage. CryoSat-2, on the other hand, carries a radar altimeter which allows elevation measurements even under cloudy conditions, which makes it suitable as a reference for co-registration. Chartrand and Howat (2020) used

Operation IceBridge where available to co-register the REMA strips and CryoSat-2 otherwise. Second, the Lagrangian thinning and melt rates rely on co-registering the DEMs, either by feature tracking between two DEMs (e.g., Berger et al., 2017) or by displacing the DEMs using an existing velocity field (e.g., Moholdt et al., 2014). Both methods come with errors which will propagate into the resulting thinning and basal melt. The accuracy of the displacement thereby also influences the highest possible spatial resolution and signal-to-noise ratio of both the Lagrangian elevation change and basal melt rate.

In this study we use the REMA strips in combination with CryoSat-2 measurements to obtain thinning and basal melt rates of the Dotson Ice Shelf at a 50 m spatial posting and a 3-yearly temporal resolution in the period from austral summer 2010/11 to 2017/18. We present and assess the high-resolution Basal melt rates Using REMA and Google Earth Engine (BURGEE) method. BURGEE is run on the Google Earth Engine (GEE), thereby allowing easy access to the data and fast processing on the GEE cloud computing platform (Gorelick et al., 2017). Furthermore, the use of GEE, REMA, and CryoSat-2 allows for easy upscalability. We use Dotson (Fig. 2.1) as a test site since there already exists a detailed basal melt rate study for comparison (Gourmelen et al., 2017). As mentioned, Gourmelen et al. (2017) relied fully on radar altimetry, which has limited coverage in mountainous regions. From Fig. 2.1 it is clear that this is an issue on parts of Dotson, which also becomes evident in the spatial coverage of the basal melt rates obtained in Gourmelen et al. (2017). For example the Kohler grounding zone (see Fig. 2.1) is poorly constrained, although here high melt rates are to be expected due to the intrusion of warm Circumpolar Deep Water into the ice shelf cavity (Jacobs et al., 1992). To investigate the highest feasible posting, we will perform a sensitivity study assuming that the highest uncertainties are related to the quality of the Lagrangian displacement. We will, furthermore, compare our results to the basal melt rates of Gourmelen et al. (2017) and discuss the different features we observe and the possible influence of a pinning point on basal channel formation and melt rates.

2.2 Theory

The basal mass balance and elevation change of an ice shelf can be observed in both a Eulerian and a Lagrangian framework. The Eulerian framework is fixed in space and provides information about the basal mass balance or elevation change at a given point in space. The Lagrangian framework, on the other hand, follows a given ice parcel and assesses the basal mass balance or elevation change of that parcel between two places in time, thereby taking the ice flow into consideration. In both cases the basal mass balance can be calculated through a mass conservation approach, which in a Lagrangian framework can be expressed as

$$\frac{\mathrm{D}H}{\mathrm{D}t} = -H(\nabla \cdot \boldsymbol{u}) + \dot{M}_s - \dot{M}_b, \tag{2.1}$$

where $\frac{\mathrm{D}H}{\mathrm{D}t}$ is the Lagrangian ice thickness change; H is the ice thickness; $\nabla \cdot \boldsymbol{u}$ is the divergence of the ice flow; $\dot{M}_s$ is the surface mass balance; and $\dot{M}_b$ is the basal mass

balance, defined as positive for melt. By assuming hydrostatic equilibrium, a constant ice density of $\rho_i = 917$ kg· m^{-3}, and a constant sea water density of $\rho_w = 1025$ kg· m^{-3}, the ice thickness can be approximated by

$$H = (h - h_f)\frac{\rho_w}{\rho_w - \rho_i}, \tag{2.2}$$

where h is the ice shelf surface elevation and h_f the firn air content in meters ice equivalent. Substituting Eq. (2.2) into Eq. (2.1) leads to

$$\frac{\mathrm{D}h}{\mathrm{D}t} - \frac{\mathrm{D}h_f}{\mathrm{D}t} = (h - h_f)(\nabla \cdot \boldsymbol{u}) + (\dot{M}_s - \dot{M}_b)\left(\frac{\rho_w - \rho_i}{\rho_w}\right), \tag{2.3}$$

from which we can obtain the basal mass balance:

$$\dot{M}_b = \dot{M}_s - \left(\frac{\mathrm{D}h}{\mathrm{D}t} - \frac{\mathrm{D}h_f}{\mathrm{D}t} + (h - h_f)(\nabla \cdot \boldsymbol{u})\right)\frac{\rho_w}{\rho_w - \rho_i}. \tag{2.4}$$

2.3 Data

As can be seen from the basal mass balance Eq. (2.4), several auxiliary data sets are required to extract basal melt rates. In this section, we discuss the different data sets used in BURGEE to obtain and evaluate thinning and basal melt rates of the Dotson Ice Shelf.

2.3.1 Surface elevation

To obtain surface elevations of high temporal and spatial resolution we make use of the Reference Elevation Model of Antarctica (REMA, Howat et al., 2019). REMA consists of numerous digital surface model strips of either 2 or 8 m spatial resolution. They are based on stereo imagery from the WorldView and GeoEye satellites and acquired between 2010 and 2017. The strips are referenced to the WGS84 ellipsoid and are not co-registered. We have chosen to exclude all strips generated using the GeoEye satellites since they suffer from inconsistencies in the surface topography in the form of a striped pattern perpendicular to the satellite flight direction. Besides the strips, a REMA mosaic, made from multiple strips that have been co-registered with CryoSat-2 and ICESat (Howat et al., 2019), will be used as a reference surface to exclude outliers.

To correct the REMA strips for tilt and bias, elevation measurements from the radar altimeter aboard CryoSat-2 are used. CryoSat-2 was launched in 2010 and is the only ice-sheet-focused altimeter-carrying satellite which has been active throughout our entire study period ranging from austral summer 2010/11 to 2017/18. To transform the waveforms of the CryoSat-2 Level-1B SARin Baseline-D product to elevations with respect to the WGS84 ellipsoid, we use the leading-edge maximum gradient retracker presented in Nilsson et al. (2016). CryoSat-2 elevations are corrected for ocean loading tide, solid earth tide, geocentric polar tide, and dry and wet tropospheric and ionospheric effects using the data provided by ESA. Furthermore, the measurements are

filtered using the ESA-provided quality flags. Additional ice-shelf-specific corrections are outlined in Sect. 2.4.1. The downside of using CryoSat-2 is that the radar signals may penetrate into the snowpack, thereby not measuring the direct surface but some depth into the snowpack. To study this effect, we compared CryoSat-2 measurements to those of the laser altimeter aboard ICESat-2 in the period from 2018 to 2021. From a comparison between neighboring measurements within 50 m and 5 d, we found a mean penetration depth of -0.4 m with a standard deviation of 2.1 m. We therefore assume that CryoSat-2 elevations can be considered to represent surface elevations.

Both the REMA strips and CryoSat-2 elevations are filtered for outliers by masking out elevations that differ more than 30 m from the REMA mosaic. This might filter out the advection of some large crevasses. However, since the REMA mosaic of Dotson is composed of REMA strips from mainly 2015 and 2016, this should mostly affect strips from the early years, if at all. After this filtering, both the REMA and CryoSat-2 elevation data are referenced to the Earth Gravitational Model 2008 geoid (Pavlis et al., 2012).

2.3.2 Surface velocity

Surface velocities are needed to calculate the ice flow divergence in the basal mass balance Eq. (2.4) and to perform a first-order displacement of the DEMs in the chain process of performing the Lagrangian displacement. The surface velocity data are obtained from the MEaSUREs ITS_LIVE data product (Gardner et al., 2022). These 120 m resolution surface velocities are generated using feature tracking of optical Landsat imagery. Since the velocity field of Dotson has shown no significant change throughout our study period (Lilien et al., 2018), we use the 120 m ITS_LIVE composite. Furthermore, we assume that the ice velocity does not vary with depth.

2.3.3 Surface mass balance

Since part of the observed ice shelf thickness change, or lack thereof, may be related to surface processes, monthly surface mass balance values ($\dot{M}_s$ in Eq. (2.4)) are obtained from the regional climate model RACMO 2.3p3 (van Wessem et al., 2018). The output from RACMO is given in millimeters of water equivalent and translated into meters of ice equivalent by using an ice density of $917 \, \text{kg} \cdot \text{m}^{-3}$. We perform a spatial extrapolation since the 27 km grid does not cover the entire ice shelf. This is done by applying a linear extrapolation over a distance of 5 pixels. Finally, the data are interpolated onto the DEM grid from the original 27 km resolution grid using a bicubic interpolation.

2.3.4 Firn air content

To obtain the local ice equivalent thickness of the ice shelf, the presence of air in the firn layer needs to be taken into account (h_f in Eq. (2.2)). Estimates of firn air content are obtained from the 27 km resolution IMAU-FDM v1.2A (Veldhuijsen et al., 2023) on a 10 d basis. The IMAU-FDM is forced with climate data from RACMO, which is why they share the same resolution. This also means that we apply an identical spatial

extrapolation for the firn air content as for the surface mass balance (see Sect. 2.3.3) to ensure coverage over the entire ice shelf, followed by a bicubic interpolation onto the DEM grid.

2.3.5 Basal melt rate comparison products

To evaluate BURGEE we compare our results with two existing melt products, based on remote sensing and an ocean model, respectively. The remote-sensing-based product is obtained from CryoSat-2 swath measurements resulting in a mean basal melt rate product in the period from 2010-2016 at a 500 m resolution (Gourmelen et al., 2017, Fig. 2.6b). The ocean modeling product (LADDIE) is obtained by a 2D dynamical downscaling of the 3D ocean model MITgcm resulting in basal melt rates at a 500 m resolution (Lambert et al., 2022, Fig. 2.6c).

To investigate the basal melt pattern we further focus on the thermal forcing and the friction velocity provided by LADDIE, since basal melt can be approximated by the product of these two terms (e.g., Favier et al., 2019). The thermal forcing is the difference in temperature between the ocean water just below the ice shelf and the freezing point and can thereby be interpreted as the available heat to melt the ice. The friction velocity, defined as the time-mean ocean velocity just below the ice shelf, describes how effectively the heat is transported to the ice.

2.4 Methods

In the following sections we describe the methodology applied in BURGEE to calculate the basal melt rate using Eq. (2.4). Firstly, the REMA strips have to be transformed to digital elevation models by first accounting for dynamic and static corrections such as tides (see Sect. 2.4.1) and thereafter through a co-registration with CryoSat-2 (Sect. 2.4.2). A schematic overview of this procedure can be seen in Fig. 2.2. The resulting DEMs are then used to obtain both Eulerian (Sect. 2.4.3) and Lagrangian surface elevation changes (Sect. 2.4.5). The latter, along with ice flow divergences (Sect. 2.4.4), are used in the basal melt rate calculation (Sect. 2.4.5). Finally, a sensitivity study (Sect. 2.4.6) is performed to assess the highest feasible posting.

2.4.1 Dynamic and static corrections

Dynamic and static corrections have to be applied to both the REMA strips and the CryoSat-2 elevations to bring all elevations to the same reference frame regardless of variations in sea level.

Due to the underlying ocean beneath the ice shelf, tides (Δh_t), mean dynamic topography (Δh_{mdt}), and the inverse barometer effect (Δh_{ibe}) should also be taken into consideration in the ice shelf elevation corrections. Just like the geoid, the mean dynamic topography is a static correction, for which we use DTU15MDT, which is an updated version of DTU13MDT (Andersen et al., 2015). Tidal heights are obtained from the CATS2008 model on a 6 h interval at a ~3 km spatial resolution for the REMA strips.

Tidal heights for CryoSat-2, however, are obtained at their point locations and acquisition times. The inverse barometer effect was corrected for by using the 6 h NCEP/NCAR sea level pressure reanalysis data (Kalnay et al., 1996), from which residuals were calculated by using a mean sea level pressure of 1013 hPa. The residuals are then scaled by ~0.9948 cm hPa^{-1} to obtain the inverse barometer effect (Wunsch, 1972). The correction for the tide and inverse barometer effect are based on the acquisition time of the first stereo image. Since the ocean-induced corrections are only applicable to the ice shelf itself, the corrected surface elevation is obtained through

$$h = h_{data} - \Delta h_{geoid} - \alpha \left(\Delta h_t + \Delta h_{mdt} + \Delta h_{ibe} \right), \qquad (2.5)$$

where h_{data} is either the CryoSat-2 or REMA surface elevations, Δh_{geoid} is the offset to the geoid, and α is a coefficient ensuring a smooth transition from grounded to floating ice as in Shean et al. (2019). This transition is a function of the distance to the grounding line (l), based on the ASAID product of (Bentley et al., 2014):

$$\alpha(l) = \begin{cases} 0 & l \le 0km \\ \frac{1}{3}l & 0km < l \le 3km \\ 1 & l > 3km \end{cases} . \qquad (2.6)$$

Once the corrections have been applied the elevation data are at the stage marked with an asterisk (*) in Fig. 2.2.

2.4.2   Co-registration

Since the REMA strips have not been co-registered with the actual surface elevation, strips might be both tilted and vertically misplaced. A co-registration with actual surface elevations therefore is needed. Here, the co-registration of the REMA strips is performed by using two consecutive plane-fit co-registration approaches: first with respect to the CryoSat-2 measurements and second with respect to overlapping REMA strips. The double co-registration is performed to improve the quality, as there might still be small offsets between strips where they overlap. The co-registration with CryoSat-2 is done by correcting for tilt and vertical bias after fitting a plane through the residuals between CryoSat-2 and the individual REMA strips.

Before the co-registration of a REMA strip with CryoSat-2 can be performed, we defined four criteria that should be fulfilled in the given order: (i) the CryoSat-2 elevations used to perform the co-registration have to be within 1 month of the acquisition date of the REMA strip to ensure that the CryoSat-2 elevations are representative of the elevations when the strip was acquired; (ii) for each and every REMA strip the number of available CryoSat-2 measurements/matchups that have fulfilled criterion (i) should be at least 80 to ensure that we perform a representative plane fit. This threshold has been set through trial and error and is a balance between good-quality co-registration while keeping a sufficient number of REMA strips; (iii) the northernmost and southernmost CryoSat-2 points should be at least 60 km apart. Likewise, the CryoSat-2 points furthest separated

2. Unveiling Spatial Variability within the Dotson Melt Channel through High-Resolution Basal Melt Rates from the Reference Elevation Model of Antarctica

2
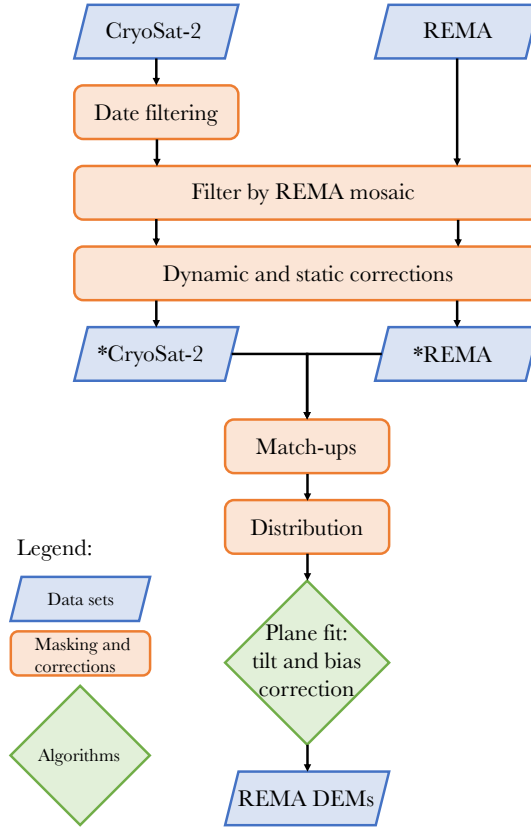
Figure 2.2: Flow chart showing the procedure going from WGS84-referenced CryoSat-2 and REMA digital surface model elevations to fully co-registered DEMs. The dynamic and static corrections are tides, mean dynamic topography, inverse barometer effect, and referencing to the geoid. The asterisk (*) denotes intermediate CryoSat-2 and REMA data sets, before merging the two and applying the two-fold co-registration as described in Sect. 2.4.2. One being with respect to the CryoSat-2 elevations and the other with respect to overlapping strips from the same period.

in the longitudinal direction should be at least 10 km apart. This third criterion ensures that the CryoSat-2 measurements are evenly distributed over the REMA strip. This is a rather conservative threshold, which may filter out smaller but good-quality REMA strips. However, in this way we ensure the best possible DEM quality, which is crucial to resolve small-scale features.
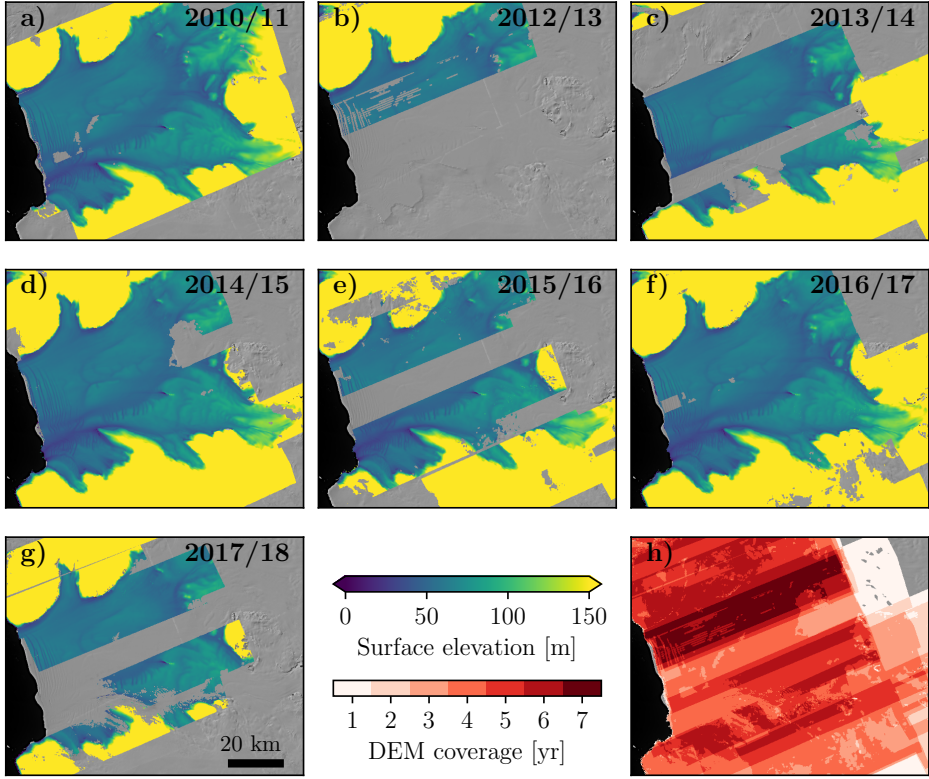
Figure 2.3: Yearly co-registered DEM mosaics ranging from 2010/11 **(a)** to 2017/18 **(g)**. Notice that there is no data from 2011/12. **(h)** Heat map showing the total DEM coverage.

The second co-registration is performed on a yearly basis by co-registering all DEMs that overlap at least 25% with the yearly median DEM. The yearly median DEM is the median of all overlapping REMA DEM strips per year, with 1 July defined as the first day of the year. The residuals between the DEM strips and the median DEM are thus used to perform the plane fit. The second co-registration is thereby not applied to all strips.

The co-registered DEM strips range from austral summer 2010/11 to 2017/18 and have a yearly coverage of up to 98% in 2016/17 (see Fig. 2.3).

2.4.3   Eulerian elevation change

Besides the Lagrangian elevation change which is needed to calculate the basal mass balance, we also assess the elevation change in a Eulerian framework. This provides information about where the ice shelf is thinning and thickening.

The Eulerian elevation change is calculated as a linear trend on a tri-yearly basis and throughout the entire study period. A tri-yearly period is chosen as the highest temporal resolution due to the limited to no DEM coverage in 2011/12 and 2012/13 (Fig. 2.3), along with the limited coverage of the center part of the ice shelf in 2015/16 and 2017/18 (Fig. 2.3). In this study, 1 July is defined as the start of the year, putting the austral summer in the middle of a year, with the first year of our study period being 2010/11 and the last year 2017/18. The Eulerian elevation change is thus calculated from the co-registered DEMs by applying a linear fit to the DEM strips and their corresponding time stamp, where the latter may vary from pixel to pixel. This implies that both the tri-yearly and entire study period trends are produced from all strips available in the period considered. The Eulerian elevation change is further cleaned from possible outliers by removing points with a surface elevation change rate of more than ± 15 m yr^{-1}.

2.4.4 Divergence of the velocity field

Berger et al. (2017) illustrated the impact different methods of calculating the velocity gradients have on the resulting divergence. They found regularized divergences (Chartrand, 2011) to be the best choice, since this method suppresses noise while keeping the data signal (Chartrand, 2011; Berger et al., 2017). In this study we use total-variation regularization (Chartrand, 2017), which is an updated version of the regularization method presented in Chartrand (2011) made especially for multidimensional data, to compute the gradients of the 120 m resolution ITS_LIVE velocity field. Due to our previous assumption of a constant velocity field in time, we also assume that the resulting divergence field of Dotson is constant in time. Finally, the divergence field is linearly interpolated onto the DEM grid.

2.4.5 Lagrangian elevation change and basal melt rate

As for the Eulerian elevation change, both the Lagrangian elevation change and the basal mass balance are calculated on a tri-yearly basis and as a linear trend throughout the entire study period. The whole process of obtaining the Lagrangian elevation change from the co-registered DEM strips and further steps to assess the basal mass balance is shown in Fig. 2.4 and is further outlined in this section.

The Lagrangian displacement is performed on a yearly basis using 1 July as the start of the year, putting the austral summer in the middle of a year. Together with the DEM strips, we also displace the velocity divergence and the nearest 10-daily firn air content from IMAU-FDM (Fig. 2.4b).

The most common approach to perform the Lagrangian displacement of DEMs is using a velocity field (i.e., Moholdt et al., 2014) or applying a feature tracking algorithm (i.e., Berger et al., 2017). The first approach requires velocities of high quality and resolution and puts strong restrictions on the spatial resolution of the final product. It is, however, computationally efficient, whereas the latter approach is computationally heavy but allows for a higher output spatial resolution. In BURGEE we want to keep the spatial resolution high, while keeping the computational cost low to allow for future
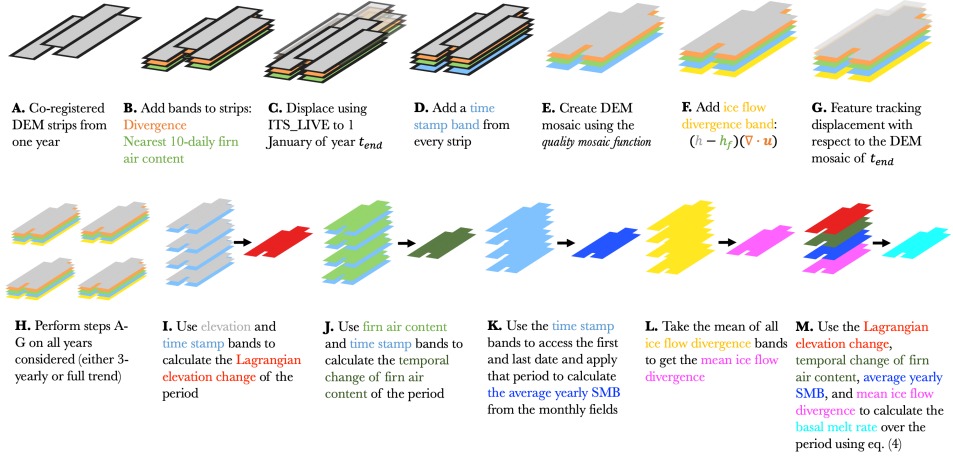
2

A. Co-registered DEM strips from one year

B. Add bands to strips: Divergence Nearest 10-daily firn air content

C. Displace using ITS_LIVE to 1 January of year t_{end}

D. Add a time stamp band from every strip

E. Create DEM mosaic using the *quality mosaic function*

F. Add ice flow divergence band: $(h - h_f)(\nabla \cdot \boldsymbol{u})$

G. Feature tracking displacement with respect to the DEM mosaic of t_{end}

H. Perform steps A-G on all years considered (either 3-yearly or full trend)

I. Use elevation and time stamp bands to calculate the Lagrangian elevation change of the period

J. Use firn air content and time stamp bands to calculate the temporal change of firn air content of the period

K. Use the time stamp bands to access the first and last date and apply that period to calculate the average yearly SMB from the monthly fields

L. Take the mean of all ice flow divergence bands to get the mean ice flow divergence

M. Use the Lagrangian elevation change, temporal change of firn air content, average yearly SMB, and mean ice flow divergence to calculate the basal melt rate over the period using eq. (4)

Figure 2.4: The workflow used to go from co-registered DEM strips in panel **(a)** to Lagrangian displaced DEM mosaics in panel **(g)**, with all Lagrangian displaced mosaics in panel **(h)** used to assess the Lagrangian elevation change in panel **(i)** and the basal melt rate in panel **(m)**.

study region upscaling. To do so, we first apply a velocity displacement, after which we perform a final correction through feature tracking. This decreases the search window needed in the feature tracking process, thus reducing the computational time.

The initial displacement of the DEM strips is performed by using the ITS_LIVE surface velocities, where all DEMs from the year considered are displaced to 1 January of the final year (t_{end}) in the trend period (Fig. 2.4c). For the Lagrangian elevation change of the entire period, t_{end} is thus 1 January 2018, and for the tri-yearly 2010/11-2013/14, t_{end} will be 1 January 2014. This means that all DEMs are roughly aligned to where they would be located at t_{end}. However, surface features such as crevasses may not be perfectly aligned, for which the second displacement is needed.

Before the second displacement is performed, all DEM strips are accompanied with a time stamp band (Fig. 2.4d), and a DEM mosaic of the given year is created using the *quality mosaic function* in GEE (Fig. 2.4e). This is done to reduce the computational requirements of the feature tracking algorithm. The resulting elevation, firn air content, and velocity divergence mosaics are used to add an ice flow divergence band (Fig. 2.4f) according to the ice flow divergence term $((h - h_f)(\nabla \cdot \boldsymbol{u}))$ in Eq. (2.4).

This second and final displacement is performed by using the built-in feature tracking algorithm *displacement* in GEE, which uses orientation correlation. In this displacement, the DEM mosaic of the given year is referenced to that of t_{end}, thereby aligning all surface features to their position in the DEM mosaic from t_{end} (Fig. 2.4g). The built-

2. Unveiling Spatial Variability within the Dotson Melt Channel through High-Resolution Basal Melt Rates from the Reference Elevation Model of Antarctica

2

in feature tracking algorithm on the GEE takes in three adjustable parameters: patch width, max offset, and stiffness, which were set to 100 m, 300 and 3, respectively. The patch width defines the size of the patches/regions to search for within the distance given by max offset, whereas the stiffness parameter defines how much distortion/warping is allowed. Since ice features may very well change in shape, a lower less rigid stiffness parameter is desired.

The above-mentioned steps (Fig. 2.4a-g) are then performed on all years considered, and the Lagrangian elevation change using the displaced DEM mosaics is then obtained similarly to the Eulerian elevation change by applying a linear fit to the DEM mosaics and their corresponding time stamp (Fig. 2.4i), which in this case may vary from pixel to pixel. The same outlier criterion of 15 m yr^{-1} is used to mask out the remaining possible outliers. This filter could possibly filter out fast, small-scale processes like rift opening, which is acceptable for this study, given our focus on the basal melt rates.

To calculate the final basal melt rate using Eq. (2.4), the change of firn air content with time is calculated using the time and firn air content bands (Fig. 2.4j). Furthermore, the time stamp bands are used to access the first and last date of the given period (full study period or 3-yearly period) and use those as limits to calculate the average yearly surface mass balance from the monthly RACMO fields within the period limits (Fig. 2.4k). Also, a mean of all ice flow divergence bands is taken to get the mean ice flow divergence of the period (Fig. 2.4l). Joining all of this with the Lagrangian elevation change and the constant densities for ice and seawater allows for the basal melt rate to be calculated over the desired period (Fig. 2.4m). As for the Eulerian elevation change (Sect. 2.4.3), this implies that both the tri-yearly and entire study period trends are produced from all strips available in the period considered and that some pixels may not have data from all years considered.

2.4.6   Sensitivity experiment

Since the signal-to-noise ratio of basal mass balance is expected to increase when refining the spatial posting, we performed a synthetic experiment to assess the impact of spatial posting on the basal melt rate in BURGEE. The sensitivity experiment is based on the assumption that the Lagrangian displacement is one of the main contributors to the basal melt rate uncertainty. Within this experiment we used the aligned annual DEM mosaics from 2010/11 and 2014/15, since they have a high coverage and are relatively far apart in time, thus placing stronger requirements on the displacement algorithm applied. Based on both aligned annual DEM mosaics, two different basal mass balance maps are obtained using two different Lagrangian elevation changes. This is first done from the aligned DEM mosaics resulting in the *true* basal melt rate. Second, the otherwise aligned 2010/11 DEM mosaic is displaced based on the 4-year accumulated ITS_LIVE error fields to create an alternative aligned DEM mosaic that incorporates the displacement uncertainty due to velocity errors. The Lagrangian elevation change is then calculated using the error-displaced 2010/11 DEM mosaic and the previously mentioned 2014/15 DEM mosaic. The difference between the resulting basal melt rates following from the two Lagrangian elevation changes is then calculated at a 50, 100,

250, and 500 m posting to see what posting is required for the artificial error to cancel out. The 500 m posting corresponds to what has been used when using CryoSat-2 alone (Gourmelen et al., 2017) and therefore serves as our most coarse limit.
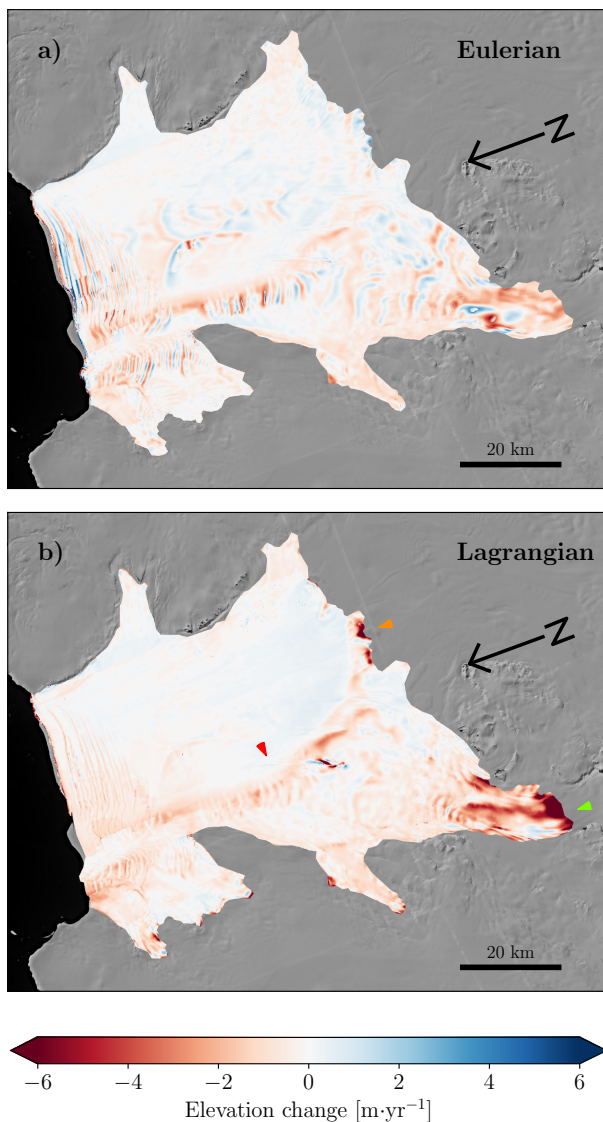

Figure 2.5: Eulerian **(a)** and Lagrangian **(b)** surface elevation trends from 2010/11-2017/18 at a 50 m posting. The red arrow marks the main channel, the green arrow marks the Kohler grounding zone, and the orange arrow marks the high elevation changes towards the Crosson Ice Shelf.

2.5 Results

2.5.1 Evaluation of BURGEE results

The Eulerian and Lagrangian surface elevation trends over the entire study period (2010/11-2017/18) are shown in Fig. 2.5 at a 50 m posting. Owing to its along-flow coordinate system, the Lagrangian elevation change has a much smoother pattern compared to the Eulerian framework. In both frameworks, the channel described by Gourmelen et al. (2017) (red arrow), which we will refer to as the Dotson Melt Channel hereafter, shows pronounced thinning. The Eulerian elevation change shows elevation decrease along and west of the Dotson Melt Channel, whereas the area east of this channel shows a more irregular pattern. Similarly, we see almost no elevation change in this eastern zone in the Lagrangian elevation change and a smoother pattern due to the along-flow framework. Three areas stand out with high Lagrangian elevation changes, namely the Dotson Melt Channel (red arrow), at the border towards the Crosson Ice Shelf (orange arrow), and the grounding zone at the inflow of the Kohler Glacier (green arrow). The latter is not fully resolved in Gourmelen et al. (2017), presumably due to limited CryoSat-2 coverage (Fig. 2.1).

The basal melt rate at a 50 m posting over the entire study period can be seen in Fig. 2.6a, which shows a similar pattern to the Lagrangian elevation change. Figure 2.6d-h show the 3-yearly basal melt rate trends also at a 50 m posting. There is a clear spatial consistency throughout the entire period, though melt rate magnitudes do seem to show temporal variability. A striped pattern is visible on some of the 3-yearly maps (e.g., 2011/12-2014/15, Fig. 2.6e and 2012/13-2015/16, Fig. 2.6f) due to the DEM mosaic coverage seen in Fig. 2.3. The varying coverage also implies that the trend is taken over different time periods whenever there is missing data in the DEM mosaics and that gaps may occur if less than 2 years of data are available. Furthermore, the Lagrangian displacement is performed with respect to the latest DEM mosaic (Sect. 2.4.5), which is what is causing the higher melt rates in the center of Dotson in the 2012/13-2015/16 product. Focusing on the basal melt rate of the entire study period (Fig. 2.6a) we see that high melt rates are present along the Dotson Melt Channel (red arrow), with a melt convergence zone just east of a pinning point (cyan arrow), near the Kohler grounding zone (green arrow), and towards the Crosson Ice Shelf (orange arrow). These are all features that are present in both Gourmelen et al. (2017) (Fig. 2.6b) and Lambert et al. (2022) (Fig. 2.6c). Likewise, the overall pattern is similar in all three products. A slight exception to this is the melt signal near the calving front seen in BURGEE. Here, there are large crevasses and fractures in the ice shelf, which may not be well represented in the divergence signal when assessing the basal melt rate at a 50 m posting. Overall, BURGEE allows us to derive melt rates of all parts of the ice shelf, compared to the limited coverage especially near the ice shelf margin for Gourmelen et al. (2017).
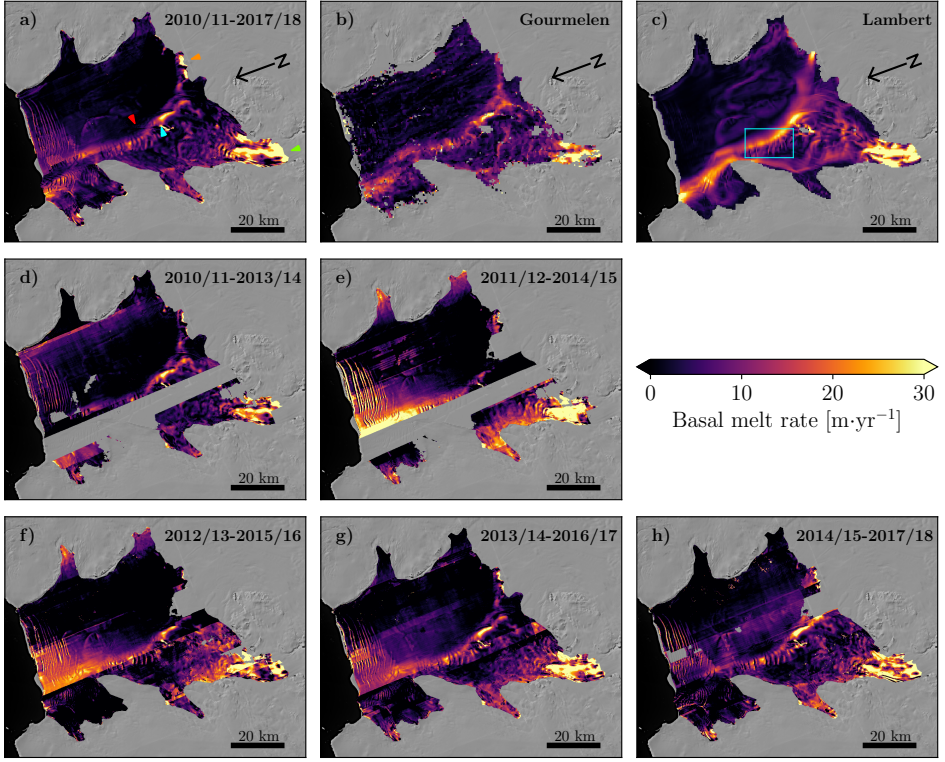
2

Figure 2.6: **(a)** Basal melt rate trend from 2010/11 to 2017/18. The arrows point out the Dotson Melt Channel (red), the pinning point below the ice shelf (cyan), the Kohler grounding zone (green), and the high melt rates near the Crosson Ice Shelf. **(b)** Basal melt rate from Gourmelen et al. (2017). **(c)** Basal melt rate from Lambert et al. (2022) with the box marking the zoom-in in Fig. 2.9. **(d-h)** Tri-yearly basal melt rate trends.

2.5.2 Results from the sensitivity experiment

Figure 2.7 shows the result of the sensitivity study where we created an alternative aligned DEM mosaic by displacing the correctly aligned DEM based on the error of the ITS_LIVE velocities under the assumption that the quality of the Lagrangian displacement is the main contributor to the basal mass balance uncertainties. In the part of the ice shelf with fewer surface undulations (distances 10-15 km of the B-BB cross section), the basal melt rate differences resulting from the artificial displacement cancel out to a large degree already at a 50 m posting. In areas with stronger surface undulations, it requires a coarser posting for the differences to cancel out. However, it should be noted that even at a high posting of 50 m, the resulting differences in basal melt rates of the cross section are within ± 4 m yr^{-1}. Furthermore, the largest differences correlate with high melt rates. Based on these findings, we have chosen to offer our product at a

2. Unveiling Spatial Variability within the Dotson Melt Channel through High-Resolution Basal Melt Rates from the Reference Elevation Model of Antarctica

2
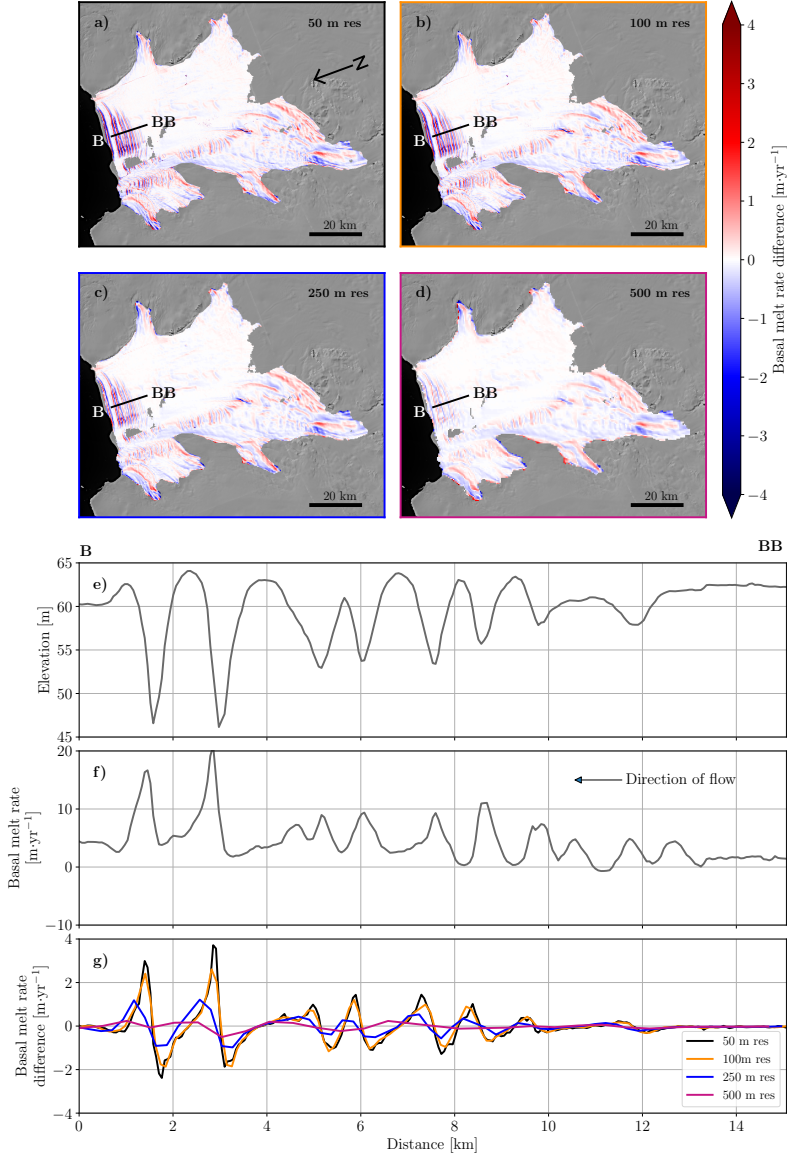
Figure 2.7: **(a-d)** The difference between the basal melt rate obtained from the correct and the erroneous Lagrangian elevation changes at 50 m **(a)**, 100 m **(b)**, 250 m **(c)**, and 500 m **(d)** postings. **(e)** The perfectly aligned 2010/11 DEM mosaic at the B–BB cross section. **(f)** The basal melt rate obtained from the correct DEMs at the B–BB cross section. **(g)** The basal melt rate differences at the B–BB cross section at 50, 100, 250, and 500 m postings. Note that panels **(f)** and **(g)** use a different range on the *y* axis.
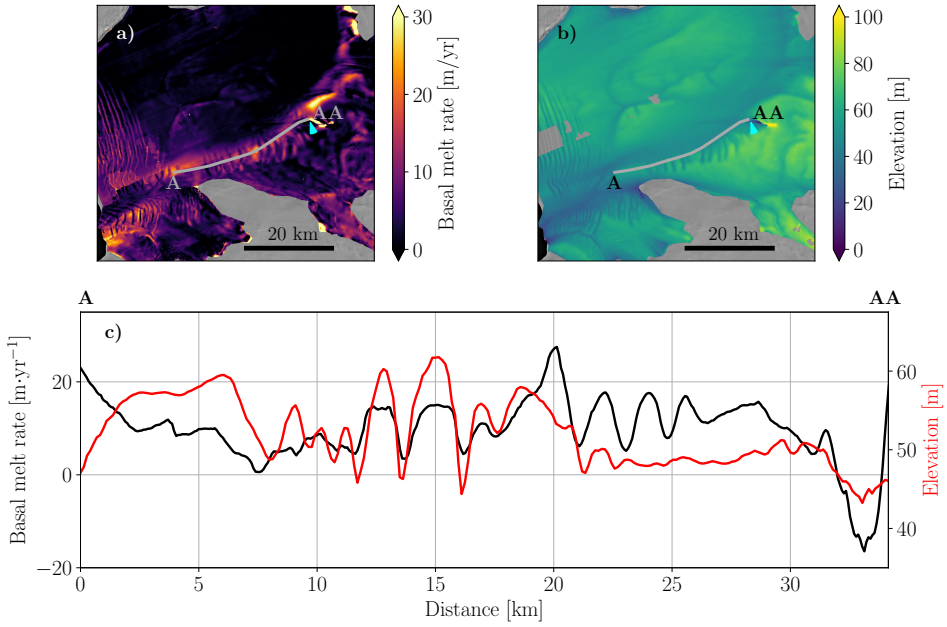
Figure 2.8: **(a)** Basal melt rate from 2010/11-2017/18; **(b)** 2016/17 DEM, with the gray line marking the cross section A to AA in panel **(c)**; **(c)** surface elevation from the 2016/17 DEM (red line), prior to any Lagrangian displacement, and basal melt rate (black line) at the cross section marked in panel **(a)** and **(b)**. The distance in panel **(c)** is with respect to the left end point (A) of the gray line in panel **(a)** and **(b)**.

50 and a 250 m posting (`https://doi.org/10.4121/21841284`, textbfREMEMBER PROBER REF to dataset). It should be noted, however, that the Lagrangian displacement is not the only error source, since all data and assumptions used to calculate the basal mass balance (Eq. (2.4)) come with errors and uncertainties, which is why these numbers cannot be considered as true uncertainties of the final product.

2.5.3   Interpretation of the melt pattern

In the vicinity of the pinning point (2.6a, cyan arrow), the basal melt within the Dotson Melt Channel shows a smooth pattern which changes to a more wavey pattern downstream. Roberts et al. (2018) hypothesize that such a wavey pattern can originate near pinning points due to ocean heat variability, where periods of increased available ocean heat induce enhanced thinning and a reduced back stress over the pinning point and vice versa. Through convergence and divergence, the resultant temporal variability in ice speed translates into an alternating pattern of thick and thin ice. To investigate the influence of the pinning point on the spatial melt variability within the Dotson Melt Channel, we have focused on a transect following the basal channel from the pinning point to the ice shelf front (Fig. 2.8, transect A to AA and pinning point marked with

the cyan arrow). We can see clear surface undulations along the Dotson Melt Channel that emerge downstream from the pinning point. We also notice higher melt rates coinciding with these surface undulations, especially around 12-22 km, where we see that higher melt rates align with higher surface elevations, implying deeper basal drafts, and vice versa.

To investigate the relation between the surface undulations and the basal melt rate, we disentangle basal melt into its two major components: thermal forcing and friction velocity. The thermal forcing determines the locally available heat for melting, whilst the friction velocity determines the efficiency of turbulent heat exchange toward the ice shelf base. The thermal forcing and friction velocity, simulated by LADDIE, are shown in Fig. 2.9, along with the LADDIE basal melt rates and draft. A direct comparison between the LADDIE thermal forcing and friction velocity with the BURGEE melt rates cannot be done, since LADDIE is forced with a different ice shelf geometry; therefore, we compare to the LADDIE melt rates instead. Figure 2.9e-f further shows the friction velocity and the thermal forcing as a function of the melt rate, respectively. It is evident that the friction velocity has a high correlation with the melt rate, implying that it is the main driver of spatial melt variability at fine scales. The friction velocity is affected by the undulations. Where the meltwater plume encounters thick ice, it is squeezed vertically, leading to convergence and a local acceleration. This locally enhanced friction velocity increases the heat transfer and consequently the basal melt. As basal melt is typically highest in regions of thick ice (Fig. 2.8), this interaction between ice topography and melt is a negative feedback that should smoothen out the undulations downstream. This negative feedback may explain the weakening signature of the undulations towards the ice shelf front.

2.6   Discussion

We show how REMA in combination with CryoSat-2 is capable of obtaining high-resolution basal melt rates of the Dotson Ice Shelf. The use of CryoSat-2 and Google Earth Engine in BURGEE allows us to process significantly more REMA strips than if using Operation IceBridge alone, and it allows for fast computations. We observe the same large-scale melt pattern consisting of one wide melt channel (Dotson Melt Channel) as previous studies (Gourmelen et al., 2017; Lambert et al., 2022). Additionally, BURGEE allows us to observe small-scale melt features which would go unnoticed in lower-resolution altimetry-based products such as Gourmelen et al. (2017) and Adusumilli et al. (2020). This especially becomes evident within the Dotson Melt Channel.

Our elevation maps reveal that surface undulations appear downstream of a pinning point on the ice shelf. Here, we also find a correlation between melt rates and ice thickness along the Dotson Melt Channel. The link between surface undulations and basal melt rates is further supported by Watkins et al. (2021), who found a clear relationship between pinning points and roughness and a correlation between the latter and basal melt. Furthermore, modeling studies suggest shear zones and topographic features have
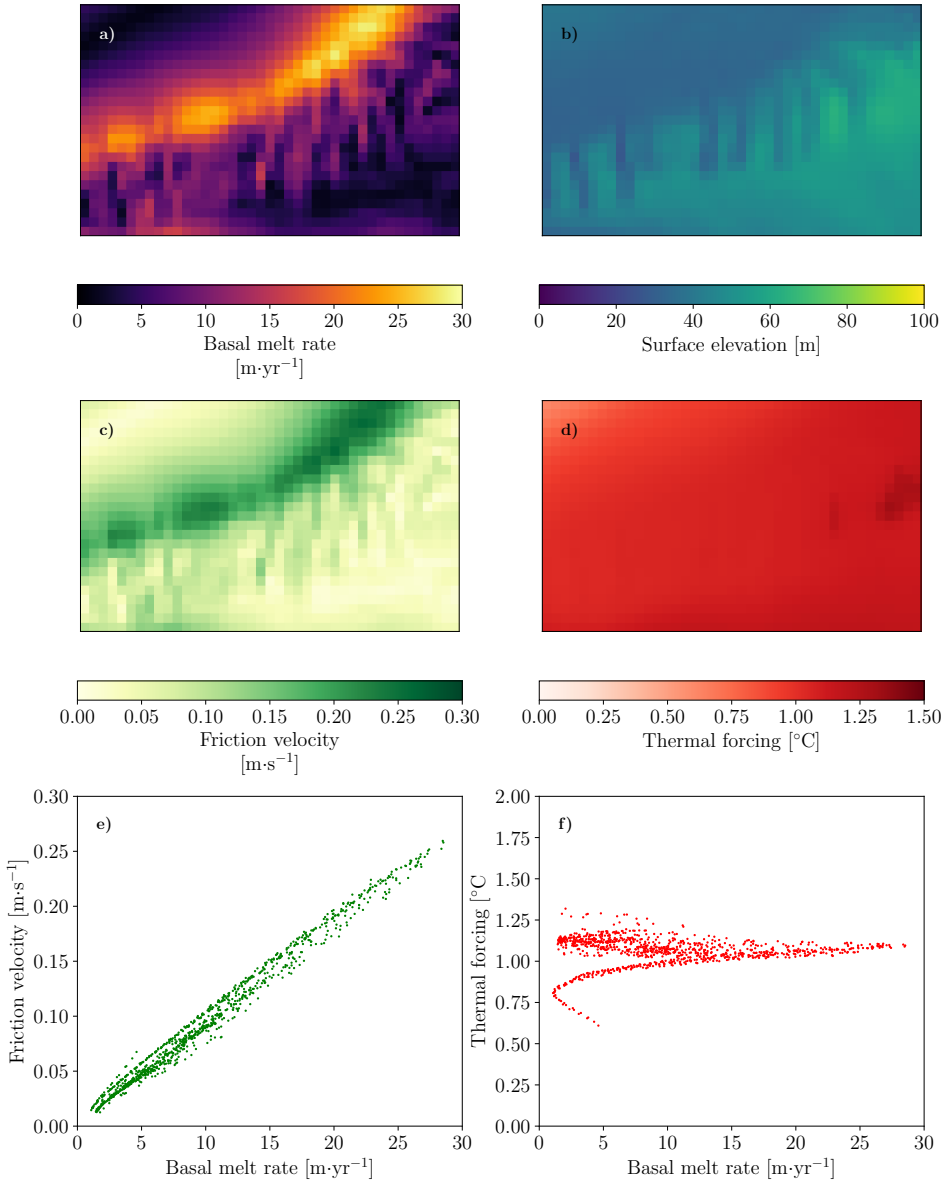
Figure 2.9: Model outputs from LADDIE within the box marked in Fig. 6c: **(a)** basal melt, **(b)** surface elevation, **(c)** friction velocity, **(d)** thermal forcing, **(e)** friction velocity as a function of basal melt, and **(f)** thermal forcing as a function of basal melt.

a possible impact on basal channels and their formation (Gladish et al., 2012; Sergienko, 2013). Also, Roberts et al. (2018) suggest that varying ocean temperatures lead to ice shelf thickness change and thereby a change in the back stress over ice rumples causing

2. Unveiling Spatial Variability within the Dotson Melt Channel through High-Resolution Basal Melt Rates from the Reference Elevation Model of Antarctica

2

a wavey pattern as the one we observe being initialized at the pinning point. Model output from LADDIE suggests that the friction velocity is the driver of the increased melting in regions of greater ice thickness, due to compression and divergence of the melt plume. The large-scale pattern of the Dotson Melt Channel, bending towards the western margin of the ice shelf, is explained by buoyancy forcing of the low-salinity meltwater plume (Lazeroms et al., 2018). However, just eastward of the pinning point, a convergence zone, causing a narrow sharp plume with high melt rates, indicates that the Dotson Melt Channel pathway may also be influenced by the pinning point. Meltwater plumes causing channel formation have a tendency to occur at western topographic boundaries in this area of Antarctica (Lambert et al., 2022). The eastward melt convergence zone suggests that the pinning point is big enough to act as a western topographic feature. Without the pinning point the meltwater plumes may thus converge elsewhere. We therefore postulate that the pinning point impacts the spatial variability within the Dotson Melt Channel and possibly also the channel pathway due to the convergence zone just east of the pinning point.

Varying basal melt rates can also be seen within the Dotson Melt Channel in Gourmelen et al. (2017), but due to the coarser resolution and gaps in the data, it is not clear whether this variation is (partially) due to noise or actual signal. This underlines the importance of high-resolution basal melt rates.

Finally, the spatial coverage is improved when using a combination of REMA and CryoSat-2. CryoSat-2 on its own cannot cover all parts of an ice shelf, especially those surrounded by topographic features such as mountains. Furthermore, we can assess temporal changes on a 3-yearly basis but with poorer coverage than the full trend due to the yearly REMA coverage. Using elevation data from the CryoSat-2 swath mode alone (Gourmelen et al., 2017) would likely yield a higher temporal resolution but would not resolve the small-scale features which we can capture with BURGEE. Adusumilli et al. (2020) used a wide range of remotely sensed surface elevations to obtain basal melt rates at quarter-yearly resolution but at the cost of the spatial resolution. The Dotson Ice Shelf did not show noticeable changes in basal melt over the study period; however, ocean observations from the Dotson Ice Shelf cavity do show variations on seasonal timescales of inflow of warm Circumpolar Deep Water (Jenkins et al., 2018; Yang et al., 2022). This could imply seasonal variability in the basal melt rates, as has been observed at both the Nivlisen Ice Shelf in East Antarctica (Lindbäck et al., 2019) and the Filchner-Ronne Ice Shelf (Vaňková and Nicholls, 2022). To investigate seasonal changes using BURGEE, more DEMs than currently available from REMA would be needed. If REMA-2 or similar data products based on future missions were to provide such a higher temporal coverage, studying seasonal or interannual variations in basal melt would become within reach with BURGEE.

The clear advantage of BURGEE is the high spatial resolution and the use of Google Earth Engine. The latter allows one to efficiently and rapidly process large amounts of data, while the built-in data catalogue drastically reduces the amount of data which has to be downloaded locally. Furthermore, the choice for no site-specific tuning allows the methodology to be easily applied to other ice shelves in Antarctica. By incorporating

upcoming and more up-to-date elevation data sets, we might then be able to assess basal melting at 50 m posting and at greater temporal resolution than 3 years. By doing so to other ice shelves influenced by pinning points, our product may also help answer what the effect of those are on the basal melt pattern. But, more importantly, it would help us to assess the (in)stability of other ice shelves and locate weak spots on them.

2.7   Conclusions

In this study we have shown that the Reference Elevation Model of Antarctica can be used to obtain high-resolution surface elevation changes and basal melt rates of the Dotson Ice Shelf. We perform a sensitivity study which supports the trustworthiness of the observed small-scale features. It further indicates that a 50 m spatial posting of basal melt is feasible. BURGEE reveals spatial variability within the Dotson Melt Channel, which was not fully resolved in coarser remote sensing products. We find strong indications that a pinning point on the ice shelf influences this spatial melt variability within the Dotson Melt Channel and that it may be controlling the position of a warmer ocean plume, thereby impacting the pathway of the Dotson Melt Channel. This underlines the importance of high-resolution basal mass balance products as our product can help future studies to provide answers to the causes behind them.

Finally, BURGEE contains no site-specific tuning, which means that it can easily be applied to other ice shelves. Of course, our assumption of a constant velocity field in time does not hold for all ice shelves and should thus be adjusted. Nonetheless, with the right computing sources, this study could be upscaled to a pan-Antarctic study of high-resolution basal mass balances.

Code and data availability

The BURGEE code is available on GitHub (`https://github.com/aszinck/BURGEE`, Zinck, 2023). Both elevation and velocity data are publicly available: REMA (`https://www.pgc.umn.edu/data/rema/`, Howat et al., 2019), CryoSat-2 (`https://earth.esa.int/eogateway/documents/20142/37627/CryoSat-Baseline-D-Product-Handbook.pdf`), and ITS_LIVE (`https://doi.org/10.5067/6II6VW8LLWJ7`, Gardner et al., 2022). Derived surface elevation changes and basal melt rates are available from `https://doi.org/10.4121/21841284`.
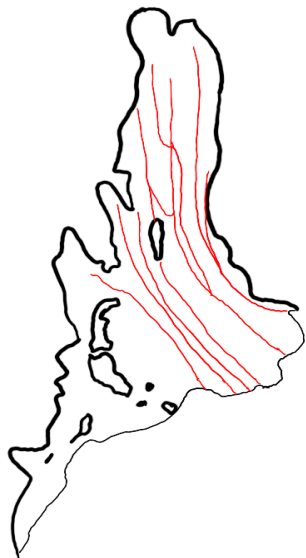
Chapter 3

Exposure to Underestimated Channelized Melt

While of critical importance for coastal communities, Antarctica's future sea level contribution remains highly uncertain. This uncertainty largely stems from the complex interaction between the ocean and the ice shelves, which is both difficult to observe and model. To better understand and constrain land ice response to a reduced buttressing exerted by ice shelves, efforts are needed to fully comprehend basal melt rates and their impact on ice shelf weakening and retreat. Here, we present high-resolution basal melt maps (50 m) of vulnerable ice shelves based on a combination of stereo imagery and satellite altimetry, revealing pronounced channelized melting patterns whose melt rates were previously substantially underestimated (42-50%). This underestimation in melt rates implies that channel breakthrough times have been underestimated, making breakthrough more likely and ice shelves more susceptible to damage. Accurately simulating small-scale dynamics in ice-sheet models remains challenging but is essential for accurate sea level rise projections.

The evolution of the Antarctic Ice Sheet poses a major uncertainty in sea level rise projections, driven largely by the uncertain response of its ice shelves and tributary glaciers to atmospheric and oceanic forcing in a changing climate (Pattyn and Morlighem, 2020; IPCC, 2023; Bamber et al., 2022; van de Wal et al., 2022). Ice shelf thinning and weakening due to basal and surface melting affect the timing and magnitude of ice mass loss as they directly impact the ability of the ice shelf to buttress inland ice (Pattyn and Morlighem, 2020; van de Wal et al., 2022; Pattyn et al., 2018). In a warming climate, as the risk of reduced ice-shelf buttressing increases, certain regions of the ice sheet could approach tipping points of irreversible mass loss (Pattyn and Morlighem, 2020). The primary contributors to ice shelf weakening are surface and basal melting, and damage (crevasses and fracturing). Basal melting is a key concern, as increasing ocean temperatures – with some projections suggesting up to a tripling of historical levels over the twenty-first century – along with potential changes in ocean circulation, are expected to intensify subsurface heat transport toward the ice shelves in the future (Pattyn et al., 2018; van de Wal et al., 2022; Naughten et al., 2023).

Repeat observations of ice-shelf surface elevation change from satellite altimeters have enabled the estimation of basal melt rates for most Antarctic ice shelves at a resolution of 500 m to 1 km (Adusumilli et al., 2020; Davison et al., 2023), revealing that basal melting not only varies in time (Adusumilli et al., 2020), but is also the primary contributor to mass reduction in ice shelves experiencing the highest losses (Davison et al., 2023). Meanwhile, studies focusing on single ice shelves have shown that the combination of satellite stereo imagery and altimetry allows ice-shelf basal melting to be calculated at significantly higher resolution (32-50 m), uncovering previously unseen small-scale features, such as spatial variability within the melt channel on the Dotson Ice Shelf (Shean et al., 2019; Zinck et al., 2023). These enhanced details, missed earlier by products relying on satellite altimetry (Gourmelen et al., 2017), offer valuable new insights into the processes driving basal melting and the potential consequences for ice shelf weakening.

Basal melting of ice shelves typically initiates at deep grounding zones and extends into basal channels, where plumes carve troughs in the ice base (Alley et al., 2016, 2022). Basal channels are widespread in Antarctica, particularly in warm cavity ice shelves (Alley et al., 2016), yet only a few have been thoroughly studied for their spatial (Zinck et al., 2023; Alley et al., 2024) and temporal (Chartrand and Howat, 2020; Alley et al., 2024) variations and their impact on ice shelf integrity (Alley et al., 2022, 2024; Chartrand et al., 2024). Although so far there are no observations of channel breakthrough solely driven by basal melt, there is evidence of channel incisions leading to large-scale fracturing and ice shelf retreat (Dow et al., 2018; Alley et al., 2022; Chartrand et al., 2024). Studies modelling the ice-shelf response to basal melting suggest that high melt rates in basal channels can lead to a complete breakthrough (Wearing et al., 2021; Humbert et al., 2022).

There are many important aspects of basal channel evolution that we do not fully understand, such as the feedback with ice shelf fracturing and details of ocean melting (and freeze-on) in channels (Alley et al., 2022). However, improved observations of melt

patterns in basal channels is crucial to quantify ongoing change and validating models.

In this study we present for the first time a high-resolution (50 m posting) basal melt rate product covering multiple ice shelves, in particular those which are rapidly melting (Adusumilli et al., 2020; Davison et al., 2023), are located in areas with high ice mass loss (Davison et al., 2023) and have a high sea level rise potential (Seroussi et al., 2020). These are also the regions where the highest density of basal channels have been observed (Alley et al., 2016) and thus the most vulnerable to channel-induced weakening. We obtain basal melt rates using a combination of stereo imagery and satellite altimetry and show that in many vulnerable locations, melt rates have previously been underestimated in altimetry-only estimates. Furthermore, we discuss the implications of this underestimation on channel breakthrough times and ice shelf weakening.

3.1   Underestimated channelized melting

We compute ice shelf basal melting at high-resolution (50 m posting) for the period 2010-2017, by combining stereo imagery from the Reference Elevation Model of Antarctica (REMA) and CryoSat-2 altimetry using a mass conservation approach. This approach - Basal melt rates Using REMA and Google Earth Engine (BURGEE, Sect. 3.4.1) - has been used previously to generate high-resolution basal melt rates of the Dotson Ice Shelf (Zinck et al., 2023). In the design of BURGEE, no specific site-tuning was applied (Zinck et al., 2023), which implies that the only limitation of applying BURGEE on other ice shelves are data availability and potentially computational constraints.

We compare BURGEE melt rates with those of two altimetry-only studies; Adusumilli et al. (2020) (500 m resolution) and Davison et al. (2023) (1 km resolution), henceforth referred to as Adusumilli and Davison. Both make use of CryoSat-2 radar altimetry to obtain surface elevation changes. Opposed to the classical point-of-closest-approach method used by Adusumilli, Davison uses a swath processing (Gourmelen et al., 2018) which allows for increased spatial detail and coverage. BURGEE and the two altimetry studies are based on the concept of mass conservation in a Lagrangian framework (Methods), which implies that uncertainties related to factors other than the Lagrangian elevation change (e.g., surface mass balance, firn correction) are common across all products. Furthermore, all three methods assume hydrostatic equilibrium, which might be violated in the immediate vicinity of the grounding zone and hence might locally lead to overestimated melt rates.

Our results show that broad-scale (~10 km) ice shelf melt spatial patterns and magnitudes generated by BURGEE are consistent with those observed in earlier altimetry-only studies (Adusumilli et al., 2020; Davison et al., 2023) (Fig. 3.1 and A.1). The ice-shelf integrated total basal melt rate is comparable between all three products, with the exception of Pine Island, where BURGEE yields 50-90% (Davison-Adusumilli) higher total melt rates. The enhanced spatial detail of BURGEE reveals more pronounced channelized melting (e.g., Moscow University and Totten) and agrees with earlier results based on stereo-imagery and altimetry for Pine Island Ice Shelf (Shean et al., 2019) (Fig. A.2).
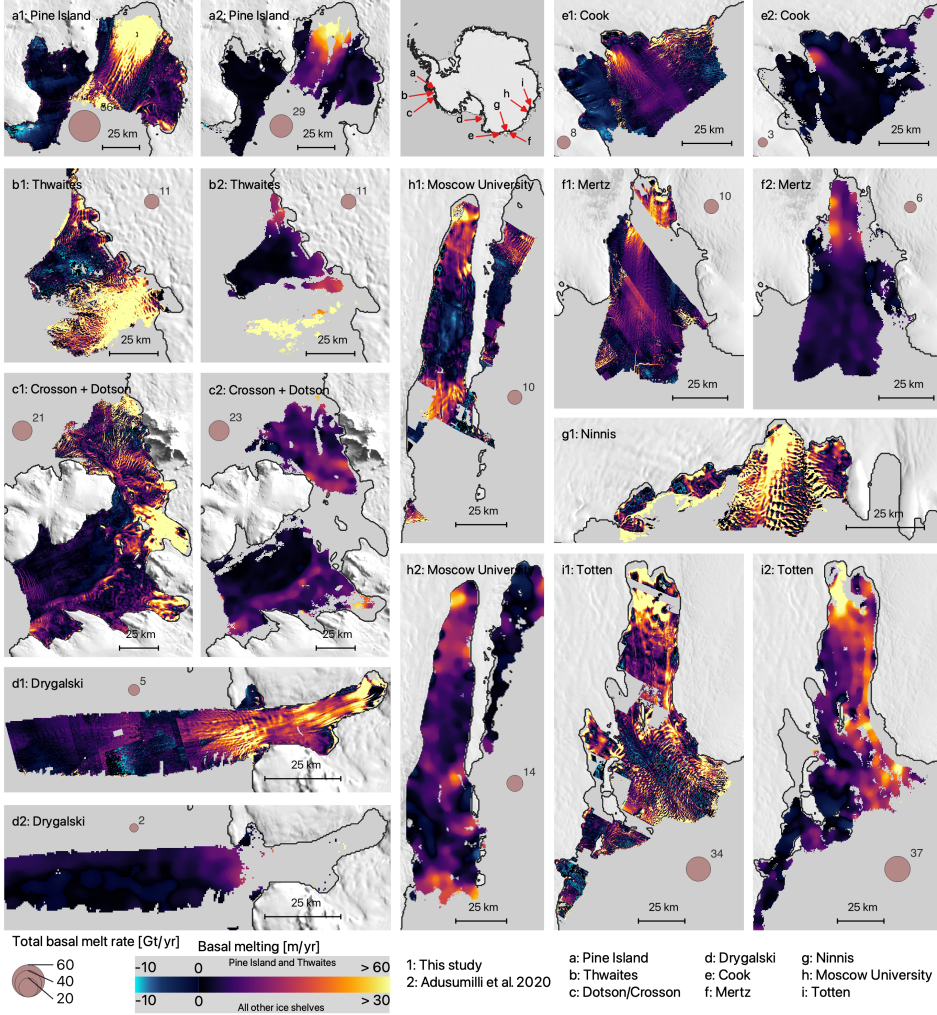
Figure 3.1: **Basal melt rate comparison**. Basal melt rates from this study are marked with 1 and melt rates from Adusumilli are marked with 2. The Ninnis ice shelf **(g)** is not covered by Adusumilli et al. (2020). The black line denotes the BedMachine V3 grounding line (Morlighem, 2022). The circles denote total ice-shelf wide basal melt rate in Gt/yr, only considering areas covered by both BURGEE, Adusumilli, and Davison.

Basal channels are expressed at the surface as depressions (Alley et al., 2024). Since the return echo of radar altimeters like CryoSat-2 naturally comes from the nearest terrain points, these depressions may be obscured and under-sampled when surrounded by significantly higher terrain, leading to an underestimate of melting (Fig. A.3). This can for instance be seen near the grounding zone of Drygalski Ice Shelf, which is unseen by CryoSat-2 because of the surrounding mountains (Fig. A.1). This could,
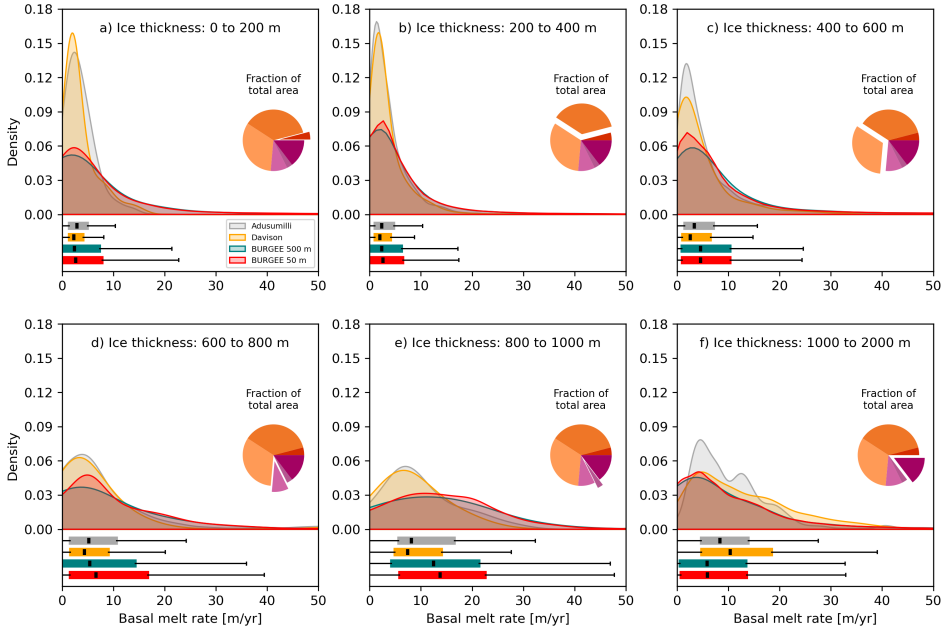
Figure 3.2: **Basal melt rate distributions**. Basal melt rate distributions of Adusumilli, Davison, and BURGEE melt rates, the latter at the original 50 m posting and interpolated onto the 500 m grid used in Adusumilli. Distributions are grouped by different ice shelf thickness sections based on BedMachine V3 (Morlighem, 2022) and only areas covered by all melting products are considered. In the lower subpanels, the thick, vertical black line represents the median melt rate, the solid box ranges from the first to the third quartile, and the whiskers extend the box to 1.5x the inter-quartile range.

further, explain the higher BURGEE total melt rate of Pine Island, where melting in along-flow channels dominates the melting signal (Fig. 3.1 and A.1). Such limitations are critical, given the importance of small-scale features for comprehensively understanding complex basal melting and its repercussions on ice shelf weakening. While Davison's use of swath processing (Gourmelen et al., 2018) allows for increased spatial detail as compared to Adusumilli, it does not fully resolve the problem of under-sampling deep surface depressions. The extent of underestimated melting is illustrated in Fig. 3.2. BURGEE reveals higher third quartile melt rates than both Davison (8 m/yr vs 4 m/yr) and Adusumilli (8 m/yr vs 5 m/yr) across areas where the ice shelf is thin (0-200 m). These thin ice areas often contain fractures and also coincide with the location of basal channels, such as the downstream section of the main basal channel on Dotson, and thus represent some of the weakest areas on the ice shelves (Fig. 3.3). Considering all studied ice shelf areas where ice thickness ranges from 200-400 m, BURGEE reveals higher third quartile melt rates (6 m/yr) than both Adusumilli (5 m/yr) and Davison (4 m/yr). This picture of higher third quartile melt rates using BURGEE is valid for all ranges of ice thickness up to 1000 m (Fig. 3.2) indicating that even thin ice, far away from
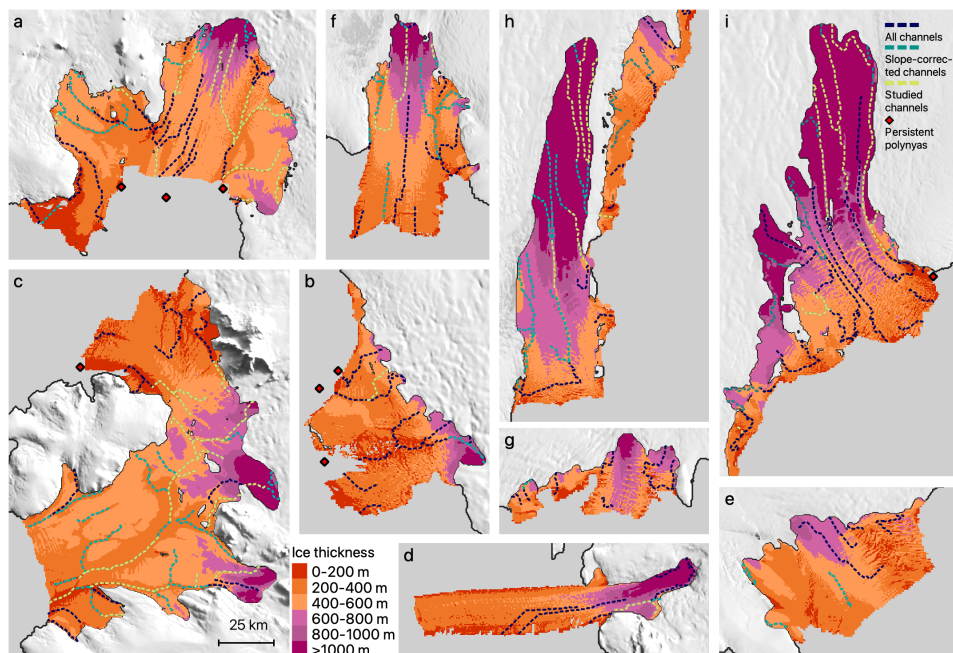
Figure 3.3: **Ice thickness and basal channels**. BedMachineV3 ice thicknesses (Morlighem, 2022) overlaid with detected channels (based on an accumulated flow approach, Sect. 3.4.5), slope-corrected channels (channels with maximum slopes $< 15°$, Sect. 3.4.5) and studied channels (channels where the 90% percentile melt rate is > 10 m/yr, Sect. 3.4.5). Persistent polynya locations are from Alley et al. (2019). Lettering corresponds to Fig. 3.1.

the deep grounding zones, is subject to high melt rates and these are underestimated in previous products. The similar distributions of BURGEE on a 50 m and 500 m (nearest neighbour) posting shows that underestimating melting is not a consequence of the product grid size (Adusumilli at 500 m and Davison at 1 km).

Furthermore, a Fourier analysis of the basal melt maps shows that only BURGEE explores the full range of basal melting wavelengths, which implies that BURGEE, unlike the altimetry-only studies, captures all melting present within the signal. This finding does not only support the potential underestimation of channelized melting, but also provides a wavelength (500 m) at which basal melting (or its impact) should be resolved in models (Sect. 3.4.8, Fig. A.4).

3.2 Channel breakthrough

Basal channels in thin ice areas (<600 m) that are subject to high melt rates are at risk of channel breakthrough (Wearing et al., 2021). Calculating breakthrough times can provide a framework to assess ice shelf weakness, as high channel incision in thin

ice areas may lead to critical weakening and initiate further damage. We therefore study the impact of enhanced channelized melting revealed by BURGEE on channel breakthrough – weakening indicator – in these potential weak zones in ice shelves. Linearly extrapolating channel melt rates has previously been used to estimate channel breakthrough times (Gourmelen et al., 2017). However, modelling work using a full-Stokes ice-flow model with idealized basal melting demonstrates that breakthrough can be slowed – and in some cases prevented – by secondary flow, i.e. the viscous inflow of ice towards the channel center induced by the gradient in ice thickness between the channel and the surrounding ice shelf (Wearing et al., 2021). These modelling results (Wearing et al., 2021) show that the primary factors influencing breakthrough times are the peak melt rate within the channel, and the ice shelf thickness outside of the channel (Wearing et al., 2021). In areas with thick ice (>600 m) secondary flow can balance melt-driven incision and prevent channel breakthrough. In areas of thinner ice (<600 m), where secondary flow cannot prevent channel breakthrough, the peak melt rate is a dominant control on how fast a channel can break through and thereby cause severe damage. The breakthrough time of a channel, and consequently the stability of the ice shelf, thus depends on the imbalance between the peak melt rate within the channel and secondary flow rates caused by ice thickness gradients.

To understand the implications of previously underestimated channelized melt rates on channel breakthrough times and weakening, we identify channels on all ice shelves included in this study (Sect. 3.4.5, Fig. 3.3). Channels with high slopes (maximum slopes > 15°; Sect. 3.4.5), which often coincide with damage (rifting and crevasses; Fig. A.5), are excluded (Fig. 3.3). We focus on a subset of these slope-limited channels, namely those (labelled studied channels in Fig. 3.3) that are subject to high melt rates (90% percentile > 10 m/yr, Sect. 3.4.5), as these potentially have a high likelihood of breaking through. To independently corroborate our channel product we map known locations of persistent polynyas (Alley et al., 2019) (Fig. 3.3) as they are known to be good indicators of buoyant upwelling from channelized ice shelf meltwater outflow (Mankoff et al., 2012). Apart from the easternmost polynya near Pine Island Ice Shelf, in an area of recent ice shelf retreat, all other polynyas are located at the outflow of detected channels.

Since channel incision and potential breakthrough is controlled by peak melt rates within channels, we extract and compare the localized peak melt rates within all studied channels from BURGEE, Adusumilli, and Davison (Sect. 3.4.6 and 3.4.7, Fig. A.6). This analysis indicates that BURGEE indeed reveals higher melting in channels (Fig. A.6), with altimetry-only peak melt rates underestimated substantially by up to 42-50% (Davison-Adusumilli), likely because the deep surface depressions resolved by REMA are not (fully) captured by CryoSat-2. To assess whether the underestimated melt in the altimetry-only studies is general across channels, or only at the deepest surface depressions, we extract mean melt rates along 10-km transects transverse to the channels (Methods). The mean melt rates across channels are on average underestimated by 11-22% (Davison-Adusumilli), showing that melting underestimation is present across channels, though more severe at the deepest surface depressions.

The underestimation of peak melt rates is consistent across all ice shelves and ice
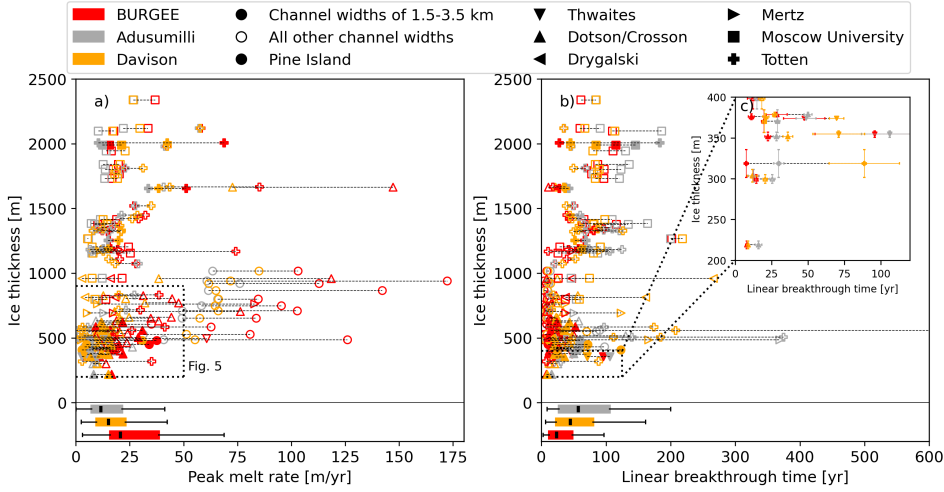
Figure 3.4: **Channel peak melt rates and breakthrough times**. **(a)** Channel peak melt rates compared to ice shelf thicknesses outside the channels. Dashed lines connect peak melt rates from the different products of the same channel. Filled markers indicate channels with a characteristic channel width of 1.5-3.5 km, which is comparable to the characteristic channel width (2.5 km) used to obtain normalized breakthrough times (Wearing et al., 2021). Unfilled markers represent all other channels (only narrower). **(b)** and **(c)** Linear channel breakthrough times compared to ice shelf thicknesses outside the channels. Dashed lines connect linear breakthrough times from the different products of the same channel. **(c)** is a zoom-in of **(b)** as marked by the dashed square **(c)**. The dashed square in **(a)** refers to the zoom-in shown in Fig. 3.5. For clarity purposes errorbars are only shown in panel **(c)**.

shelf thicknesses studied (Fig. 3.4). Since this underestimation has consequences for assumptions about ice shelf weakening, we assess the impact of increased peak melt rates in an idealized model using the normalized breakthrough times as an indicator of weakening. The normalized breakthrough time is defined as the time for a channel to breakthrough when secondary flow is considered divided by the linear breakthrough time, i.e., without considering secondary flow (Wearing et al., 2021) (Fig. 3.5). The normalized breakthrough time thus describes the breakthrough slow-down due to secondary flow. This relationship is derived from an idealized 2D cross-section of an ice shelf made for channels with a characteristic channel width of 2.5 km (Sect. 3.4.7).

The higher BURGEE peak melt rates yield shorter normalized breakthrough times across all ice shelves studied (Fig. 3.5) when compared to both altimetry-only studies (Adusumilli et al., 2020; Davison et al., 2023). This conclusion would not change for channels with a characteristic channel width not comparable in scale to the model study channel width (Wearing et al., 2021). Narrower (wider) channels have longer (shorter) normalized breakthrough times, but breakthrough time is still controlled by the peak melt rate (Wearing et al., 2021).
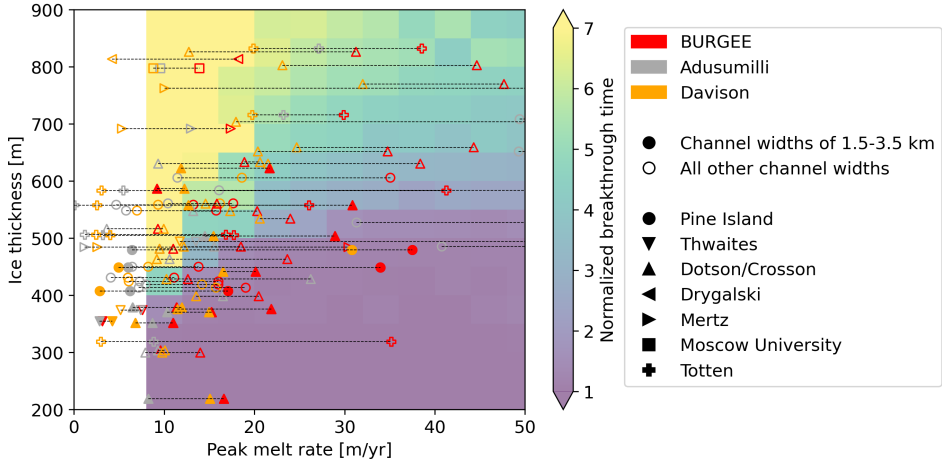
Figure 3.5: **Normalized breakthrough times**. Normalized breakthrough times, based on channel peak melt rates, compared to ice shelf thicknesses outside the channels and normalized breakthrough times obtained from Wearing et al. (2021). A normalized breakthrough time of 1 is when linear breakthrough and breakthrough with secondary flow are equal. The dashed square in Fig. 3.4 marks the zoom-in region used in this figure. As in Fig. 3.4 the dashed lines connect peak melt rates from the different products of the same channel. Filled markers indicate channels with a characteristic channel width of 1.5-3.5 km, which is comparable to the characteristic channel width (2.5 km) used to obtain normalized breakthrough times (Wearing et al., 2021). Unfilled markers represent all other channels (all narrower).

The magnitude of the implications of underestimating peak melt rates, and thus weakening, become clear on Pine Island and Dotson/Crosson ice shelves, where channels are comparable in scale to those considered in the modelling study (Wearing et al., 2021) (characteristic channel width of 1.5-3.5 km, ice thickness <1000 m, and peak melt rate from 8-50 m/yr). Within the most downstream part of the main melt channel on Dotson (lime box, Fig. 3.6a), BURGEE peak melt rate (16.6±0.8 m/yr) and breakthrough time with secondary flow (7±1 yr) are comparable to Davison (15.1±0.6 m/yr and 7±1 yr) but twice as high/fast as Adusumilli (8.2±1.0 m/yr and 13±2 yr). Moving upstream on the Dotson main melt channel (orange box, Fig. 3.6a), where thicker ice is present, BURGEE peak melt rate (28.9±2.3 m/yr) and breakthrough time with secondary flow (17±1 yr) are several times higher/faster than both Davison (15.5±0.3 m/yr and 94±3 yr) and Adusumilli (14.5±0.9 m/yr and 100±7 yr). Meanwhile, the BURGEE peak melt rate in the western shear zone on Pine Island (red box, Fig. 3.6b) is 17.1±2.2 m/yr, resulting in a breakthrough time with secondary flow of 25±3 yr. In comparison, Davison (2.8±0.7 m/yr) and Adusumilli (6.2±0.5 m/yr) peak melt rates are too low to even cause channel breakthrough.

These reductions in breakthrough times have significant consequences if the break-
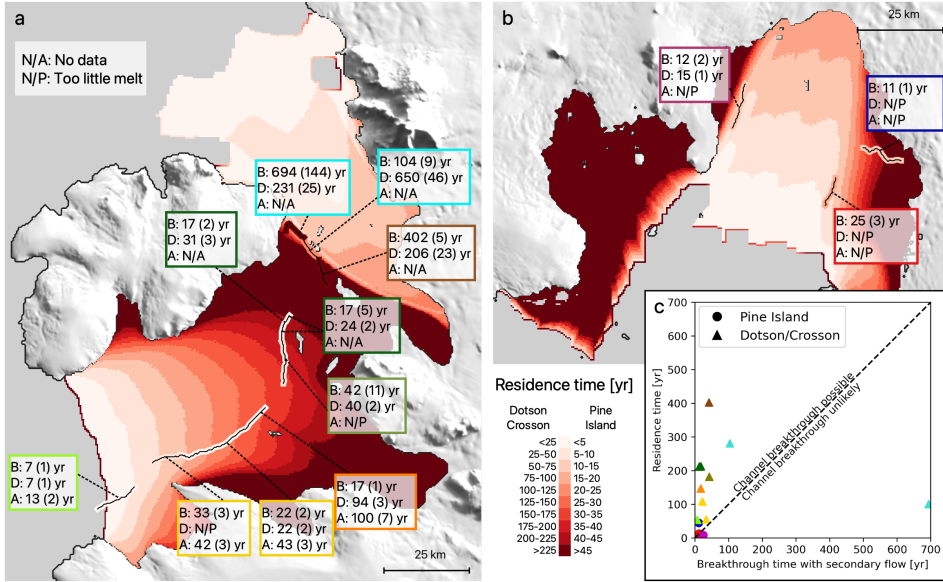
Figure 3.6: **Residence times and channel breakthrough times**. Ice shelf residence times of Dotson/Crosson **(a)** and Pine Island **(b)** ice shelves overlaid with studied channels with a characteristic channel width of 1.5-3.5 km and accompanied by channel breakthrough times where secondary flow is included (B: BURGEE/this study, D: Davison, A: Adusumilli). The colouring of the breakthrough time boxes corresponds to the markers in **(c)**. Standard deviations are given in the brackets (Sect. 3.4.9). N/P corresponds to peak melt rates <8 m/yr, where channel breakthrough is assumed to be unlikely (Wearing et al., 2021). The colouring of the channels corresponds to BURGEE breakthrough times with secondary flow. Panel **(c)** compares BURGEE breakthrough times with secondary flow to channel residence times with marker colouring corresponding to the boxes in **(a)** and **(b)**.

through time is shorter than the residence time, i.e. the time that it takes for the ice to advect to the ice shelf front. On Dotson/Crosson all channels, except one channel subsection at the shear zone between Crosson and Dotson (turquoise box, Fig. 3.6), have the potential to breakthrough within the residence time when comparing to BURGEE breakthrough times (Fig. 3.6, Sect. 3.4.6 and 3.4.7). In contrast, neither Adusumilli nor Davison exhibit melt rates high enough to cause a breakthrough in major sections of the Dotson main melt channel (yellow and olive boxes, Fig. 3.6). On other parts of the main channel (orange box, Fig. 3.6) their breakthrough times (94±3 yr and 100±7 yr) are much closer to the residence time (147 yr) than BURGEE (17±1 yr). They therefore underestimate the magnitude of channelized melting, and thereby also the potential weakening it may cause locally and for the whole ice shelf.

On Pine Island, where ice shelf surface velocities are amongst the highest in Antarctica and residence times thus amongst the shortest, basal channel breakthrough is possible

within the residence time for two channels and unlikely for a third. The two channels where breakthrough is possible are located in the eastern shear zone (BURGEE breakthrough time: 12±2 yr, residence time: 13 yr, purple box, Fig. 3.6) and west of the western shear zone (BURGEE breakthrough time: 11±1 yr, residence time: 45 yr, blue box, Fig. 3.6). However, irrespective of residence time, these channels would not breakthrough when considering the Adusumilli melt rates because the peak melt rate is too low(<8 m/yr). Using Davison melt rates, only the eastern channel (purple box, Fig. 3.6) has the potential to breakthrough. However, that would not be within the residence time for this channel. This underestimation of peak melt rates and thus channel breakthrough times makes ice shelves more susceptible to weakening than previously assumed with altimetry-only studies.

The only channel on Pine Island where channel breakthrough (25 ±3 yr based on BURGEE) does not occur within the residence time (8 yr) is located in the western shear zone of the ice shelf (red box, Fig. 3.6). Although breakthrough is unlikely, extensive damage has already caused calving and ice shelf retreat (Lhermitte et al., 2020) in this shear zone. On several other ice shelves, similar transverse fracturing has been observed in the vicinity of basal channels (i.e. Nansen, Moscow University, Totten; Dow et al., 2018). Monitoring such areas at high resolution is therefore crucial to understand the interplay between basal melt channels, damage, and their role in calving and ice shelf retreat, and highlights the importance of considering channel breakthrough times as indicator for future damage development.

3.3   Implications

The previous underestimate of peak melt rates in ice shelf basal channels, and the consequences for channel breakthrough times, lead to underestimation of ice shelf weakness. Even though we only explicitly discussed this for Dotson/Crosson and Pine Island ice shelves, this conclusion is valid for all ice shelves with underestimated peak melt rates. These findings, therefore, highlight the importance of properly resolving basal melt rates. While melt rates derived from altimetry-only observations are not fully capable of constraining channel melt patterns, they do have the advantage of a higher temporal resolution, as they are not constrained to cloud-free and sunlit conditions, which are needed for stereo imagery. There is, therefore, an opportunity to obtain high spatio- and temporal-resolution channel melt rates using a combination of BURGEE and altimetry through deep learning approaches, as has been done for surface melt (de Roda Husman et al., 2024), or other multi-sensor approaches (Winstrup et al., 2024).

Our findings further underscore the importance of including channelized melting at high resolution in ice sheet models due to the implications for ice shelf weakening, stability and buttressing. Here, we have used a simplified model representation of basal channel evolution, neglecting 3D ice dynamics, channel-width variability, elastic and brittle deformation, spatio-temporal evolution of melting and uncertainty related to ice-flow parameters, to consider the implications of increased peak melt rates. However, to fully assess the implications of focused melting in basal channels and project future change,

these processes should be included in ice sheet models. Crucially, basal channels must be simulated at high resolution (≤500 m) to capture channel evolution and interplay with fractures. Furthermore, there is a need to accurately simulate ocean dynamics and melting within basal channels in a coupled ocean model. Ongoing efforts aim to include these processes in simulations with realistic (Lambert et al., 2023) and idealized geometries (Sergienko, 2013; Drews, 2015; Bassis and Ma, 2015; Humbert et al., 2022). However, integrating them into ice-sheet-wide projections is essential to fully evaluate the impact of ocean melting on ice sheet stability and the implications for global sea level rise (van Westen and Dijkstra, 2021).

3.4 Methods

3.4.1 Basal melt rates Using REMA and Google Earth Engine (BURGEE)

To calculate the basal melt rates we make use of BURGEE v2, an updated version of Basal melt rates Using REMA and Google Earth Engine (BURGEE v1, Zinck et al., 2023). The basal melting is calculated in a Lagrangian reference frame following a mass conservation approach and under the assumption that the ice shelf is floating in hydrostatic balance. The basal melt rate ($\dot{M}_b$) is thus obtained through

$$\dot{M}_b = \dot{M}_s - \left(\frac{\mathrm{D}h}{\mathrm{D}t} - \frac{\mathrm{D}h_f}{\mathrm{D}t} + (h - h_f)(\nabla \cdot \boldsymbol{u})\right)\frac{\rho_w}{\rho_w - \rho_i}, \tag{3.1}$$

where $\dot{M}_s$ is the mean annual surface mass balance over the study period obtained from the regional climate model RACMO 2.3p3 (van Wessem et al., 2018), $\frac{\mathrm{D}}{\mathrm{D}t}$ denotes the Lagrangian change, h is the surface elevation, h_f is the firn air content obtained from the firn densification model IMAU-FDM v1.2A (Veldhuijsen et al., 2023), ρ_w is the density of water (assumed to be 1025 kg· m^{-3}), ρ_i is the density of ice (assumed to be 917 kg· m^{-3}), and $\nabla \cdot \boldsymbol{u}$ is the divergence of the velocity field. For the latter we use the MEaSUREs ITS_LIVE data product (Gardner et al., 2022) and total-variation regularization (Chartrand, 2017) to calculate the divergence. A full description of BURGEE v1, including a sensitivity experiment of the Lagrangian displacement, can be found in Zinck et al. (2023). In the following sections we describe the updates made to achieve BURGEE v2 (Tab. A.1).

3.4.2 Co-registering REMA elevations

We use CryoSat-2 measurements (Level-1B SARin Baseline-E where available and Baseline-D otherwise) to co-register the REMA strips using a plane-fit approach. Before the co-registration takes place, both CryoSat-2 and REMA elevations are referenced to the EGM2008 geoid (Pavlis et al., 2012) and corrected for the mean dynamic topography (DTU15MDT), tides (CATS2008), and inverse barometer effect using the 6h NCEP/NCAR sea level pressure reanalysis data. In BURGEE v1, the REMA strips were corrected for tides on a 6-hourly basis, which was changed to the acquisition time of

the first stereo image used to generate the REMA strip in BURGEE v2. In the co-registration, a few adjustments have been made with respect to the CryoSat-2 coverage over the individual REMA strips, needed to perform the co-registration. In BURGEE v1 the CryoSat-2 points furthest apart from each other in the latitudinal and longitudinal directions were required to be separated by at least 60 km and 10 km, respectively, to ensure sufficient representation. This criterion has been changed to a CryoSat-2 coverage in both the latitudinal and longitudinal directions of at least 75% of the distance of the REMA strip in both of those directions. This implies that even small REMA strips, that otherwise would have been filtered out, will be taken into consideration, while making sure that we have a sufficient CryoSat-2 coverage. Furthermore, the minimum number of CryoSat-2 points needed was previously set to 80, this has now been changed to at least 80 points or at least a 5% CryoSat-2 coverage at a 500 m resolution. As for the latitudinal and longitudinal coverage criterion, this change implies that smaller, otherwise good quality, REMA strips are not filtered out.

3.4.3   Lagrangian elevation change and basal melt rate

To obtain the Lagrangian elevation change, all REMA strips are displaced to their 2017-01-01 location based on the ITS_LIVE velocities (Gardner et al., 2022) and are further displaced using feature tracking with respect to the median elevation map based on all velocity-displaced REMA strips from 2015-07-01 to 2017-07-01. In BURGEE v1, the reference elevation map used was generated from the last year of data only, however, not all ice shelves in this study have equally good coverage in the last study year (Fig. A.7), so this ensures better coverage and therefore more features which can be used in the feature tracking. Furthermore, we now apply the feature tracking to all strips individually instead of first generating yearly median elevation maps. Yearly median elevation maps are generated after the final displacement, and only years covering at least 25% of an ice shelf are used, since years with limited coverage reduces the quality of the basal melt rate estimation. Finally, for the same reason, the basal melt rate in BURGEE v2 is only calculated in pixels with at least three years of elevation coverage (see Fig. A.7 for a full overview of areas covered per year). Remote sensing-derived basal melt rates should always be used with care in the vicinity of the grounding line, since hydrostatic equilibrium assumptions can interfere with the inferred melting signal. Ice shelves experiencing grounding line retreat are therefore more sensitive to interferences in the melting signal in the vicinity of the grounding line, with its spatial implications determined by ice flow.

3.4.4   Model description

We use the idealized modelling results from Wearing et al. (2021) to assess the time to breakthrough (as a metric for weakening). This idealized modelling considers a confined 2D vertical plane, of 50 km width, aligned perpendicular to a basal channel. The full-Stokes numerical ice-flow model ELMER/Ice (Gagliardini et al., 2013) is used to simulate the evolution of a basal channel. The domain is assumed to be advected in the primary flow direction of the ice shelf, without along-flow extension. An idealized basal melt

rate is imposed at the centre of the domain using a Gaussian function with peak melt rate (M_p) and a characteristic width (x_m, equal to one standard deviation). Surface accumulation is spatially uniform and set so that the total accumulation matches the total basal melting. The ice rheology is specified by Glen's Flow Law, with a uniform rate factor appropriate for ice at $-10°$C, ($A = 3.5 \times 10^{-25}$ s^{-1} Pa^{-3}) (Cuffey and Paterson, 2010) and flow-law exponent $n = 3$. Each simulation is initiated with an ice shelf of uniform thickness (H), and is run for one characteristic time. If the channel incises completely the simulation stops. The results used in this assessment use a characteristic width of $x_m = 2500$ m.

This idealized modelling neglects some more complex processes, such as the effect of longitudinal and transverse strain (determined by local and ice-shelf scale stresses) on ice shelf thickness and effective viscosity, elastic deformation, brittle deformation, fine-scale and spatial-temporal evolution of ice-ocean interaction (melting and freeze-on).

3.4.5   Extracting channels

Under the assumption that the ice shelf surface topography reflects that of the ice shelf base, we use the surface topography to systematically identify the location of basal channels. Using the REMA DEM mosaic (Howat et al., 2019) at 32 m resolution, bicubic down-sampled onto a 250 m resolution grid, we calculate the accumulated flow in each grid cell. The accumulated flow is the number of upstream cells calculated using a watershed delineation approach (pysheds). We define basal channels as grid cells with an upstream inflow of at least 1000 cells. This threshold was found through trial-and-error, with the goal of removing as many "visually false" channels as possible, while keeping "visually true" channels. A comparison with other thresholds is shown in Fig. A.8, which shows that the end product of "studied channels" is little influenced by this threshold. To exclude smaller sub-branches, channels shorter than 2.5 km are filtered out, together with those shorter than 10 km if the maximum accumulated flow of the channel is less than 5000 upstream pixels. We refer to the resulting channels as "all channels" (Fig. 3.3) and compare them to existing channel products (Fig. A.9). We, furthermore, perform a sensitivity test by varying these thresholds within reasonable bounds, which shows only little dependence on their actual value (Fig. A.10). To exclude crevasses, which otherwise fulfilled the aforementioned criteria, we filter out channels where the maximum slope (considering both along and across flow) is greater than $15°$. These channels that are filtered out correspond to either channels in highly fractured areas or actual fractures (Fig. A.5). While recent studies do show elevated melt rates within crevasses (Schmidt et al., 2023; Wåhlin et al., 2024), it is difficult to fully separate the elevation change signal into components associated with fracturing and basal melting. The remaining channels are referred to as "slope-corrected channels" (Fig. 3.3). Finally, in this study we only consider a subset of the slope-corrected channels, namely those channels with at least 50% BURGEE coverage and with a 90% percentile melt rate higher than 10 m/yr, which we consider indicative of channels with active melting. These channels are referred to as "studied channels" (Fig. 3.3).

3.4.6   Peak channel melt rates and breakthrough analysis

To analyze melting within the channels, we extract 10 km transects perpendicular to the channels at 1 km intervals along their length (Fig. A.11). Since channel breakthrough times depend on ice thickness, we divide the channels into segments (sub-channels) based on their ice thickness. This segmentation ensures that representative values for peak melt rates, mean melt rates, and ice thickness are used in the breakthrough analysis. The segmentation is based on the difference in along-channel thickness (ΔH). The thickness bin size (H_{bin}) is calculated as

$$H_{bin} = \frac{\Delta H}{\lceil \Delta H/100 \rceil},$$

where $\lceil \ \rceil$ is the ceiling function. This method ensures bin intervals are a maximum of 100 m ice thickness (see example in Fig. A.11). Sub-channels comprising less than three transects are excluded from the analysis.

For each sub-channel, we extract median transects of BedMachineV3 ice thickness (Morlighem, 2022), REMA surface elevations (Howat et al., 2019), and basal melt rates from BURGEE, Adusumilli, and Davison, respectively. Channel widths are derived for each transect by averaging the transect's surface elevation profile and its mirrored counterpart, fitting an inverted Gaussian curve at the channel center, and using the first two maxima to define channel boundaries (Fig. A.11). The standard deviation of the Gaussian fit is defined as the characteristic channel width. Sub-channels with standard deviations exceeding 10 km are excluded as outliers, as they imply basal channels wider than 10 km. These wide channels are typically located in regions where REMA surface depressions are poorly represented in BedMachineV3 due to its coarser resolution (500 m) or because of differences in the BedMachineV3 input data, as it is not solely based on the REMA mosaic. Additionally, sub-channels with more than 20% grounded ice within their median transects are excluded, as the assumption of hydrostatic equilibrium becomes invalid near the grounding line.

To determine representative values for ice thickness and melt rates, we define the ice shelf thickness outside the channel as the 80% percentile of the median ice thicknesses across all transects (Fig. A.11). Peak melt rates are calculated as the 90% percentile of transect melt rates within ± 2 km of the channel center (i.e. the channel positions as derived from the accumulated flow analysis, Fig. A.11). Mean channel melt rates are defined as the average of the respective transect median melt rates.

3.4.7   Evaluation of peak melt rates and breakthrough times

We compare the ice thicknesses outside the channels with the channel peak melt rates of all three products (BURGEE, Adusmilli, and Davison, Fig. 3.4), as these are the main factors influencing channel breakthrough times. We zoom in on the thinner ice sections (200-900 m), where channel breakthrough is possible, even when secondary flow is taken into consideration (Fig. 3.5). For these thinner ice sections, normalized breakthrough times of channels with a channel width of 1.5-3.5 km are compared between all three

products (solid makers in Fig. 3.4 and 3.5). The remaining channels are all narrower than 1.5 km and are not comparable in size to the channel-assumptions made in the modelling study to obtain the normalized breakthrough times (Wearing et al., 2021) (2.5 km). We, furthermore, calculate linear breakthrough times (t_{lb}) using

$$t_{lb} = H_c/\dot{M}_p, \tag{3.2}$$

where H_c is the ice thickness within the channel and $\dot{M}_p$ is the peak melt rate. The linear breakthrough times are of special interest for ice shelves thinner than 400 m where secondary flow barely provides any breakthrough-delay (Wearing et al., 2021) (Fig. 3.4c).

Using the linear breakthrough times and normalized breakthrough times from Wearing et al. (2021), breakthrough times with secondary flow are calculated. Normalized breakthrough times are only available for channels thinner than 1000 m and peak melt rates in the range from 8-50 m/yr. Ice shelf residence times (the time that it takes for the ice to advect to the ice shelf front) are obtained from Wearing et al. (2021) and are based on ice velocities in comparison to the distance from the ice shelf front. The residence times are compared to the breakthrough times with secondary flow to establish whether a channel is likely to breakthrough before it reaches the ice shelf front.

Finally, we compare the impact of the different time periods the reference maps are based on in the different melt products' Lagrangian frameworks (Fig. A.2 and A.12) on the peak melt rates and thus also on assumptions about channel breakthrough (Fig. A.13 and A.14).

3.4.8 Wavelength analysis

To determine whether all basal melt products analyzed in this study capture the full range of possible melting wavelengths within their signal, including the smaller scales associated with channelized melting, we perform a Fourier analysis of the basal melt maps. Specifically, we assess the Lomb-Scargle spectra (Lomb, 1976; Scargle, 1982) of the melt maps, a statistical tool designed to detect periodic signals in unevenly spaced data, which accommodates gaps in the maps. For consistency, we restrict the analysis to areas covered by all products.

The melt maps from the three products (BURGEE, Adusumilli, and Davison) are treated as individual 2D arrays per ice shelf. The analysis is conducted on data rows (or columns) of the individual 2D arrays in segments of 10 km, with an overlap of 5 km between consecutive segments. To minimize spectral leakage, a Hamming window is applied to each segment before performing the Lomb-Scargle analysis. We only include segments with at least 90% data coverage and calculate their power spectra using the following sampling intervals (t) and frequencies (f):

$$t = \{t_0, t_1, t_2, \ldots, t_n\}, \quad \text{where} \quad t_i = i \cdot r \quad \text{and} \quad t_n < L, \quad t_{n+1} \geq L, \tag{3.3}$$

and

$$f = \{f_0, f_1, f_2, \ldots, f_n\}, \quad \text{where} \quad f_i = i \cdot \frac{1}{L}, \quad \text{and} \quad f_n < \frac{0.5}{r}, \quad f_{n+1} \geq \frac{0.5}{r}, \tag{3.4}$$

where i is the index, r is the posting of the product (thus either 50 m, 500 m, or 1000 m), and L is the segment length (10 km).

The choice of whether to analyze rows or columns is based on the predominant direction of ice flow and thus the rough "direction" of melting and channels. For Thwaites, Dotson/Crosson, and Drygalsky ice shelves, we analyze the power spectra of all columns to ensure that the melting/channels are roughly perpendicular to the analyzed segments. For all other ice shelves, we analyze the power spectra of all rows.

Finally, the power spectra are averaged per product and across all ice shelves, including the BURGEE product at both 50 m and 500 m spatial resolutions, as shown in Fig. A.4.

3.4.9   Uncertainty estimation

To estimate the uncertainty of the peak melt rates we calculate the standard deviation of melt rates between the 85 and 95 percentiles of all channel transects within a given channel. The uncertainty of the channel ice thickness is calculated by taking the standard deviation of the minimum channel thickness across all channel transects within a channel. The uncertainty estimations of linear and secondary flow breakthrough times are obtained through error propagation, in which we assume that the normalized breakthrough times are not associated with any errors as they are the result of an idealized model set up designed to represent a generic channel. Uncertainties in the residence time are associated with errors in the velocity product used and the calving front position (which may change with iceberg calving events). For ice shelves, the uncertainties are relatively low (approx. <1% of flow speed) and we, therefore, consider them to be negligible.

Code and data availability

The BURGEE code (V1 and V2) is publicly available at `https://github.com/aszin ck/BURGEE` (Zinck, 2023). The derived channel product and BURGEE basal melt rates are publicly available (`https://doi.org/10.4121/4e2ba9a9-7b1b-4837-b52d-0 36f8c876e67`, Zinck et al., 2024a). REMA strips and mosaics are available from the Polar Geosptaital Center (`https://www.pgc.umn.edu/data/rema/`), CryoSat-2 data is available from the European Space Agency (`https://earth.esa.int/eogateway/ documents/20142/37627/CryoSat-Baseline-D-Product-Handbook.pdf`), and MEaSUREs ITS_LIVE velocities and BedMachine V3 are both available from NASA National Snow and Ice Data Center (`https://doi.org/10.5067/6II6VW8LLWJ7` and `https://nsidc.org/data/NSIDC-0756/versions/3`).
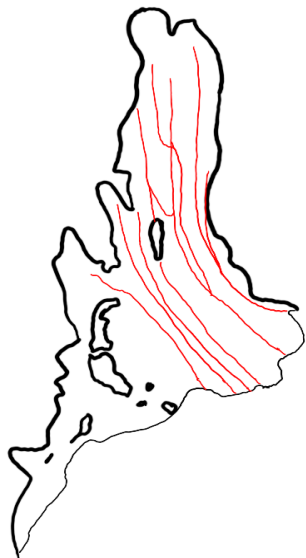
Appendix A

Supplementary to Ch. 3

- **Suppl**. **Fig**. **1** Basal melt rates.
- **Suppl**. **Fig**. **2** Pine Island Ice Shelf comparison.
- **Suppl**. **Fig**. **3** CryoSat-2 point-of-closest-approach and REMA coverage.
- **Suppl**. **Fig**. **4** Wavelength analysis.
- **Suppl**. **Fig**. **5** Damage.
- **Suppl**. **Fig**. **6** Mean and peak channel melt rates.
- **Suppl**. **Fig**. **7** Yearly coverage.
- **Suppl**. **Fig**. **8** Accumulated flow comparison.
- **Suppl**. **Fig**. **9** Channel comparison.
- **Suppl**. **Fig**. **10** Channel criteria sensitivity.
- **Suppl**. **Fig**. **11** Channel transects and Gaussian fitting.
- **Suppl**. **Fig**. **12** Lagrangian reference frames.
- **Suppl**. **Fig**. **13** 2015 reference year peak melt rates.
- **Suppl**. **Fig**. **14** 2015 reference year breakthrough times.
- **Suppl**. **Tab**. **1** Updates made to BURGEE v2.

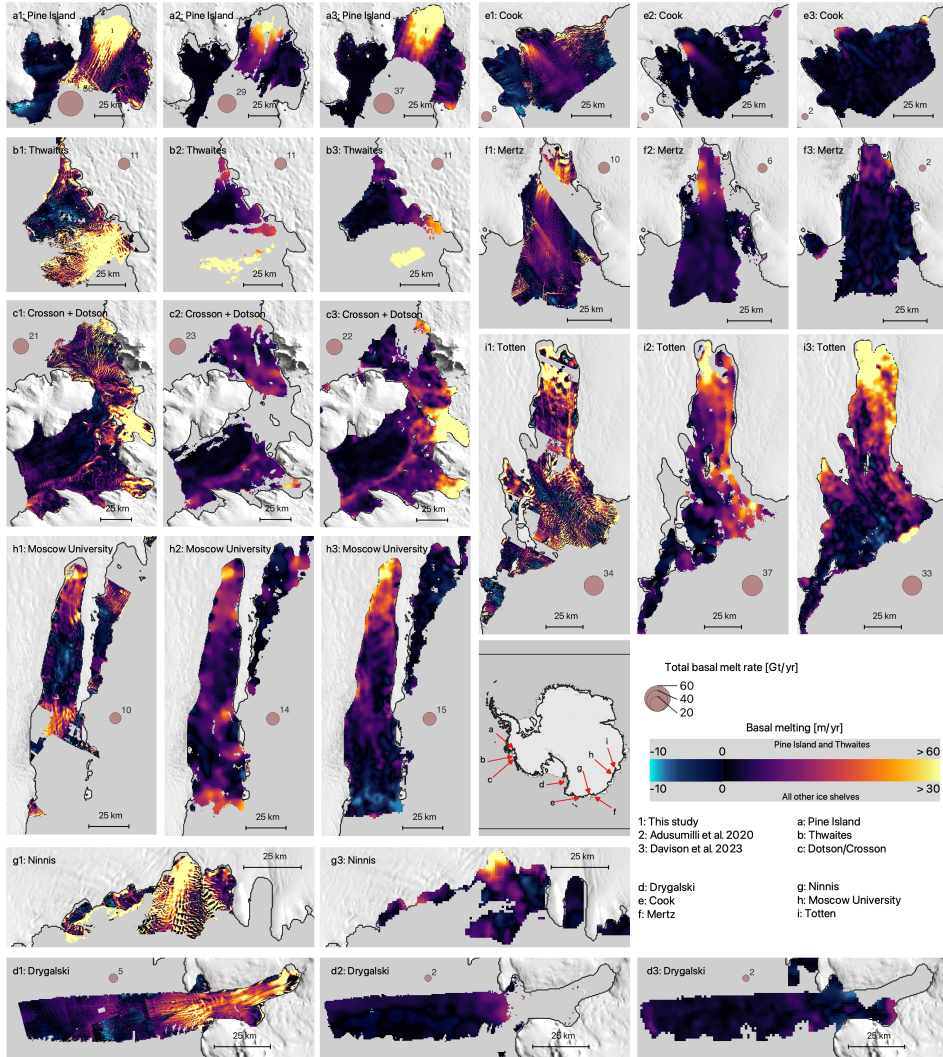Figure A.1: **Basal melt rates**. Basal melt rates from this study are marked with 1, from Adusumilli with 2, and from Davison with 3. The Ninnis ice shelf **(g)** is not covered by Adusumilli. The black line denotes the BedMachine V3 grounding line (Morlighem, 2022). The circles denote total ice-shelf wide basal melt rate in Gt/yr, only considering areas covered by both BURGEE, Adusumilli, and Davison.
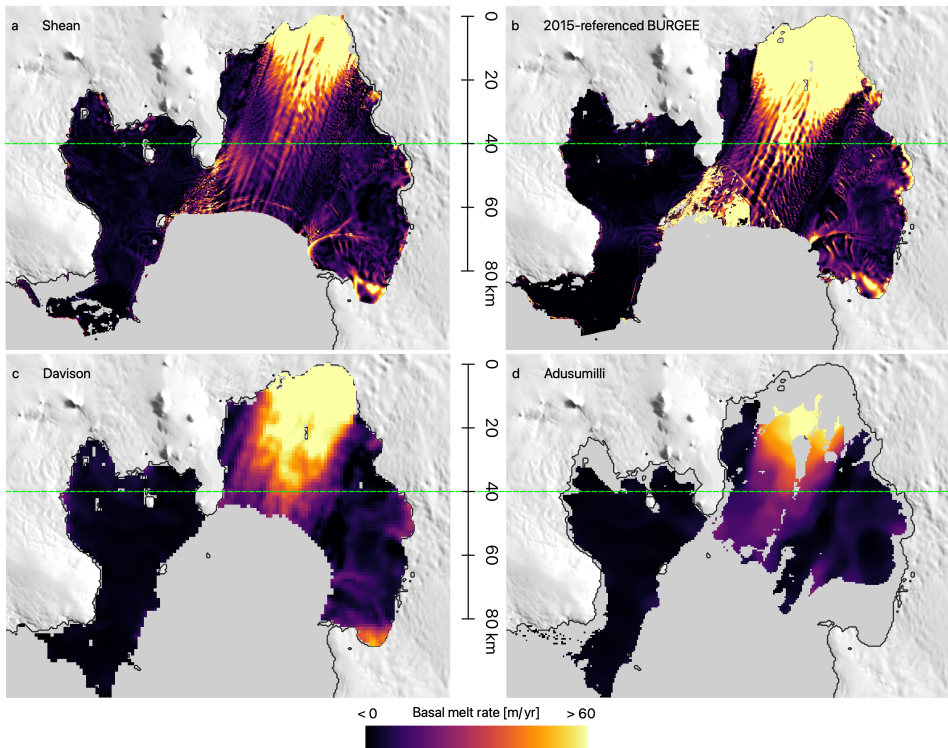
Figure A.2: **Pine Island Ice Shelf comparison**. Basal melt rates from **(a)** Shean et al. (2019), **(b)** BURGEE referenced to 2015, **(c)** Davison, and **(d)** Adusumilli. The Shean (Shean et al., 2019) melt rates are based on elevation changes from a combination of stereo imagery and altimetry, like BURGEE, but the approach of the lagrangian framework differs slightly from the other three. The Shean et al. (2019) melt rates are calculated on a 2-yearly basis, Lagrangianly displaced to the later of the two years, in the period from 2008-2015. The 2-yearly melt maps are eventually averaged and **(a)** is a result of that. In both Davison, Adusumilli and BURGEE, the elevations from all years considered are displaced to one specific date, and Lagrangian elevation changes and basal melt rates are calculated using these displaced elevations. Davison and Adusumilli both make use of 2015 as "reference year" for the displacement, whereas BURGEE uses 2017 (the last year of interest). This different approach between Shean et al. (2019) on one hand, and BURGEE, Adusumilli and Davison on the other hand, is what is leading to the difference in the extent of the area of high melt rates (reaching around 40 km, green line, in BURGEE, Adusumilli, and Davison, but only ∼30 km for Shean et al. (2019)). For the comparison here, we have displaced the final melt map of BURGEE "back" to 2015 using the ITS_LIVE velocities (Fig. A.12).
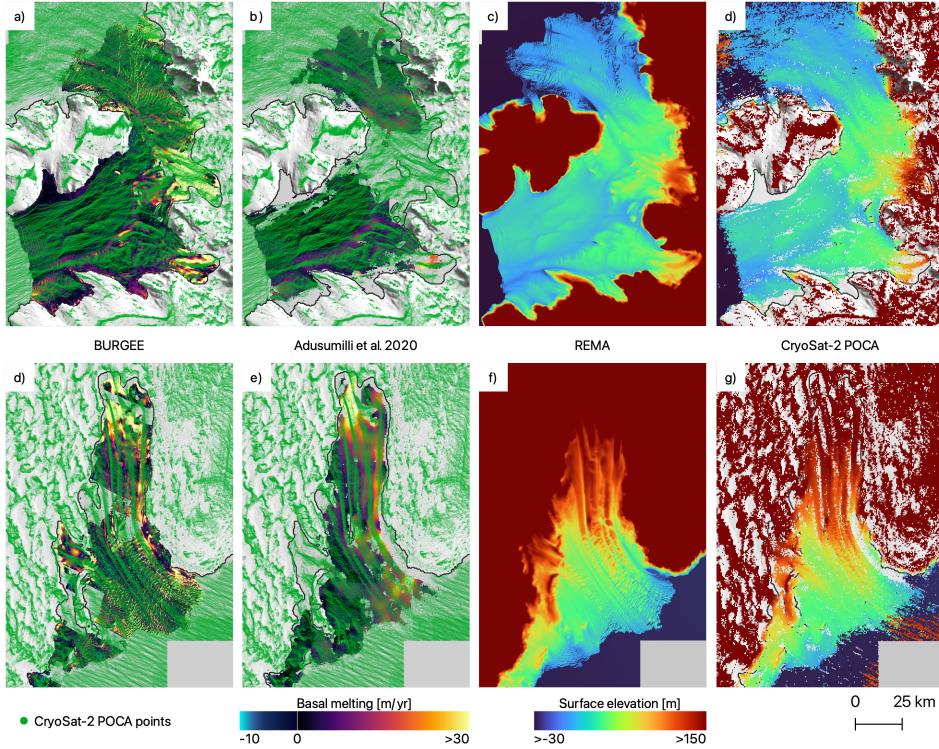
Figure A.3: **CryoSat-2 point-of-closest-approach and REMA coverage**. **(a)** and **(d)** Dotson and Totten ice shelves, respectively, with BURGEE melt rates and CryoSat-2 points. **(b)** and **(e)** Dotson and Totten ice shelves, respectively, with Adusumilli melt rates and CryoSat-2 points. **(c)** and **(f)** REMA mosaic surface elevation of Dotson and Totten, respectively. **(d)** and **(g)** CryoSat-2 point-of-closest-approach elevations of Dotson and Totten, respectively.
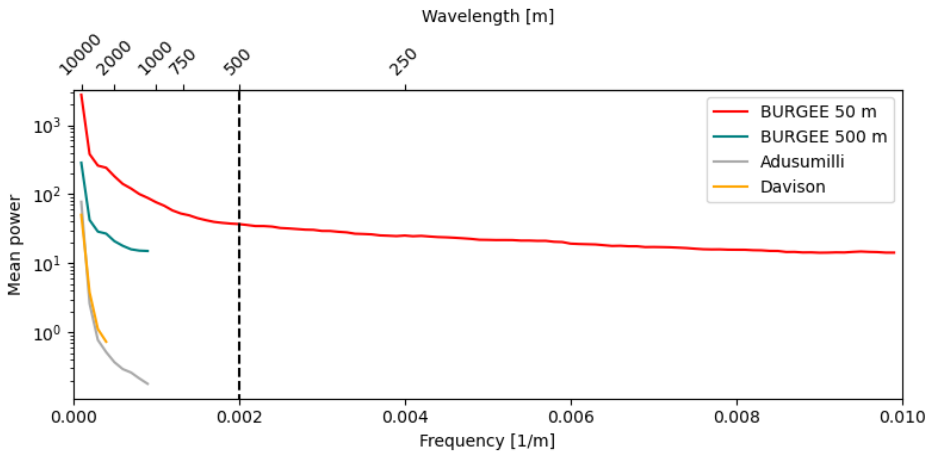
Figure A.4: **Wavelength analysis**. Average Lomb-Scargle power spectra across all common ice shelf areas of BURGEE (50 m and 500 m posting), Adusumilli, and Davison. The dashed vertical line indicates the approximate frequency (bottom) and wavelength (top) at which BURGEE (50 m) reaches its noise level (approximately constant power level for increasing frequencies). This indicates that BURGEE uniquely captures the full range of wavelengths and frequencies at which (channelized) melting occurs within the signal. Both Adusumilli and Davison unexplored melting frequencies within their signal as their power spectra do not reach a constant noise level. The transition from signal to noise in the BURGEE power spectrum indicates the smallest wavelengths at which melting occurs within the signal. This transition is located at a wavelength of 500 m and is an indicator of the wavelength that models must resolve to be able to capture channelized melting as observed by BURGEE (and/or the consequences thereof).
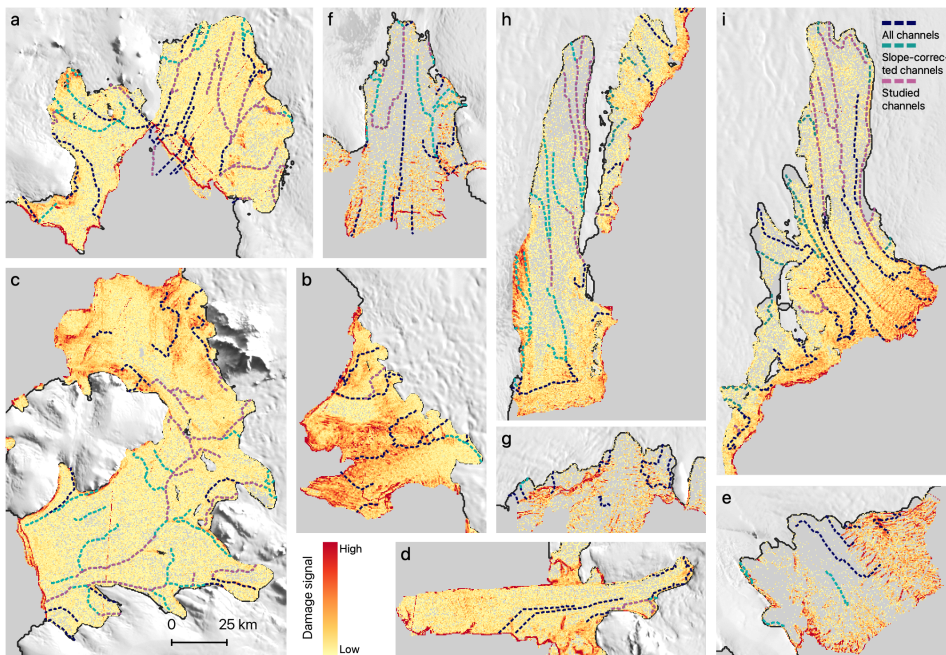
Figure A.5: **Damage**. Ice shelf average damage map from 2015-2018 (Izeboud et al., 2024) overlaid with detected channels. On-shelf areas in gray correspond to areas with either no or very low damage signal.
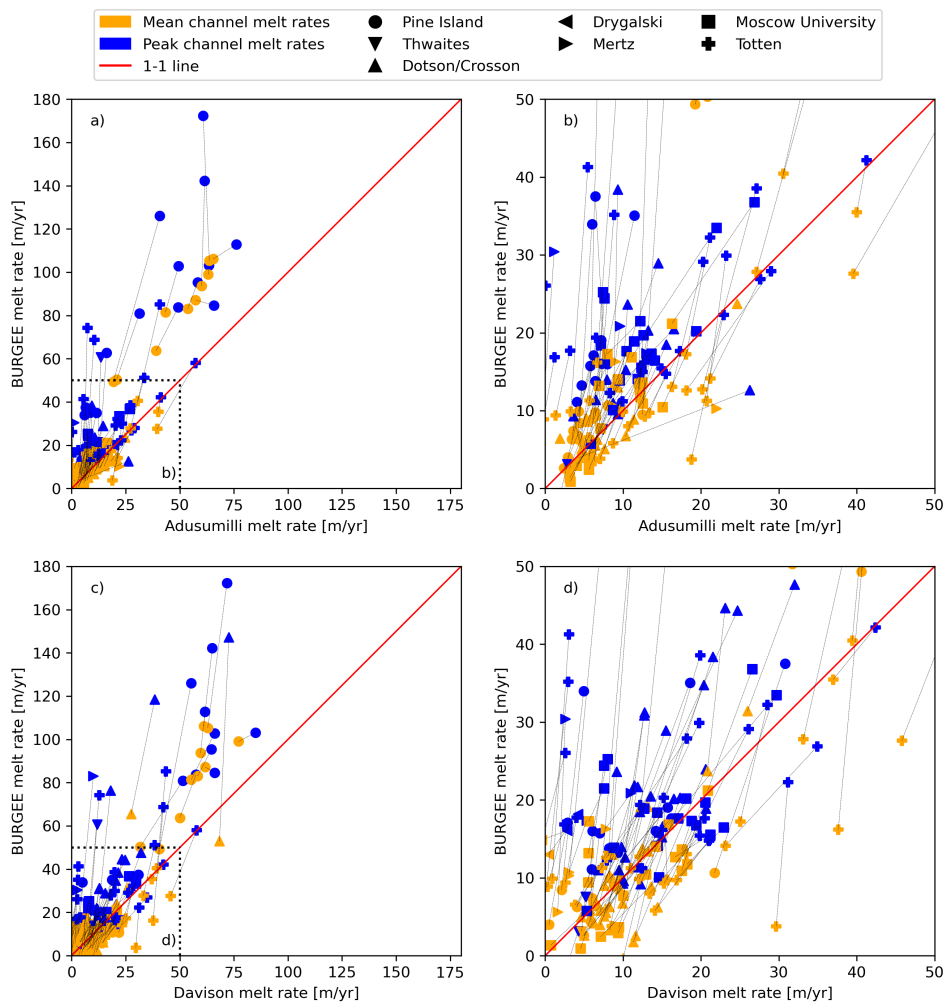
Figure A.6: **Mean and peak channel melt rates**. Mean and peak channel melt rates comparing BURGEE to Adusumilli (**(a)** and zoom-in in **(b)**) and Davison (**(c)** and zoom-in in **(d)**).
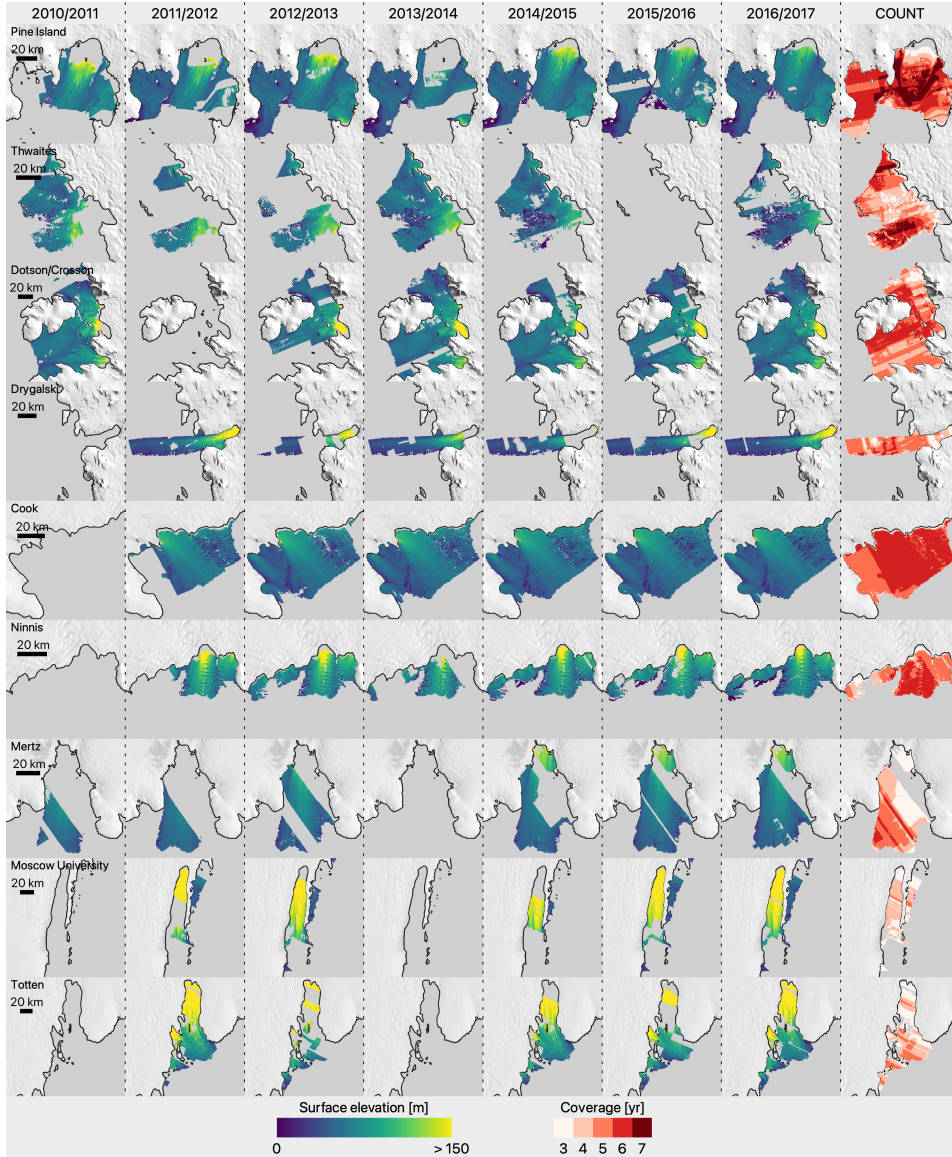
Figure A.7: **Yearly coverage**. Yearly elevation coverage per ice shelf, with the total years covered in the leftmost column (COUNT). All elevation, and thus also the COUNT maps, are Lagrangianly displaced to their end location.
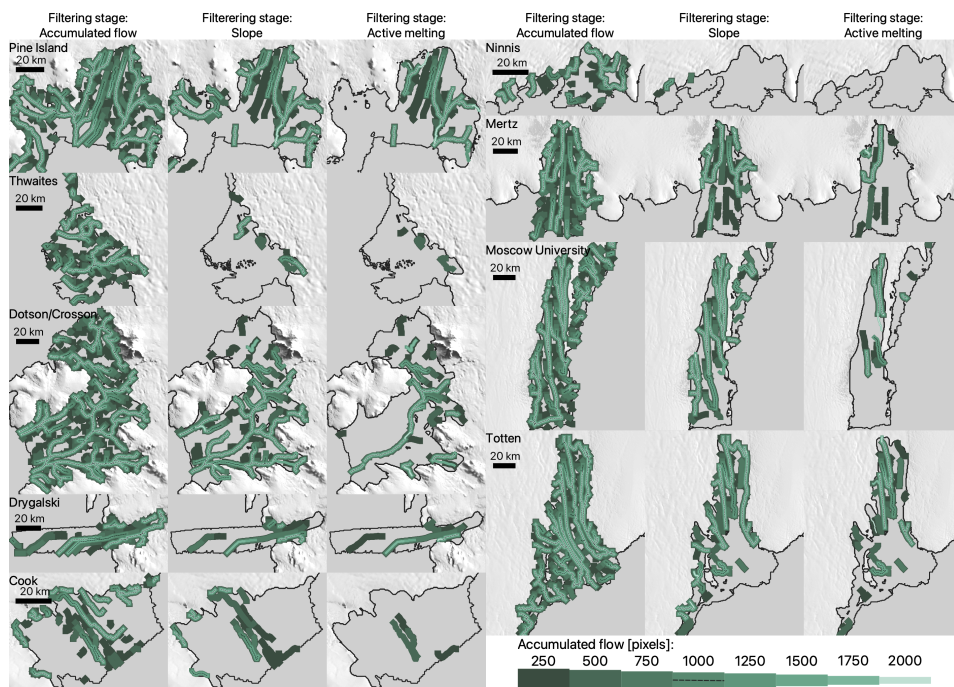
Figure A.8: **Accumulated flow comparison**. Comparison of channel detection using different accumulated flow thresholds in the watershed delineation approach. Here we show the channels at three different stages: Accumulated flow, Slope, and Active melting. The first stage (Accumulated flow) is the channels right after applying the initial accumulated flow threshold. The second stage (Slope) shows the before-mentioned channels after going through both the length and slope criteria as described in the Methods. Finally, the last stage (Active melting) shows the before-mentioned channels after being filtered based on BURGEE coverage and melt rate as described in the Methods. This shows that there is a relatively good agreement on the final channels (Active melting) regardless of the initial accumulated flow threshold, and that the chosen threshold of 1000 appears to be a good compromise of a threshold which works reasonable well regardless of ice shelf.

A
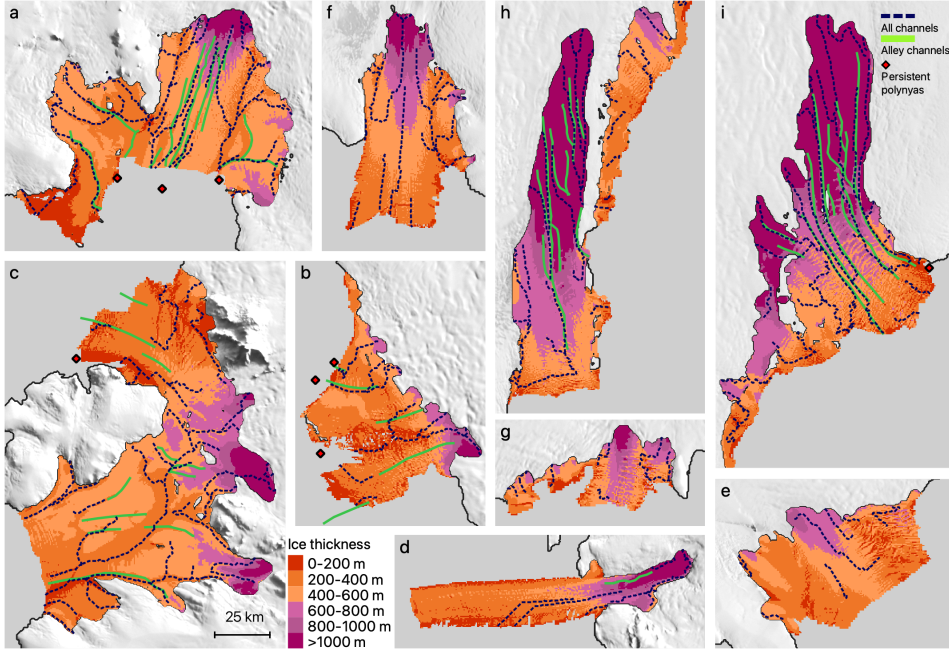
Figure A.9: **Channel comparison**. A comparison of the channels derived in this study ("All channels") with manually derived channels ("Alley channels") from MODIS optical imagery (Alley et al., 2016). The optical product is based on older and coarser resolution data than our REMA-based channels, which implies that a perfect match between the two is not expected. Channels may have migrated between the two products or, as on Thwaites Western Tongue, ice shelves may have experienced structural damage making channel detection challenging. Furthermore, smaller/narrower channels may have remained unseen by MODIS, which could explain the general higher density of channels per ice shelf in our product. Although, that does not explain why the main melt channel on the Dotson Ice Shelf was not detected from the MODIS imagery. However, there is a very good agreement between the two channel products on especially Moscow University and Totten ice shelves, which are both characterized by very well-pronounced channels in both elevation data and optical imagery. Finally, some channels on Pine Island Ice Shelf have remained unseen in our product due to the chosen accumulated flow thresholds.
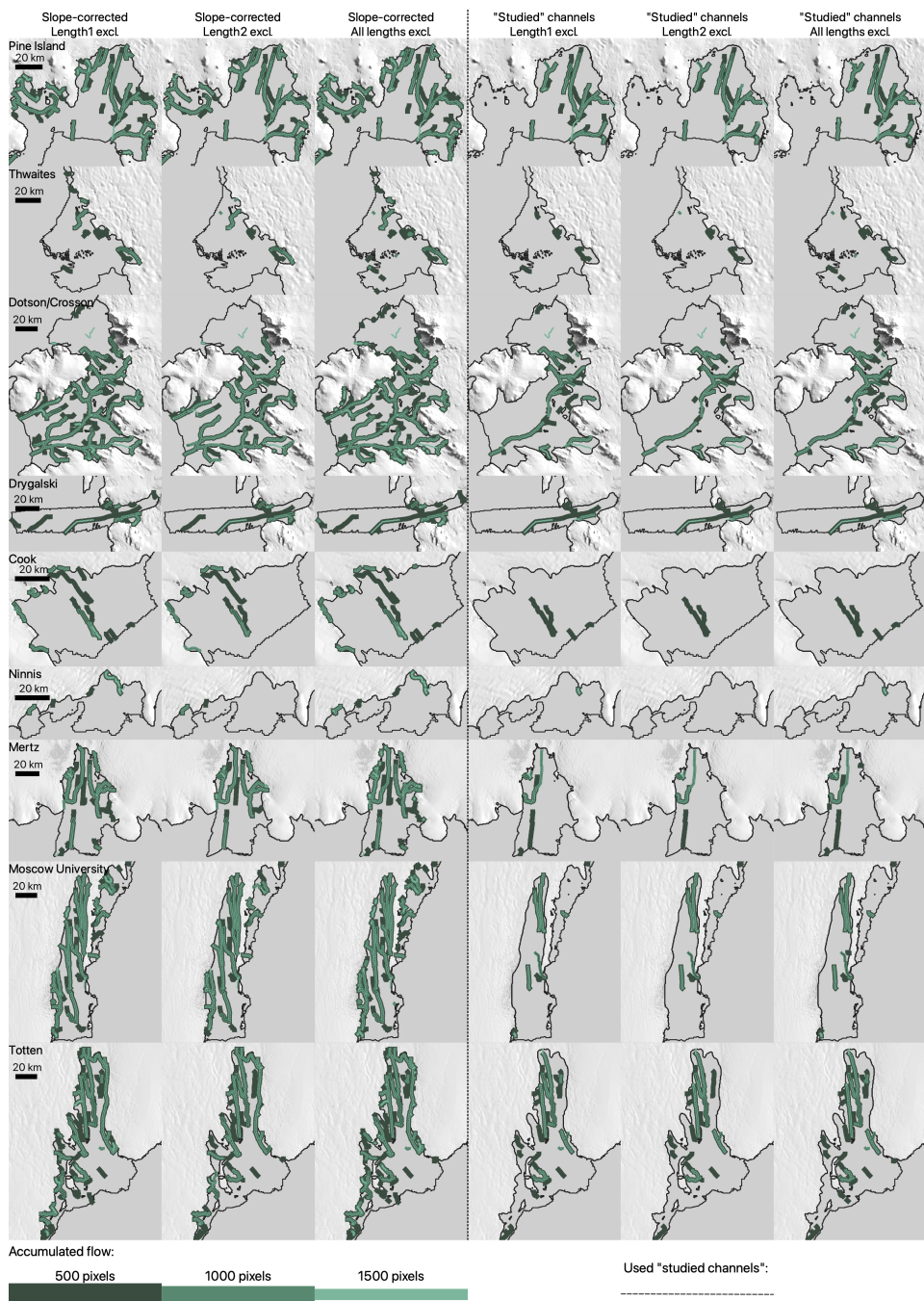
Figure A.10: **Channel criteria sensitivity**. *Caption on next page.*

A

Comparison of channel detection when excluding the different length criteria as described in the Methods. Three different cases are tested for three different cases of accumulated flow thresholds (500, 1000, and 1500). The first of the three cases is referred to as "Length1 excl." which implies that the criteria to remove all channels shorter than 10 km and with a maximum accumulated flow of less than 5000 pixels has been excluded. The second case is referred to as "Length2 excl." which implies that the criteria to remove all channels shorter than 2.5 km has been excluded. Finally, the last case "All lengths excl." implies that both of the two before-mentioned criteria are excluded. The impact of excluding one or both of these criteria is analysed at the stage after the slope-correction (Slope-corrected, the three columns left of the vertical dashed line) and at the stage after removing channels with too little BURGEE coverage or to little BURGEE melt ("Studied" channels, the three columns right of the vertical dashed line). From this sensitivity study it can be seen that these criteria (by excluding some of them) only have little impact on the final channels. As reference, the channels used in this study are marked by the black dashed line.
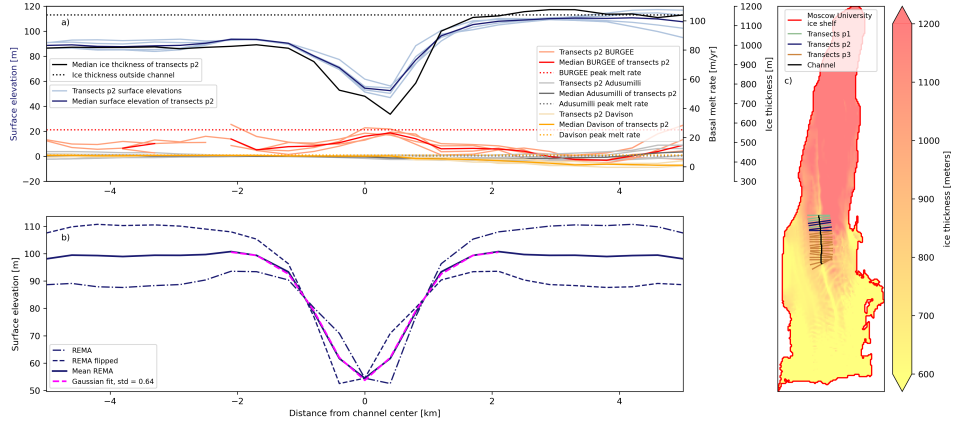
Figure A.ll: **Channel transects and Gaussian fitting**. **(a)** Ice thickness, surface elevation and basal melt rates of transects p2 as shown in **(c)** The peak melt rates are the 90 percentiles of all the transect p2 melt rates within ±2 km of the channel center. The mean melt rate is the mean of the median melt rate profile. The ice thickness outside of the channel is defined as the 80 percentile of the median ice thickness profile. **(b)** Example of Gaussian fitting of the transect p2 parts of the channel shown in **(c)** using the mean elevation profile of the surface elevation and its' flipped version. The channel width is defined as one standard deviation. **(c)** Example of a channel, its' transects and transact division based on ice thicknesses on Moscow University ice shelf with BedMachineV3 ice thicknesses below. The channel thickness difference of this channel is between 200-300 m, and then channel transects are therefore grouped into three different groups. Group pl: channels with a channel ice thickness in between H_{max} and $H_{max} - \frac{H_{max}-H_{min}}{3}$, where H_{max} is the maximum channel thickness and H_{min} is the minimum channel thickness. Group p2: channels with a channel ice thickness in between $H_{max} - \frac{H_{max}-H_{min}}{3}$ and $H_{max} - \frac{H_{max}-H_{min}}{2}$. Group p3: channels with a channel ice thickness in between $H_{max} - \frac{H_{max}-H_{min}}{2}$ and H_{min}.
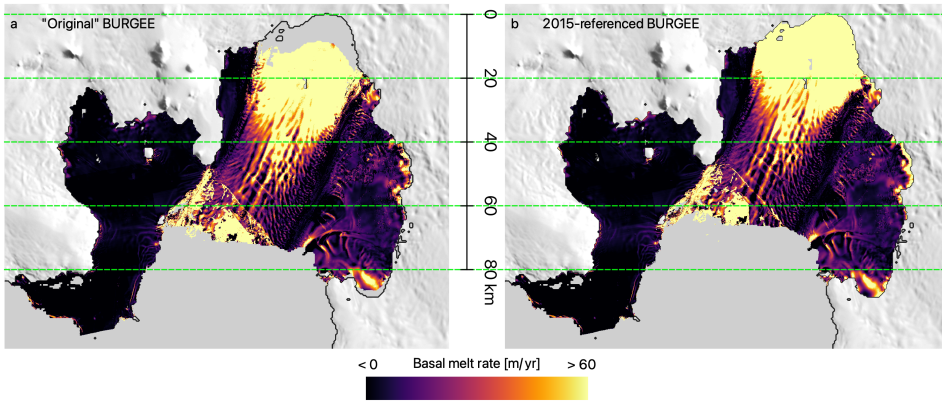
Figure A.12: **Lagrangian reference frames**. Comparison of the **(a)** "original" BURGEE melt rates, which are based on Lagrangianly displaced elevations with respect to 2017, and the **(b)** "original" melt rates displaced "back" to 2015 using the ITS_LIVE velocities. This 2015-referenced BURGEE melt map is thus a displaced version of the BURGEE melt maps, and are displaced to the same year as to which both Adusumilli and Davison are Lagrangianly referenced to. The difference between the two melt maps is largest in fastest flowing areas, which can be seen here in the center part of Pine Island, where the area of extended melting is moved ~5-10 km upstream. For the peak melt extraction we use the original BURGEE melt rate maps, and the implication of doing so is further outlined in Fig. A.13 and A.14.
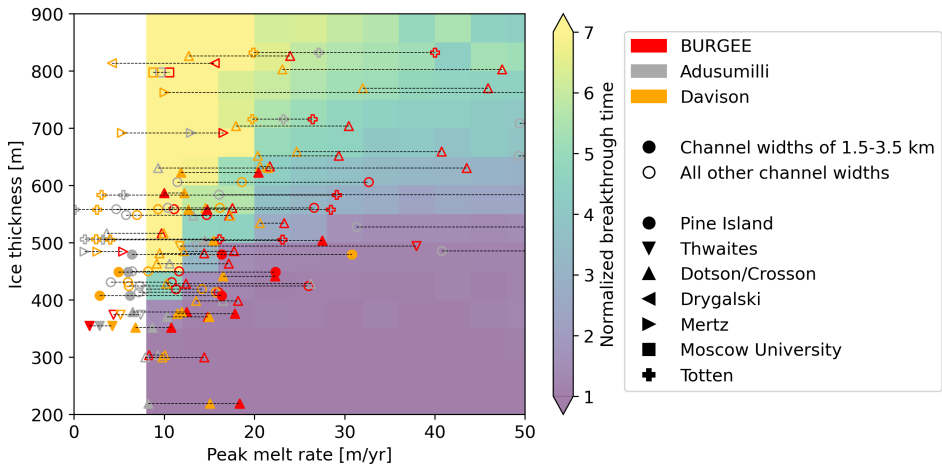
Figure A.13: **2015 reference year peak melt rates**. Derived peak melt rates with BURGEE melt maps displaced to 2015 (the same year as the Lagrangian displacement of Davison and Adusumilli). This figure shows that even when all products are referenced to the same year, the peak melt rates remain underestimated altimetry-only products. The peak melt rates are underestimated by up to 42% for Davison and 50% for Adusumilli with respect to the original BURGEE melt maps which are referenced to 2017. In this case, where we have displaced the BURGEE melt maps to 2015, the altimetry-only products are underestimated by up to 43% and 53% for Davison and Adusumilli, respectively. This implies, that even though these products have slightly different Lagrangian reference frames, the impact on the peak melt rates can be considered to be negligible for the peak melt rates.

A

Figure A.14: **2015 reference year breakthrough times**. BURGEE breakthrough times based on the 2015-referenced BURGEE melt rates. Comparing to the original BURGEE melt rate breakthrough times (Fig. 3.6c), it becomes clear that mainly the brown channel is impacted. This brown channel is located in the fastest flowing area between Dotson and Crosson (Fig. 3.6a), which explains the greater impact.

Table A.1: Updates made to BURGEE v2.

Component	BURGEE v1	BURGEE v2
REMA tides	6-hourly basis	Using sourceImage1 time-stamp
CryoSat-2 latitudinal and longitudinal criteria	CryoSat-2 points furthest apart from each other in the latitudinal and longitudinal directions are required to be separated by at least 60 km and 10 km	CryoSat-2 coverage in both the latitudinal and longitudinal directions of at least 75% of the distance of the REMA strip in both directions
CryoSat-2 coverage criteria	Minimum 80 CryoSat-2 points per REMA strip	Minimum 80 CryoSat-2 points per REMA strip or a percental coverage of at least 5%
Reference image for feature tracking	Median of the DEMs from the last year	Median of the 2015-07-01 – 2017-07-01 DEMs
Lagrangian displacement	Of the yearly median elevation maps	Strip-per-strip basis
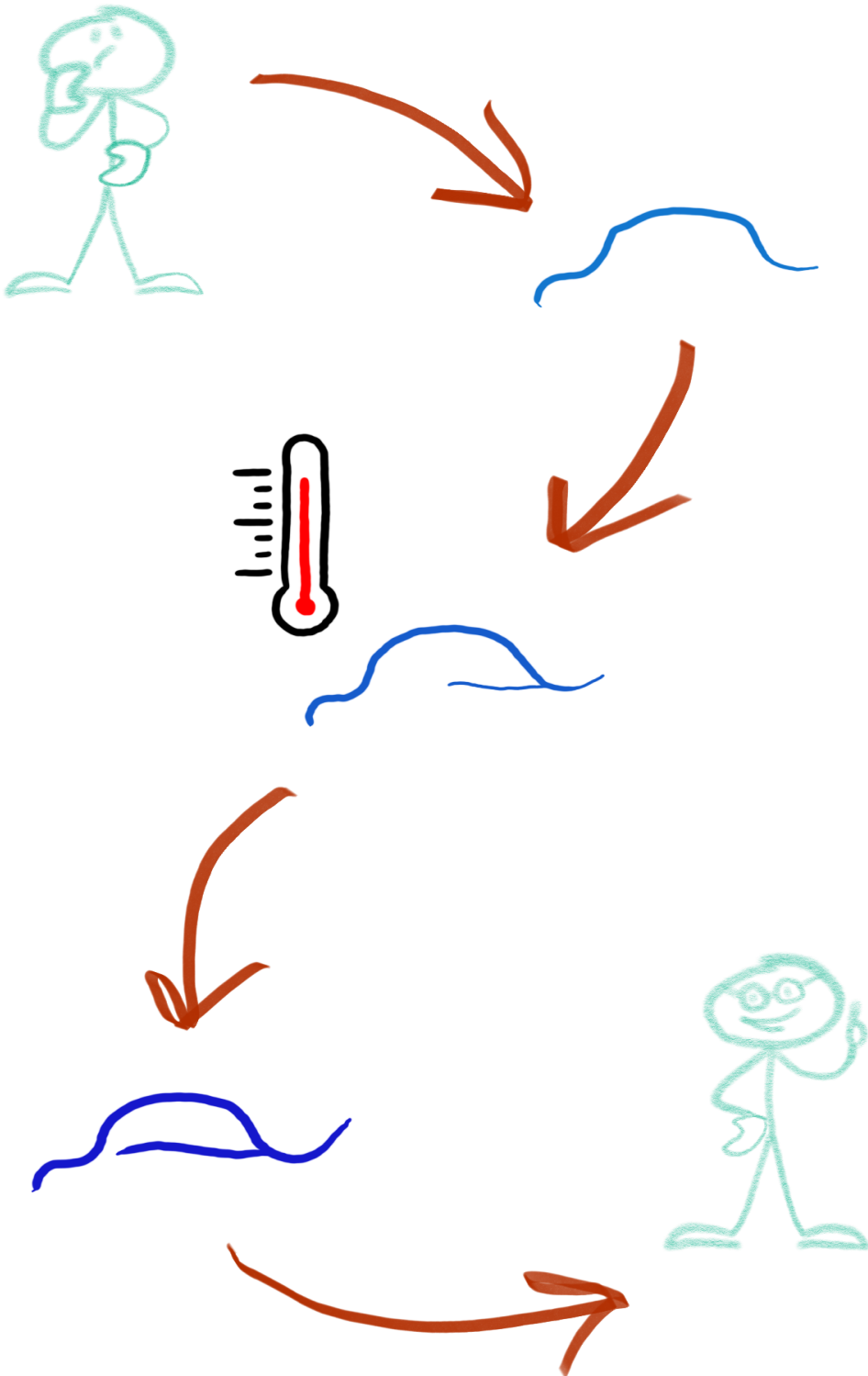
Chapter 4

Ocean-Induced Weakening of George VI Ice Shelf

Channelized basal melting is a critical process influencing ice shelf weakening, as basal channels create zones of thinning and vulnerability that can potentially lead to ice shelf destabilization. In this study, we reveal and examine the rapid development of a channel within the George VI Ice Shelf's extensive channelized network, characterized by a 23 m surface lowering over a nine-year period. We study changes in ice flow, ocean circulation and heat potential as possible drivers behind the channel, under the hypotheses that it is either a fracture, a basal melt channel, or a combination of the two. Our findings show that the onset of this channel coincides with significant changes in ocean forcing, including increased ocean temperatures and salinity, that occurred during the 2015 El Niño Southern Oscillation event. Modelling of basal melting further suggests that channel re-routing has taken place over this nine-year period, with the channel serving as a basal melt channel in the latest years. We further observe subtle shifts in ice flow indicative of fracturing. Our findings thus indicate that this channel likely contributes to the weakening of an already thin ice shelf through a combination of basal melting and fracturing. These findings offer insight into how similar potentially destabilizing processes could unfold on other Antarctic ice shelves. Monitoring the evolution of this channel and its impact on ice shelf integrity will be critical for understanding the mechanisms of ice shelf retreat, especially on heavily channelized ice shelves.

4.1 Introduction

The future evolution of the Antarctic Ice Sheet and its potential sea level contribution in a changing climate is highly uncertain (IPCC, 2023), largely due to the unknown response of ice shelves (Pattyn and Morlighem, 2020; Bamber et al., 2022; van de Wal et al., 2022). Ice shelves play a critical role in buttressing the ice sheet (Fürst et al., 2016) and their weakening or eventual collapse can accelerate ice flow across the grounding line, which in turn contributes to sea level rise (Pattyn and Morlighem, 2020; van de Wal et al., 2022). It is therefore crucial to understand the processes that lead to ice shelf weakening to better constrain uncertainties in sea level rise projections.

Basal melting is one such process known to weaken ice shelves (Pritchard et al., 2012; Silvano et al., 2016) and has been linked to the collapse of Wordie Ice Shelf (Doemgaard et al., 2024). Basal melting is often driven by the intrusion of Circumpolar Deep Water (CDW), a relatively warm water mass located at depth beyond the continental shelf (Silvano et al., 2016). In some regions of Antarctica, the continental shelf's bathymetry allows CDW to flow over it, enabling this warm water to reach ice shelf cavities (referred to as warm cavity ice shelves). This phenomenon occurs particularly in the Amundsen and Bellingshausen Seas - where the Wordie Ice Shelf was located - which experience some of the highest basal melt rates on the continent (Rignot et al., 2013; Davison et al., 2023). Although basal melting is most pronounced near the grounding zone due to the pressure-dependent freezing point of seawater (Silvano et al., 2016), the resulting meltwater plume usually travels from the grounding zone towards the ice shelf front, thereby carving basal channels in the ice (Alley et al., 2022). These channels, which are more prominent in warm cavity ice shelves (Alley et al., 2016), represent potential zones of weakness due to their reduced thickness and elevated melt rates relative to their surroundings (Alley et al., 2022).

Basal channels are dynamic features that do not necessarily remain in a steady state. They can experience changes in melt intensity, fracturing, and re-routing. In warm cavity ice shelves, the magnitude of melting within channels and across the entire ice shelf is primarily influenced by the volume and temperature of CDW entering the ice shelf cavity (Dutrieux et al., 2014). These oceanic conditions can, in turn, be affected by larger climatic phenomena such as the El Niño Southern Oscillation (ENSO, Huguenin et al., 2024). Increased availability or higher temperatures of CDW can thus lead to enhanced thinning through basal melting (Paolo et al., 2018).

Basal channels can also be associated with transverse fracturing, a phenomenon observed on several ice shelves, including Pine Island, Nansen, Moscow University, and Totten (Dow et al., 2018; Alley et al., 2024). These fractures, driven by extensional stresses within the ice (Dow et al., 2018), have triggered major calving events on Nansen and Pine Island ice shelves (Dow et al., 2018; Alley et al., 2024, 2022). Although extensional stresses are considered a primary driver, variations in meltwater availability within channels may also contribute to fracture formation (Alley et al., 2022). In addition to transverse fracturing, longitudinal fractures within basal channels have been documented (Vaughan et al., 2012; Dutrieux et al., 2013), potentially leading to full-
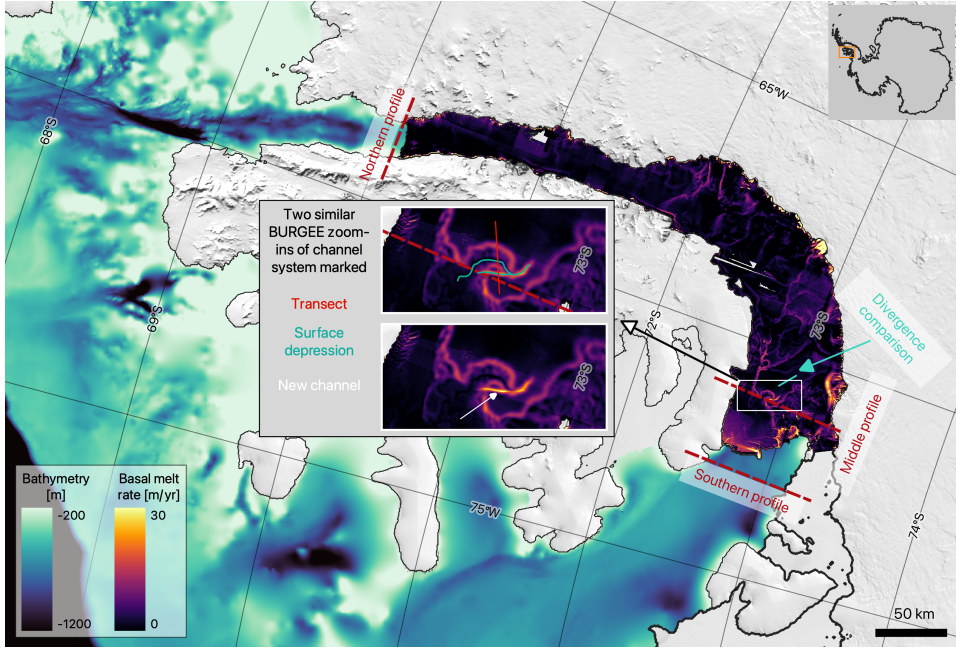
Figure 4.1: A map of the study area (George VI Ice Shelf) with BURGEE basal melt rates and bathymetry from BedMachineV3 (Morlighem et al., 2020; Morlighem, 2022). The grounding line and ice shelf extent are from BedMachineV3 (Morlighem et al., 2020; Morlighem, 2022). The three profiles marked (Southern, Middle, and Northern) refer to the profiles in Figure 4.6. The transect marked as "Divergence comparison" refers to the transect used for assessing the root-mean-square error of the divergence in Fig. 4.5. Two similar zoom-ins of the highly channelized area marked by the white square shows BURGEE melt rates both with the approximate location of the surface depression of the old and new channel in year 2016 in teal, the new channel pointed out by the white arrow, as well as the red transect used in Fig. 4.4 and 4.5.

thickness fractures and eventual ice shelf retreat (Alley et al., 2022).

The interactions between basal channels, fractures, and CDW-variations are highly complex, reflecting significant knowledge gaps in channel dynamics. Beyond changes in melt magnitude and fracturing, basal channels have been observed to migrate laterally or re-route entirely. Examples of such behavior include channels on the Getz (Chartrand and Howat, 2020) and Roi Baudouin (Drews et al., 2020) ice shelves, as well as other ice shelves in the Amundsen and Bellingshausen Sea sectors (Alley et al., 2024). Lateral channel migration, often in the direction favored by the Coriolis effect, has been linked to increased ocean heat availability (Alley et al., 2024). Similarly, the re-routing of a meltwater plume on Thwaites Ice Shelf has been observed to follow pre-existing fractures, underscoring the interplay between channel dynamics and ice shelf structure (Alley et al., 2024).

The importance of high-resolution basal channel melt rates on ice shelf weakening was emphasized using Basal melt rates Using REMA and Google Earth Engine (BURGEE, Zinck et al., 2024b). The high-resolution BURGEE melt data reveal a peculiar, and to our best knowledge so far unreported, channel on George VI Ice Shelf with high melt rates near extensive channelization (Fig. 4.1). The channel appears to intersect and alter other channels in the area, suggesting significant changes in the channel system during the BURGEE period (2010–2022). Given the channel's location in a heavily channelized area and its proximity to the southern ice shelf front which has been persistently retreating since 1947 (Smith et al., 2007), this channel poses a potential risk of further retreat.

In this study, we examine the potential drivers behind the formation and evolution of this newly observed channel on the George VI Ice Shelf (Fig. 4.1). Using high-resolution surface elevation and basal melt rate data, we assess temporal changes in channel morphology. Furthermore, we explore the roles of ice flow dynamics, ocean circulation, and ocean forcing as potential contributors to channel evolution. Finally, we employ a basal melt model with realistic ocean forcing and ice shelf geometries from two time periods to investigate the possibility of channel re-routing within the observed network. This multi-faceted approach aims to advance our understanding of the processes driving rapid channel formation.

4.2   Study area

Our study area focuses on the region surrounding the newly identified channel on the George VI Ice Shelf located near the southern ice shelf front, as well as the two entrances to its ice shelf cavity where CDW flows in (Fig. 4.1). The analysis spans the BURGEE period from 2010 to 2022.

George VI Ice Shelf is particularly vulnerable due to its already thin state and ongoing thinning (Smith et al., 2007; Davison et al., 2023). The ice shelf experiences significant melting both from its surface (de Roda Husman et al., 2024; van Wessem et al., 2023) and its base (Davison et al., 2023), making it susceptible to structural weakening. Adding to this vulnerability, studies have shown that parts of the firn layer of the ice shelf are saturated to levels that could facilitate hydrofracturing, while other areas are approaching similar thresholds with only minor increases in temperature (van Wessem et al., 2023). This dual weakening mechanism highlights the sensitivity of George VI Ice Shelf to changes in climatic conditions.

The bathymetry of the region further amplifies this vulnerability. Troughs in the continental shelf guide CDW into the cavity beneath the ice shelf (Fig. 4.1, Hyogo et al., 2024). Once inside the cavity, the CDW drives some of the highest basal melt rates observed in the Antarctic Peninsula (Davison et al., 2023).

4.3   Data and Methods

In the following subsections, we describe the data and methods used to i) generate high-resolution surface elevation and basal melt rates to analyze the temporal evolution of the channel (Sect. 4.3.1); ii) explore potential drivers behind the channel, utilizing both ice velocity observations (Sect. 4.3.2) and model simulations of ocean circulation and forcing (Sect. **??**); iii) model temporal changes in basal melt patterns near the channel driven by variations in ocean forcing and ice shelf geometry (Sect. 4.3.4).

4.3.1   Surface elevations and basal melt rates

To derive high-resolution surface elevation and basal melt rates of the George VI Ice Shelf, we use BURGEE as presented in Zinck et al. (2023) and updated in Zinck et al. (2024b). In summary, BURGEE utilizes CryoSat-2 SARin Baseline-E Level 1B radar altimeter data to co-register the 2-meter REMA digital surface model strips (Howat et al., 2022), producing high-resolution surface elevation maps. From these maps, surface elevation changes are calculated in a Lagrangian framework, from which basal melt rates are derived using information about surface mass balance, firn, and ice flow.

For this study, we use REMA strips from version s2s041 (Howat et al., 2022) instead of the older s2s030 (REMA v1) used in Zinck et al. (2023, 2024b). The latter is the only version available on the Google Earth Engine but covers only the years from 2010 to 2017, whereas the newest version is updated yearly with new data. Since George VI is frequently cloud-covered, we included these newer strips to enhance coverage. All strips were bicubically interpolated onto a 50-meter grid from their original 2-meter resolution to reduce storage requirements, both locally and on Google Earth Engine.

Surface elevations were derived by co-registering the REMA strips to CryoSat-2 radar altimetry measurements, following the method outlined in Zinck et al. (2023) with updates from Zinck et al. (2024b). First, both datasets were adjusted for dynamic and static corrections – accounting for tides, mean dynamic topography, the inverse barometer effect, and geoid referencing. Then, tilt and bias in the REMA strips were corrected by fitting a plane through the REMA/CryoSat-2 elevation residuals. Basal melt rates were calculated similarly to Zinck et al. (2024b), with a minor adjustment in the Lagrangian displacement related to the feature tracking. In previous work (Zinck et al., 2024b), strips were referenced to a median elevation map covering the period 2015-07-01 to 2017-07-01. Here, for the George VI Ice Shelf, we extended this median elevation map period to 2018-07-01 for improved ice shelf coverage, resulting in better quality of the Lagrangian displacement. To derive the basal melt rate through the traditional mass conservation approach we used both information about firn air content from the IMAU-FDM v1.2A (Veldhuijsen et al., 2023) and surface velocities from MEaSURE ITS_LIVE (Gardner et al., 2022) to calculate the ice flux divergence as described in Zinck et al. (2023). For the surface mass balance, however, we used a new 2 km resolution down-scaled version of the regional climate model RACMO (Noël et al., 2023). The final surface elevation and basal melt maps were produced on a 50-meter grid.

4.3.2   Ice velocities and divergences across the channel

To investigate ice speed and divergence across the new channel (Fig. 4.1), and track their temporal evolution as possible indicators of fracturing, we use monthly ice velocities from ENVEO (provided by the European Space Agency's Antarctic Ice Sheet Climate Change Initiative project). Based on Sentinel-1 synthetic aperture radar imagery, these velocities offer higher spatial and temporal resolution, along with greater coverage, compared to velocity products based on optical imagery feature tracking. We examine a ~15 km transect crossing both the persistent channel system and the new channel (Fig. 4.1). Yearly ice speeds are calculated by taking the median of the monthly speeds, with measurements extracted every ~250 meters along the transect.

To obtain the divergence along the transect, we first calculate the yearly median x- and y-components of the monthly velocity fields, then extract the values along the transect in the same manner as for ice speed. The divergence is computed by summing the velocity gradients in the x- and y-directions for the yearly velocity fields along the transect. To estimate the noise in the divergence data we calculate the root-mean-square error of the yearly divergences along a transect (Divergence comparison, Fig. 4.1) where rifting and thus changes in the divergence field are not expected to occur.

4.3.3   Ocean heat and circulation

To investigate changes in ocean heat content and circulation during the study period, we use output from the Amundsen-Bellingshausen Seas regional configuration of the Massachusetts Institute of Technology general circulation model (MITgcm), which has been validated against observational oceanographic data (Hyogo et al., 2024; Park et al., 2024). This model configuration, originally developed by Nakayama et al. (2018), features a horizontal grid spacing of 2–4 km and 70 vertical layers. The vertical resolution varies, with layer thicknesses ranging from 10 meters near the surface to 450 meters in the deepest regions ($\sim$ -6000 m), and between 70–90 meters at depths of -500 to -1000 meters. The model uses constant ice shelf geometry and ocean bathymetry from BEDMAP-2 (Fretwell et al., 2013) and has a monthly temporal resolution. We use the model for two purposes; to analyze changes in i) ocean circulation and ii) ocean heat. First, to explore potential changes in ocean circulation near the channel which could explain its development, we obtain mean annual velocities by averaging the model's monthly velocities over the years 2010 and 2020, at two different depth levels: -325 m and -391 m. The first is just below the ice base in the thinner areas and the latter is at a depth below the ice base in most areas near the channel. Secondly, to investigate changes in ocean heat we examine monthly changes in temperature and salinity for all years between 2010 and 2020 to determine if shifts in ocean heat potential can explain the channel's development. Temperature and salinity profiles are extracted from three cross-sections: the northern and southern entrances to the ice shelf cavity, and near the channel (Fig. 4.1). Even though the new channel is located near the southern entrance, CDW entering through the northern entrance might contribute to the meltwater plume within the channel system, due to the sub-shelf circulation (Hyogo et al., 2024). Anomalies in temperature and salinity are calculated by subtracting the 2010 to 2020

time-averaged values at each depth level. Furthermore, we compute the depth-averaged monthly temperature and salinity for the water mass below -300 m, where CDW is found in the George VI cavity (Jenkins and Jacobs, 2008; Holland et al., 2010).

4.3.4 Modelling of basal melt rates

We use the two-dimensional basal melt model LADDIE (Lambert et al., 2023) to simulate basal melt rates with greater spatial detail (compared to the MITgcm output) for George VI Ice Shelf in two scenarios: i) from the beginning of the BURGEE period before July 2016 (BEFORE experiment), and ii) from the end of the BURGEE period after July 2016 (AFTER experiment). The goal is to investigate potential changes in plume direction and melt patterns near the channel, using two different ice shelf geometries and ocean forcings, resembling the two different time periods, while keeping other model parameters constant. Below, we describe how these ice shelf geometries and ocean forcings are derived, and how the model is tuned to match observed basal melt rates.

Ice shelf geometry

The ice shelf geometries for the BEFORE and AFTER scenarios are generated using a combination of BedMachineV3 (Morlighem et al., 2020; Morlighem, 2022) data and co-registered REMA strips (Sect. 4.3.1). BedMachineV3 provides the bathymetry, ice shelf mask, and the ratio between surface elevation and ice shelf thickness, which we use to transform REMA-derived surface elevations into ice thickness and draft. As LADDIE only considers areas where its mask is set to be ice shelf, we do not consider areas outside of the ice shelf in terms of the generation of the BEFORE and AFTER geometries.

We use BURGEE to create two separate high-resolution surface elevation maps of the ice shelf (see Fig. 4.2 for a visual representation of the workflow). This implies horizontally aligning REMA strips from different time periods, followed by a vertical alignment with respect to BedMachineV3. For the surface elevation for the BEFORE geometry, all strips up to 2016-07-01 are firstly displaced to their location as of 2013-01-01 using MEaSURES ITS_LIVE velocities (Gardner et al., 2022). Secondly, these strips are further displaced using feature tracking relative to the median elevation map between 2012-07-01 and 2015-07-01 to ensure alignment across strips. The displaced strips provide surface elevation estimates. To derive ice thickness, we use BedMachineV3's surface-elevation-to-thickness ratio. Since the surface elevation used in BedMachineV3 has not been subject to the exact same dynamic and static corrections as used here, the finally co-registered strips are co-registered to the BedMachineV3 surface, by fitting a plane through the residuals. The median of the resulting strips is taken and interpolated onto the 500 m BedMachineV3 grid, from which ice shelf thickness is obtained by using the BedMachineV3 surface elevation to thickness ratio. All negative ice shelf thicknesses and ice shelf thicknesses > 2000 m are replaced by BedMachineV3 thicknesses, as well as all other remaining gaps. The same procedure is followed for the AFTER geometry, considering all strips from 2016-07-01 to 2022-12-31, displaced to 2023-01-01. The

a) Displace based on velocities to a reference date

b) Feature tracking displacement

c) Co-register with respect to BedMachine

d) Calculate a median DEM of all strips

e) Only for AFTER geometry: Replace grounding zone with BEFORE geometry

GROUNDED

FLOATING

f) Interpolate onto BedMachine grid

g) Convert surface elevation to ice thickness

h) Exclude thicknesses > 2000 meters

i) Fill gaps with BedMachine

Figure 4.2: The workflow used to generate the BEFORE and AFTER geometries. The grounding line masking in **(e)** is only done for the AFTER geometry.

feature tracking displacement is performed using the median elevation map between 2018-07-01 and 2022-12-31. The surface elevation in BedMachineV3 is based on the REMA mosaic generated from the strips from 2010-2017, so to reduce inconsistencies in the grounding zone area, we mask out the grounding zone (~1.5 km) in the median (AFTER) surface elevation map and replace the surface elevation here with that from the BEFORE surface elevation map. The replacement is done with the BEFORE elevation map instead of BedMachineV3 to allow for greater spatial details. Like, the BEFORE geometry, ice thickness outliers and all remaining gaps are filled with BedMachineV3 values.
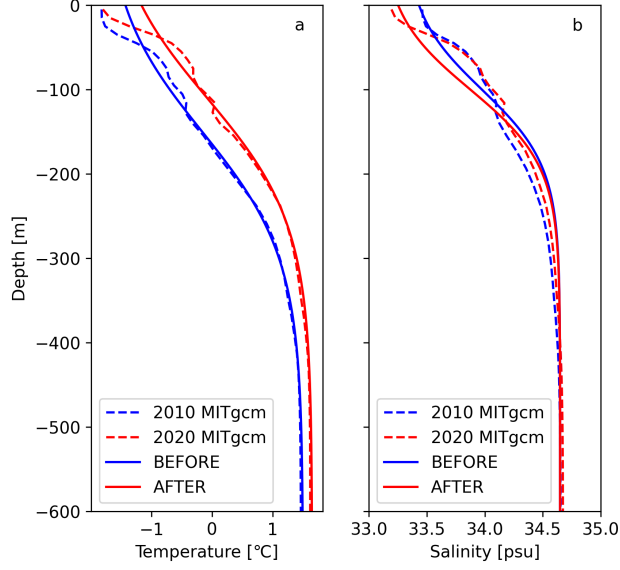
Figure 4.3: Average temperature **(a)** and salinity **(b)** profiles from winter months (May-August) of MITgcm in 2010 (dashed blue) and 2020 (dashed red), alongside with the tangent hyperbolic prescribed temperate **(a)** and salinity **(b)** used in LADDIE for the BEFORE run (solid blue) and AFTER run (solid red).

Ocean forcing

We force LADDIE with a 1D temperature and salinity profile (Lambert et al., 2023) based on MITgcm results from 2010 and 2020 (Hyogo et al., 2024), for the BEFORE and AFTER experiment, respectively. We average the May-August MITgcm temperatures and salinities from the Northern and Southern profiles (Fig. 4.1) to obtain the average forcing for 2010 and 2020 (Fig. 4.3). We only consider Austral winter months (May-August) to reduce the noise level from the seasonality in the upper ocean layers. To avoid sudden changes in temperature and salinity present in the MITgcm outputs and to ensure a stable stratification, we describe both salinity and temperature as a tangent hyperbolic function. For the temperature, the tangent hyperbolic function is already built into LADDIE, where the surface temperature (T_0) is based on the surface salinity (S_0) following

$$T_0 = l_1 S_0 + l_2. \tag{4.1}$$

Here l_1 and l_2 are the freezing point salinity coefficient and the freezing point offset, respectively. The temperature (T) as a function of depth (z) is then given by

$$T(z) = T_1 + (T_0 - T_1)\frac{1 + \tanh\left(\frac{z-z_0}{z_1}\right)}{2}, \tag{4.2}$$

where T_1 is the temperature at depth, z_0 is the reference depth for the thermocline, and z_1 is the scaling factor of the thermocline, which determines the thermocline gradient.

Table 4.1: Forcing parameters used in the BEFORE and AFTER experiments.

Parameter	BEFORE	AFTER
Temperature at depth, T_1 [°C]	1.50	1.65
Thermocline depth, z_0 [m]	-150	-110
Thermocline scaling factor, z_1 [m]	150	150
Freezing point salinity coef., l_1 [°C/psu]	3.733e-5	3.733e-5
Freezing point offset, l_2 [°C]	8.32e-2	8.32e-2
Surface salinity, S_0 [psu]	33.30	33.10
Salinity at depth, S_1 [psu]	34.65	34.65
Halocline depth, $z_{0,S}$ [m]	-100	-100
Halocline scaling factor, $z_{1,S}$ [m]	90	90

The salinity is in LADDIE, however, described by a quadratic function, which does not fit well with the MITgcm outputs, as they roughly follow the same profile as the temperature (Fig. 4.3). We, therefore, use a similar tangent hyperbolic function for the salinity (S) as for the temperature, following

$$S(z) = S_1 + (S_0 - S_1)\frac{1 + \tanh\left(\frac{z - z_{0,S}}{z_{1,S}}\right)}{2}. \tag{4.3}$$

Here, S_1 is the salinity at depth, $z_{0,S}$ is the halocline reference depth (as opposed to the thermocline for the temperature), and $z_{1,S}$ is the halocline scaling factor. Surface salinity, salinity at depth, and temperature at depth are all roughly based on the MITgcm profiles, whereas the thermocline/halocline depths and scaling factors are tuned to match the MITgcm profiles.

For both temperature and salinity the tangent hyperbolic only starts to diverge from the MITgcm profiles at depths above ∼-100 m (Fig. 4.3), which is shallower than the ice shelf draft in most parts of the ice shelf with the exception of a few areas in the northern part of the ice shelf. All forcing parameters for the BEFORE and AFTER experiments are tabulated in Tab. 4.1.

Tuning

Ocean models approximate physical processes, which implies that they need to be tuned in order to match observations. LADDIE has two tuning parameters; the minimum meltwater layer thickness (D_{min}) and the drag coefficient ($C_{d,top}$) applied to the friction velocity in the basal melting formulation (Lambert et al., 2023). We use the latter as the main tuning parameter due to its direct influence on basal melt rates as tuning $C_{d,top}$ roughly corresponds to scaling the basal melting magnitude up and down. To calibrate the model, we iteratively adjust $C_{d,top}$ to approximate the maximum BURGEE melt rates observed near the channel of interest using the BEFORE geometry. Once determined, this value of $C_{d,top}$ remains fixed across the BEFORE and AFTER experiments, allowing

Table 4.2: LADDIE parameters used in both experiments.

Parameter	Value
Time step [s]	36
Equilibrium time [model days]	60
Top drag coefficient, $C_{d,top}$	$3.0 \cdot 10^{-4}$
Minimum thickness, D_{min} [m]	2
Ice temperature [°C]	-25
Tidal velocity [m/s]	0.01
Horizontal viscosity [m^2/s]	6
Horizontal diffusivity [m^2/s]	1

us to focus on the effects of changing geometry and forcing. The full list of model parameters specific for our experiments is provided in Tab. 4.2.

4.4   Results

The basal melt rate trend from 2010 to 2022, shown in Fig. 4.1, reveals a general pattern consistent with previous studies (Davison et al., 2023): higher melt rates are observed in the southern region of the ice shelf compared to the north. Furthermore, as is typical for most ice shelves, the highest melt rates are concentrated near the grounding zone, with channels extending from these zones across mainly the southern part of the ice shelf. A closer examination of the newly identified channel highlights its position within a densely channelized area. This channel stands out with exceptionally high melt rates, reaching up to approximately 30 m/yr, which surpasses the melt rates in the surrounding channels. The channel appears to intersect existing channels, complicating the interpretation of the meltwater plume's pathway.

By examining the surface elevations over the study period, it becomes evident that the new channel has developed during this period; it began forming around 2015, reflected by a narrow surface depression in Fig. 4.4d. This depression deepens progressively throughout the study period by 23 m between 2013/14 and 2022/2023, with two further key observations emerging. First, as the depression associated with the channel becomes more pronounced (Fig. 4.4j, around 11 km), the deepest part of the older channel becomes shallower (Fig. 4.4j, around 8 km), while the flanks of the older channel are lowering (Fig. 4.4j, around 4-8 km and 9-10 km), thereby widening this pre-existing channel. These flanks are also associated with high melt rates ($\sim$ 15 m/yr, Fig. 4.1), as opposed to the deepest part of the channel ($\sim$ 0 m/yr, Fig. 4.1). The continuous lowering of the flanks suggests that the channel system is not in a steady state, with the closure of the deepest part possibly indicating channel re-routing, where the new channel may now serve as the primary basal melt pathway. Second, just downstream of the channel (Fig. 4.4j, around 12 km) a slight surface elevation bump appears from 2016/17 onward. This type of bump, known as flanking uplift, is typically associated with fractures on
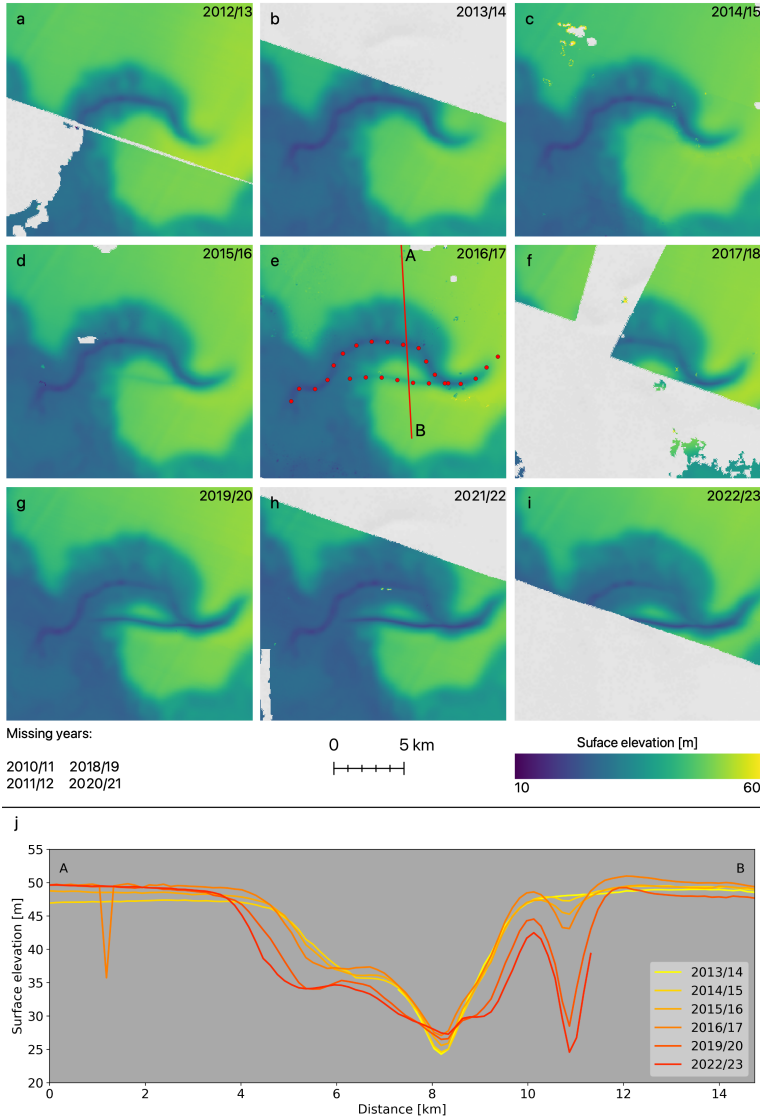
Figure 4.4: **(a-i)** surface elevations through time from 2012/13 in **(a)** to 2022/23 in **(i)**. In panel e the old/persistent and new channel are marked by red dots. The missing years indicated in the legend are years without REMA coverage in this area. **(j)** shows the surface elevations in a Lagrangian framework along the transect marked and lettered for direction in **(e)** which crosses both the persistent channel (surface depression deepest at around 8.2 km) and the new channel (around 11 km). The sudden dip around 1 km in one of the surface elevations is caused by a few contaminated pixels in that given REMA strip.

ice shelves (Walker and Gardner, 2019). These findings suggest that the channel could either be a fracture, a basal melt channel, or a combination of both (i.e., a fracture that serves as a melt plume pathway or a channel that has begun to fracture). Since both basal channels and fractures can weaken ice shelves (Alley et al., 2022, 2024), the presence of either on George VI, a relatively thin ice shelf with a relatively warm atmosphere, likely contributes to its weakening (Smith et al., 2007).

To further investigate fracturing as a possible driver behind such a fast developing channel we explore changes in ice flow across the channel. Ice shelf fracturing is typically linked to variations in ice speed and divergence caused by stretching. Our analysis of ice speed and divergence across the channel show speeds along the transect fluctuating substantially in both 2014/15 and 2015/16 (Fig. 4.5a and b) from ~370 m/yr to almost ~400 m/yr with an isolated peak in the ice speed at the channel location in 2015/16. That peak is associated with sudden changes in divergence from -0.02 m/yr (compression) just upstream of the channel to 0.03 m/yr (stretching) just downstream of the channel (10-11 km, Fig. 4.5b), which could indicate fracturing as a potential driver of the channel. These changes, however, are rather subtle in comparison to the noise level and to observations across wider fractures (~ 1-4 km) on e.g. Ross Ice Shelf, where divergences reaches 30-80 m/yr at their maximum (Walker and Gardner, 2019). The low magnitude of the changes could potentially be due to the coarse resolution of the velocity product (200 m) relative to the channel's width and depth. Finally, in the later years (2017 and 2020, Fig. 4.5c and d), both ice speeds and divergences are more stable, without any outstanding signals in the vicinity of the channel.

Focusing on changes in ocean heat as possible driver of channel changes, we investigate temporal changes in ocean temperature and salinity. Figure 4.6a-f illustrate temperature and salinity anomalies for the Northern, Middle, and Southern profiles (Fig. 4.1), revealing a regime shift from cold and fresh conditions to warmer and saltier conditions across all profiles. At the Northern profile, this shift begins around 2013, intensifying in 2015/16, after which sub-shelf temperatures remain above the temporal mean. Similar, albeit weaker, trends are observed in the Middle and Southern profiles. In the deeper ocean layers below -300 m, where CDW resides, both average temperature and salinity have increased over the study period across all three profiles (Fig. 4.6g-i). Notably, a jump in salinity is observed around 2016, with the most pronounced increase in the Northern profile (Fig. 4.6g), where the strongest temperature and salinity anomaly shifts also occur (Fig. 4.6a and d), although the average temperature at depth already starts increasing in 2011 (Fig. 4.6g). This shift in ocean regime aligns with the 2015 El Niño Southern Oscillation (ENSO) event, with its effects already having been shown to reach George VI (Boxall et al., 2024). These changes in oceanic conditions, partially driven by ENSO, thus indicate more heat available for basal melting, likely intensifying and accelerating the meltwater plume, which in turn may cause higher melt rates and alterations in the plume pathway, influenced by the ice shelf's evolving geometry. Furthermore, in the Southern temperature anomaly profile, where several melt channels have their outflow (Fig. 4.1), the upper ocean layers have become fresher since 2016 (Fig. 4.6f), possibly indicating increased meltwater outflow.
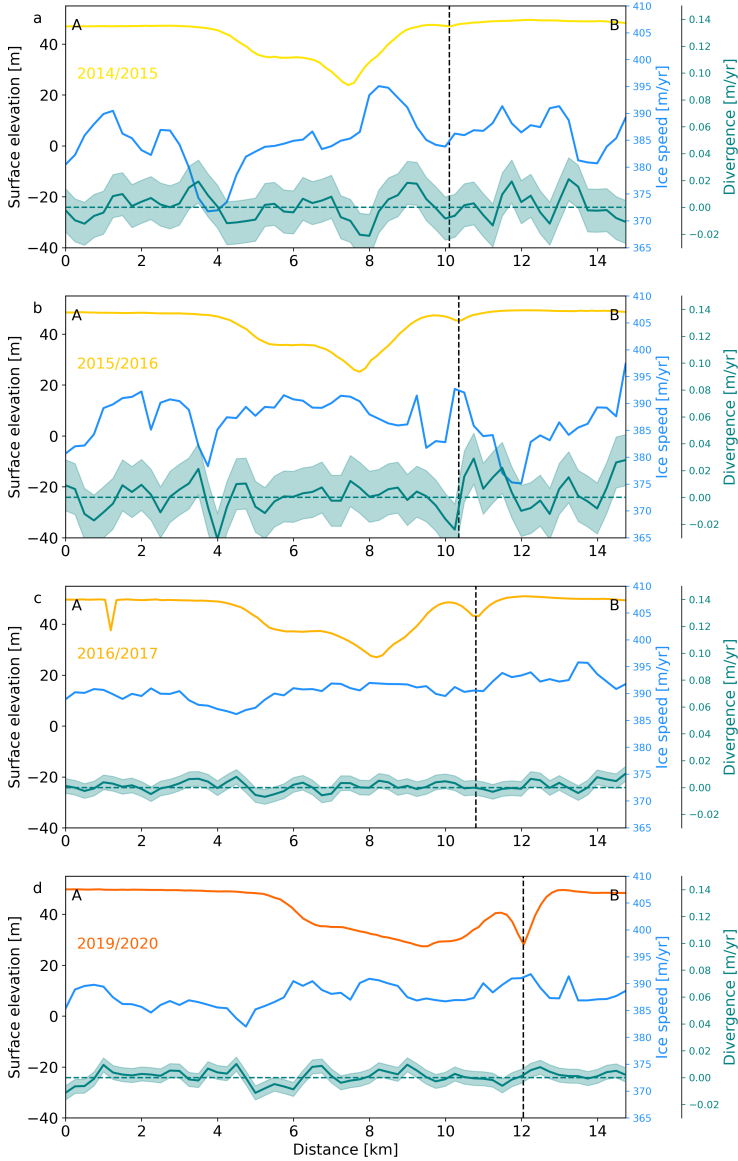
Figure 4.5: Surface elevation (same coloring as in Figure 4.4j), ice speed (blue) and divergence (green), all in a Eulerian framework, along the transect marked in Figure 4.4e. The dashed green line indicate zero divergence, to easier distinguish between stretching (positive values) and compression (negative values). The shaded green area indicates the noise in the signal as described in Sect. 4.3.2. The dashed black line marks the approximate location of the channel. **(a)** is year 2014/15, **(b)** is 2015/16, **(c)** is 2016/17, and **(d)** is 2019/20.
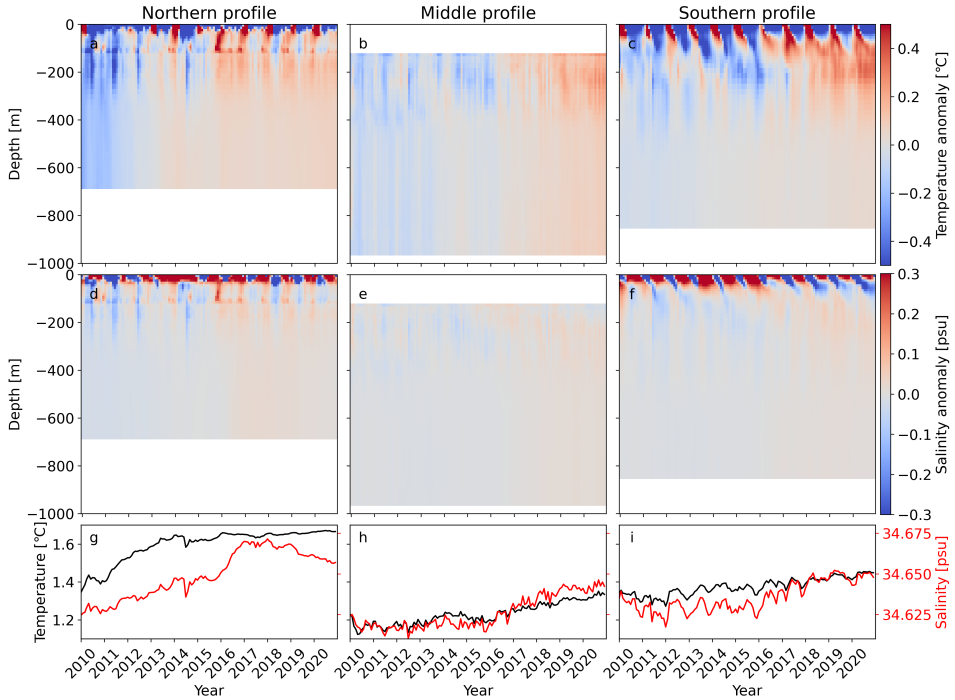
Figure 4.6: MITgcm ocean temperature **(a-c)** and salinity **(d-f)** anomalies of the Northern profile (**(a)** and **(d)**), Middle profile (**(b)** and **(e)**), and Southern profile (**(c)** and **(f)**) as marked in Figure 4.1. Panel **(g-i)** show the average temperature and salinity at all depths <-300 m through time of the Northern profile **(g)**, Middle profile **(h)** and Southern profile **(i)**.

In addition to changes in ocean temperature and salinity, MITgcm model outputs suggest alterations in ocean circulation near the channel (Fig. 4.7). Although there is a disparity in scale between the model grid size and the size of the channel, we can reasonably conclude that changes in ocean circulation likely occurred near the channel between 2010 and 2020, with higher current velocities near the channel. However, interpreting circulation changes in more detail and on a smaller scale, particularly in the immediate vicinity of the channel, remains challenging given the coarse model resolution.

The LADDIE model outputs from the BEFORE and AFTER experiments allow us to zoom in on the channel at a finer resolution, enabling us to explore how changes in ice shelf geometry and ocean forcing affect basal melt patterns. The modeled melt rate patterns (Fig. 4.8) align well with observations in areas outside the channel (Fig. 4.1). Figure 4.8f shows that LADDIE suggests the channel could serve as a pathway for the meltwater plume, potentially contributing to the high melt rates within the channel itself. Moreover, both BEFORE and AFTER melt patterns show enhanced melt along the
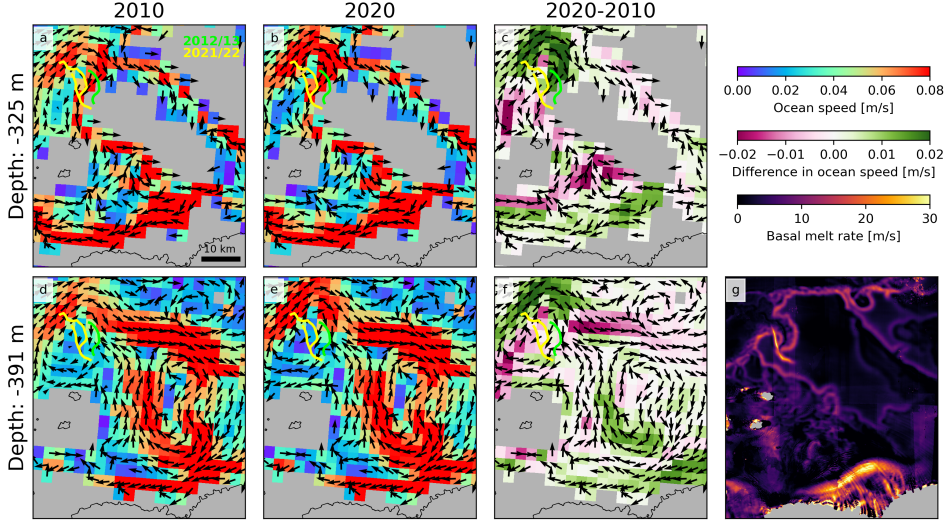
Figure 4.7: Yearly averaged ocean circulation in the vicinity of the channel in 2010 (**(a)** and **(d)**), 2020 (**(b)** and **(e)**), and the difference between the two (**(c)** and **(f)**) at two different depths (-325 m in **(a-c)** and -391 m in **(d-f)**) which roughly corresponds to the layers right below the ice shelf base. The arrows in panel **(c)** and **(f)** correspond to the ocean circulation directions in 2020. The locations of the original and the new channel from 2012/13 and 2021/22 are marked in green and yellow, respectively. The BURGEE melt rates in **(g)** are shown for easier orientation.

sides of the channel, similar to BURGEE, which explains the widening of the old channel seen in Fig. 4.4j. Notably, the observed BURGEE melt pattern (Fig. 4.1) near the channel appears to combine elements from both the BEFORE and AFTER experiments, with channels following the "original" channel system as in the BEFORE scenario combined with high melt rates within the new channel as in the AFTER scenario. This strong agreement between observations and models suggests that the plume pathway may have shifted during the BURGEE observational period, now following a new route as indicated by the AFTER experiment.

4.5   Discussion

In this study, we uncovered a new channel within the channelized basal melting network of the George VI Ice Shelf, characterized by rapid changes in surface elevation, from 48 m in 2013/14 to 25 m in 2022/23. The onset of this channel coincides with both a shift towards a warmer ocean regime as well as subtle divergence changes across the channel, both aligning with the 2015 ENSO event (Boxall et al., 2024). ENSO has already been linked to an intensified inflow of CDW onto the continental shelf during El Niño years (Huguenin et al., 2024), supporting the MITgcm results of a warmer regime

Figure 4.8: **(a-c)** Ice shelf draft, plume velocity, and basal melt rate in the BEFORE experiment. **(d-f)** Same as **(a-c)** but for the AFTER experiment. Arrows on the ice shelf draft (**(a)** and **(d)**) are the plume velocities. The dashed green line in **(c)** marks the location of the original channel in 2012/13 and the dashed green line **(f)** marks the location of the new channel in 2021/22.
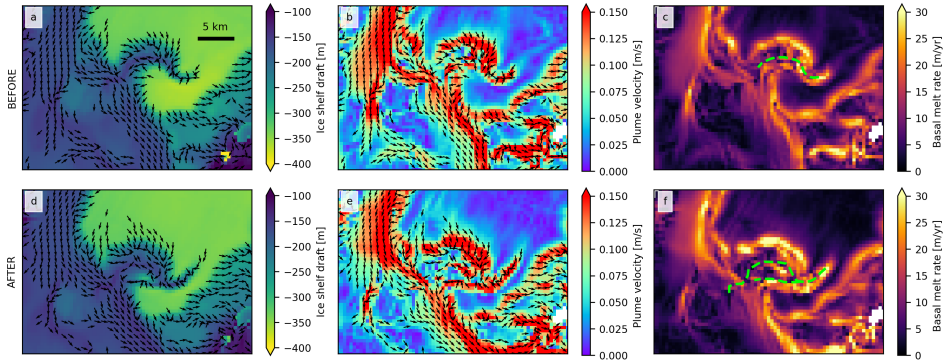
after 2015. The 2015 ENSO event has further been linked to the acceleration of glaciers feeding into the George VI Ice Shelf (Boxall et al., 2024). ENSO events have additionally been shown to enhance basal melting on ice shelves in the Amundsen Sea Sector (Paolo et al., 2018). While we cannot definitively conclude that ENSO caused the appearance of this channel, the timing is notable and the potential link to ENSO is important, as the projected increase in El Niño frequency suggest even further acceleration of ice shelf basal melting in Antarctica in the future (Cai et al., 2023).

The observed new channel could represent a basal melt channel, a fracture, or a combination of both and our investigations of the channel's origin point towards both the latter. The uplift in the surface near the depression, coupled with signs of stretching in the divergence field downstream of the channel in 2015/16, suggests fracturing. However, these signals are subtle, leaving us unable to confirm or dismiss the possibility of fracturing with certainty. At the same time, changes in ocean temperature, salinity, and circulation point to evolving and strengthening basal melt conditions that could encourage channel re-routing. Our LADDIE modelling results further support this possibility, indicating that even if the channel originated as a fracture, the meltwater plume may now be using it as a new pathway, which could further deepen the fracture, provided the initial fracture has a basal component.

To assess the potential impact of the new channel on the weakening of George VI Ice Shelf, we can draw parallels to other ice shelves where interactions between basal melt channels and fractures have led to structural instability. A notable example is Pine Island Ice Shelf, where a channel first observed in the 1970s progressively thinned and extended over time (Alley et al., 2022, 2024). This channel triggered both transverse fractures and fractures along the channel's length, eventually leading to calving and retreat along the channel from approximately 2018 to 2022 (Alley et al., 2022, 2024).

The new channel on George VI Ice Shelf is located just about 30 km from the southern edge, raising concerns that continued melting, thinning, and weakening in this region could drive significant structural changes. These changes may include enhanced fracturing, calving, and ultimately, retreat of the ice shelf in this highly channelized area. Given projections of increased ocean heat availability in the future (Naughten et al., 2023), basal melting is expected to intensify, further amplifying the vulnerability of this portion of George VI Ice Shelf.

To definitively determine whether the channel is a fracture, a basal melt channel, or a combination of the two, in-situ field measurements, including basal melt rates, ice deformation monitoring, and radar surveys of ice thickness, are necessary. Regardless of its specific nature, this channel offers a direct observation of weakening in a highly channelized, vulnerable portion of the ice shelf. These results underscore how quickly ice shelf channels - important for ice shelf integrity - can occur and how easily small-scale changes might go unnoticed. Closely observing the continued evolution of the ice shelf and its integrity will be crucial in understanding these weakening processes. Such knowledge could also be valuable for other heavily channelized ice shelves, like Pine Island and Totten, which both have a higher projected potential sea level rise contribution.

4.6   Conclusions

Our study highlights the rapid emergence of a significant channel on the George VI Ice Shelf, marked by a 23 m surface lowering over just nine years. The appearance of the channel aligns with both changes in ocean forcing, most notably increased ocean temperatures and salinity, and subtle changes in ice divergence, both of which coincide with the timing of a major ENSO event. While the exact link between ENSO and the development of this channel remains speculative, the temporal correlation suggests that large-scale climate patterns may have a role in amplifying basal melting and possibly in re-routing meltwater pathways on Antarctic ice shelves.

The presence of such a fast-evolving channel on an already thin and vulnerable ice shelf like George VI likely has destabilizing effects, accelerating its weakening through both basal melting and fracturing. The behavior of this channel on George VI may offer valuable insights into how sudden changes in ocean forcing could trigger similar destabilizing processes elsewhere.

Moving forward, continuous monitoring of this channel and its evolving impact on George VI is crucial. The lessons learned from tracking its development may provide critical information on the future behavior of other highly channelized ice shelves undergoing changes in ocean conditions. Understanding these processes is essential for better projecting potential ice shelf retreat and the associated contributions to global sea-level rise.

Code and data availability

The BURGEE code is publicly available at `https://github.com/aszinck/BURGEE` (Zinck, 2023), likewise is LADDIE (`https://github.com/erwinlambert/laddie`). The derived melt rates as well as surface elevations are available at `https://doi.org/10.4121/dbf9ade9-9f85-49f4-89ba-3d8d8310c9e4`. The REMA strips are available from the Polar Geosptaital Center (`https://www.pgc.umn.edu/data/rema/`) and CryoSat-2 data is available from the European Space Agency (`https://earth.esa.int/eogateway/documents/20142/37627/CryoSat-Baseline-D-Product-Handbook.pdf`). BedMachine V3 is available from NASA National Snow and Ice Data Center (`https://nsidc.org/data/NSIDC-0756/versions/3`), likewise are MEaSUREs ITS_LIVE velocities (`https://doi.org/10.5067/6II6VW8LLWJ7` and `https://nsidc.org/data/NSIDC-0756/versions/3`). The ENVEO monthly velocities provided by the European Space Agency's Antarctic Ice Sheet Climate Change Initiative project are available from `https://cryoportal.enveo.at/data/`. The regional MITgcm model output is available from `https://ecco.jpl.nasa.gov/drive/files/ECCO2/LLC1080_REG_AMS/Hyogo_et_al_2022` (Hyogo et al., 2024).

4

Chapter 5

Conclusions and Outlook

The aim of this thesis was to develop improved remote sensing methods for capturing small-scale basal melting features, such as basal channels, enhance our understanding of their impact on ice shelf weakening, and to explore their link to external drivers. This aim was addressed through three research questions. This chapter summarizes the key findings by providing answers to all these three research questions and further investigates future research directions.

5.1   Conclusions

What is the added value of using a combination of REMA stereo imagery and satellite altimetry in resolving ice shelf basal melt patterns?

This research question was addressed in Chapter 2 by developing the BURGEE method. BURGEE uses a combination of satellite radar altimetry from CryoSat-2 and the REMA stereo imagery strips to generate high spatial resolution ice shelf elevations changes and basal melt maps. It was shown that BURGEE is capable of capturing small-scale features such as basal channels by applying BURGEE to the Dotson Ice Shelf. The 50 m posting BURGEE basal melt maps revealed spatial variability within a major melt channel that had not been fully resolved with coarser resolution remote sensing products relying on altimetry only. Notably, we identified that a pinning point influences the channel's melt variability, underlining the critical role of high-resolution basal melt products in uncovering melt channel patterns and possible mechanisms behind channel pattern formation. This spatial variability within the channel is related to the fact that remote sensing basal melt products that rely solely on CryoSat-2 altimetry have reduced coverage in steep terrain areas. This includes regions like basal channels and grounding zones surrounded by mountains, where CryoSat-2 only measures the point closest to the satellite, leaving these areas unseen. Finally, BURGEE is build to make use of the Google Earth Engine (which stores the first version of the REMA strips across the entire

Antarctic continent) and to be free of site-specific tuning, which makes BURGEE easily scalable. Hence, this work established a scalable methodology that can be applied to any ice shelf without the need of high local computational power due to the usage of Google Earth Engine. Thus, it provides a powerful tool for understanding ice shelf (in)stability at high spatial resolution.

Besides Chapter 2, also Chapter 3 shed further light on this research question. This study provided valuable insights for improving ice sheet models by identifying the spatial resolution (500 m) required to capture channelized melting effectively. An analysis of the basal melting wavelength power spectra of the remote sensing basal melt products examined in Chapter 3 demonstrated that only BURGEE, with its 50 m grid spacing, reaches a noise level in its power spectrum (approximately constant power level for increasing frequencies), whereas the two atimetry-only studies (Adusumilli et al., 2020; Davison et al., 2023) did not. This indicates that BURGEE uniquely captures the full range of wavelengths and frequencies at which (channelized) melting occurs.

To summarize, the added value of using a combination of REMA and CryoSat-2 altimetry is that it provides an automated workflow of obtaining high-resolution basal melt rates on a rather large scale in Antarctica. Furthermore, the high-resolution product allows for detecting basal melting in areas surrounded by steep terrain. This especially becomes evident in basal channels, where this combination of stereo imagery and altimetry allows for surveying the full depth of basal channels, and thus also explore the highest melt rates within basal channels, unlike radar-altimetry-only products.

What is the impact of high resolution basal melt maps in assessing basal channel melt rates and ice shelf channel vulnerability?

By making use of the BURGEE methodology and its scalability, we generated and analyzed basal melt maps of some of the most vulnerable ice shelves in Antarctica in Chapter 3. These high-resolution maps revealed that peak melt rates within basal channels are significantly underestimated in existing products relying on radar altimetry only by as much as 42–50%. The peak melt rates were further used to calculate the time it would take for a channel to break through, as an indicator of channel, and thus ice shelf, vulnerability. This analysis showed that the peak melt rate underestimation has significant implications on breakthrough, as it suggests that channels might break through, or lead to other destabilizing processes such as fracturing, more rapidly and weaken ice shelves more extensively than previously thought. These results underscore the importance of incorporating channelized melting at high spatial resolutions, or at least the consequences thereof through parametrization, in ice sheet models to more accurately model ice shelf stability with the ultimate goal of improving sea level rise predictions.

To which extent can changes in basal channel patterns be linked to changes in external drivers?

This research question was addressed in Chapter 4, where a fast-developing channel on George VI Ice Shelf was studied. Its rapid formation can be a result of fracturing, basal melting, or a combination of the two. We found evidence of the latter, thus of a dual process where likely both basal melting and fracturing contributed to the channel's formation. The channel was found to experience a 23 m surface lowering over a period of just 9 years, with its emerge coinciding with significant changes in ocean forcing alongside subtle changes in flow, both coinciding with a strong ENSO event in 2015. This study provided insights into how external drivers, such as large-scale climate patterns, can possibly amplify basal melting and reroute meltwater plumes, accelerating ice shelf weakening through potentially both melting and fracturing. These findings emphasize the need for continuous monitoring and further research into the interplay between ocean forcing and ice shelf channel dynamics (fracturing and melting), especially on thin and vulnerable ice shelves like George VI. Some of these future possibilities are further highlighted in Sect. 5.2.1.

5.1.1   Synthesis

This thesis has advanced our understanding of ice shelf basal melting by introducing improved remote sensing methodologies, delivering new insights into the dynamics and vulnerability of basal channels, and identifying links between channel evolution and external forcing.

A key advancement lies in the use of high-resolution REMA elevations in combination with CryoSat-2 altimetry observations, which enable the detection of basal melting in areas with steep terrain, features that have remained largely unresolved by radar altimetry-based products. This is particularly significant for grounding zones surrounded by complex topography and, maybe more importantly, for capturing small-scale features such as basal channels.

The improved ability to resolve basal channels has revealed that channelized melting is far more widespread and intense than previously recognized. The latter has significant implications for assumptions about ice shelf weakening, as basal channels can act as critical zones of structural vulnerability, accelerating fracturing and retreat.

Moreover, the greater spatial detail provided by BURGEE offers a validation reference for ocean models, enabling them to better simulate channelized melting processes. The resolution at which channelized melting should be resolved in models is further outlined in the power spectrum analysis presented in Fig. A.4. Figure A.4 shows that the BURGEE signal approaches its noise level at a frequency of ~ 0.002 m^{-1}, corresponding to a wavelength of approximately 500 m. This indicates that ice-ocean models should resolve basal melting processes at spatial scales of at least this wavelength to accurately represent channelized melting dynamics.

Additionally, the identified link between large-scale climatic phenomena, such as El

Niño, and changes in basal channel melt patterns highlights the broader climate sensitivity of Antarctic ice shelves. Given projections of stronger and more frequent El Niño events under future climate scenarios, capturing the impact of channelized melting becomes increasingly critical for predicting ice shelf behavior.

Collectively, these contributions provide a foundation for future research aimed at understanding changes in basal melting patterns and the impact of small-scale basal melting on ice shelf stability to better predict the fate of Antarctic ice shelves and their role in global sea level rise.

5.2 Outlook

This thesis has advanced the knowledge of ice shelf basal melting, but many critical unknowns remain. Below, I outline some future opportunities that could address key gaps and further enhance our understanding of basal melting, particularly channelized melting, and its implications for ice shelf stability. I further expand on how principles from BURGEE can be applied to other aspects of cryospheric research. Common for all future opportunities outlined in the following subsection, is the need for integrated approaches, combining advanced remote sensing, in-situ observations, and modelling, to address the pressing research gaps in ice shelf basal melting, but also in cryospheric research as a whole.

5.2.1 Continued monitoring of channels on George VI Ice Shelf

Chapter 4 demonstrated that the channel system on George VI Ice Shelf is undergoing changes that likely only have destabilizing effects on the ice shelf. While Chapter 4 provided valuable initial insights into the drivers behind these changes, important questions remain unanswered. For instance, it became clear that the channel formation possibly involved both basal channels and fracturing. However, the actual interplay between melting and fracturing, as well as which of the two caused the emergence of the new channel, requires further investigation. Furthermore, the implications for ice shelf stability are still unclear, and continued monitoring of the long-term evolution of the channel system on George VI is essential.

Future efforts could involve deploying autonomous phase-sensitive radio echo sounders (ApRES) across the channel network to monitor internal ice displacements, basal melting, and ice flow variations. Complementary observations using underwater autonomous vehicles (such as ICEFIN) could enhance understanding by providing optical imagery and ocean properties measurements from within the channels. Such observations would help clarify the processes driving channel migration and the interaction between basal melting and fracturing. It might further shed light on the origin of the channel as to whether it originated as a fracture or a basal melt channel.

High-resolution coupled ice-ocean modeling has the possibility to further project channel evolution and their influence on ice shelf stability. Although such models are currently limited to idealized scenarios (Jesse et al., 2024), George VI Ice Shelf offers an

ideal testbed due to its relatively simplified ice dynamics, detached from the complexities of the main Antarctic Ice Sheet. Applying high-resolution coupled ice-ocean models that are capable of capturing the dynamics of basal channels, both from an ocean and ice flow perspective, could significantly improve projections of channel impacts on ice shelf stability under varying climate scenarios.

5.2.2 Aligning in-situ and remote sensing observations of basal melting

Despite advancements in basal melt rate estimation, understanding and quantifying uncertainties in remote sensing basal melt products remain a major challenge. This is largely because the inputs to the mass conservation equation used in these estimates are highly correlated. For example, firn densification models, which account for air content within the firn layer when applying hydrostatic equilibirum, rely on outputs from regional climate models. The surface mass balance estimates, used to correct for atmospherically-driven thinning at the surface, are typically taken from the same regional climate model. Additionally, the assumption of hydrostatic equilibrium itself also leads to substantial uncertainties, especially near grounding zones. Addressing these intertwined uncertainties through comprehensive statistical analysis is nearly impossible due to the complexity of the models and the computational demands.

In Chapter 3, the BURGEE melt rates were compared to several remote sensing products, showing that while total melt rates across datasets were broadly consistent, channelized melting was notably underestimated in altimetry-only studies. Although this comparison increases confidence in the overall melt rate estimates, it does not validate small-scale melting features or address uncertainties related to hydrostatic equilibrium assumptions near grounding zones.

To address these limitations and refine remote sensing melt products, integrating in-situ observations with remote sensing data is essential. Both methods have complementary strengths and weaknesses. In-situ methods, such as ApRES and oceanographic measurements, offer either high temporal resolution at specific points or high spatial resolution temporal snapshots along lines. On the other hand, remote sensing products offer grid-based data with melt rates calculated as trend over a longer time period. Aligning a point or line measurement with a grid cell or comparing observations that reference different time frames complicates such analyses further, especially given the Lagrangian procedure of many remote sensing products.

A focused field campaign could bridge this gap and provide invaluable insights into basal melting across spatial and temporal scales. By simultaneously deploying a dense network of ApRES stations, ocean moorings, and regular ICEFIN missions on a single ice shelf, combined with remote sensing-derived melt maps covering the same period, it would be possible to better constrain uncertainties and validate small-scale melt features. This comprehensive, multi-year campaign would facilitate a robust comparison of basal melt dynamics across both methods, improving interpretations of melt rates and their drivers.

The Dotson-Crosson ice shelf system presents an ideal region for such a study due to its diverse basal melting dynamics and good REMA coverage. This system offers multiple opportunities to address key scientific questions. For example, in-situ measurements in the shear zone between Dotson and Crosson could help disentangle shear-related signals from basal melt estimates derived via remote sensing. The complex basal channel networks on Dotson and between the shelves provide an opportunity to study cavity circulation and temporal changes in channelized melting. Additionally, comparing ICEFIN measurements near the retreating grounding zone of Smith Glacier with remote sensing-derived melt rates could help reduce uncertainties in areas where hydrostatic equilibrium assumptions break down.

By focusing on these key features – shear zones, basal channels, and grounding zones – a well-coordinated field campaign in the Dotson-Crosson system would not only advance our understanding of basal melting but also improve the reliability of remote sensing products in critical, dynamic environments.

5.2.3   Towards high spatio-temporal resolution basal melt rates

Capturing temporal and spatial variability in basal melting is essential, especially for understanding how basal channels evolve and impact ice shelf stability. However, current datasets are limited. Methods like BURGEE offer high spatial resolution but are limited in temporal resolution, with mean melt values calculated over 5-10 years. Conversely, high temporal resolution products lacks spatial resolution (e.g., 3-monthly trends in 10 km grids Adusumilli et al., 2020) and thus fail to resolve small-scale features like channels.

To address these limitations, combining datasets through data fusion techniques is a potential solution. While BURGEE does make use of CryoSat-2 altimetry in the REMA strip co-registration, there is still potential for including CrySat-2 swath data in filling REMA strip gaps. Regression or machine learning methods may make it possible to increase the spatial resolution and coverage of the CryoSat-2 swath data by using information from the REMA strips in areas where both are available. Such a data fusion could potentially lead to high spatio-temporal surface elevation maps.

A similar data fusion method has recently lead to great success in creating yearly 500 meters resolution coastal elevation maps in Greenland using the ArcticDEM mosaic (Arctic pendant to REMA) in combination with ICESat-2 and CryoSat-2 (Winstrup et al., 2024). It is therefore likely that even finer resolutions, both temporal and spatial, might be possible by using REMA/ArcticDEM strips as opposed to the mosaic.

Such a high resolution dataset would allow for a detailed spatio-temporal examination of channelized melting, including seasonal variability and the mechanisms driving changes. Additionally, the high resolution spatio-temporal ice shelf elevation changes would provide critical benchmarks for refining ice-ocean models, enhancing predictions of ice shelf evolution, stability, and contributions to sea level rise.

5.2.4 Applying BURGEE concepts to the Arctic

One of the central components of the BURGEE methodology is the co-registration of REMA strips with CryoSat-2, which generates high-resolution digital elevation models capable of tracking temporal changes in surface elevation. Adapting this approach to the Arctic, using ArcticDEM strips, could produce similarly high-resolution surface elevation changes for regions in the Arctic.

For example, these elevation changes could be utilized to estimate the basal melt rates of Greenland's remaining ice shelves, many of which are rapidly retreating and disintegrating (Millan et al., 2023). Applying the BURGEE methodology in this context could offer valuable insights into the processes driving the disintegration, particularly the interaction between basal melt channels and fractures.

In addition, the high-resolution surface elevation change data could address gaps in ice thickness observations for glaciated regions outside the two main ice sheets, where most existing thickness estimates are derived from global glacier modeling efforts and only a handful of localized studies provide detailed estimates (e.g. Zinck and Grinsted, 2022). By exploiting this data with inverse modeling or mass conservation approaches, it would be possible to create a comprehensive high-resolution dataset of ice thickness and the changes therein for Arctic glaciers and ice caps. Such a dataset would offer detailed insights into ice thickness and bedrock topography, greatly improving ice sheet models for reconstructing past ice dynamics, analyzing present conditions, and forecasting the future response of Arctic ice caps to a warming climate.

Bibliography

Adusumilli, S., Fricker, H. A., Medley, B., Padman, L., and Siegfried, M. R.: Interannual variations in meltwater input to the Southern Ocean from Antarctic ice shelves, Nature Geoscience, 13, 616–620, https://doi.org/10.1038/s41561-020-0616-z, 2020.

Albrecht, T. and Levermann, A.: Fracture-induced softening for large-scale ice dynamics, The Cryosphere, 8, 587–605, https://doi.org/10.5194/tc-8-587-2014, 2014.

Alley, K. E., Scambos, T. A., Siegfried, M. R., and Fricker, H. A.: Impacts of warm water on Antarctic ice shelf stability through basal channel formation, Nature Geoscience, 9, 290–293, https://doi.org/10.1038/ngeo2675, 2016.

Alley, K. E., Scambos, T. A., Alley, R. B., and Holschuh, N.: Troughs developed in ice-stream shear margins precondition ice shelves for ocean-driven breakup, Science Advances, 5, 1–8, https://doi.org/10.1126/sciadv.aax2215, 2019.

Alley, K. E., Scambos, T. A., and Alley, R. B.: The role of channelized basal melt in ice-shelf stability: recent progress and future priorities, Annals of Glaciology, 63, 18–22, https://doi.org/10.1017/aog.2023.5, 2022.

Alley, K. E., Alley, R. B., Crawford, A. D., Ochwat, N., Wild, C. T., Marson, J., Snow, T., Muto, A., Pettit, E. C., Child, S. F., Truffer, M., Collao-Barrios, G., and Scambos, T. A.: Evolution of sub-ice-shelf channels reveals changes in ocean-driven melt in West Antarctica, Journal of Glaciology, pp. 1–15, https://doi.org/10.1017/jog.2024.20, 2024.

Andersen, O., Knudsen, P., and Stenseng, L.: The DTU13 MSS (Mean Sea Surface) and MDT (Mean Dynamic Topography) from 20 Years of Satellite Altimetry, in: IGFS 2014, edited by Jin, S. and Barzaghi, R., pp. 111–121, Springer International Publishing, Cham, https://doi.org/10.1007/1345{_}2015{_}182, 2015.

Bamber, J. L., Oppenheimer, M., Kopp, R. E., Aspinall, W. P., and Cooke, R. M.: Ice Sheet and Climate Processes Driving the Uncertainty in Projections of Future Sea Level Rise: Findings From a Structured Expert Judgement Approach, Earth's Future, 10, 1–13, https://doi.org/10.1029/2022EF002772, 2022.

Banwell, A. F., MacAyeal, D. R., and Sergienko, O. V.: Breakup of the Larsen B Ice Shelf triggered by chain reaction drainage of supraglacial lakes, Geophysical Research Letters, 40, 5872–5876, https://doi.org/10.1002/2013GL057694, 2013.

Bassis, J. and Ma, Y.: Evolution of basal crevasses links ice shelf stability to ocean forcing, Earth and Planetary Science Letters, 409, 203–211, https://doi.org/10.1016/j.epsl.2014.11.003, 2015.

Bentley, M. J., Ó Cofaigh, C., Anderson, J. B., Conway, H., Davies, B., Graham, A. G., Hillenbrand, C.-D., Hodgson, D. A., Jamieson, S. S., Larter, R. D., Mackintosh, A., Smith, J. A., Verleyen, E., Ackert, R. P., Bart, P. J., Berg, S., Brunstein, D., Canals, M., Colhoun, E. A., Crosta, X., Dickens, W. A., Domack, E., Dowdeswell, J. A., Dunbar, R., Ehrmann, W., Evans, J., Favier, V., Fink, D., Fogwill, C. J., Glasser, N. F., Gohl, K., Golledge, N. R., Goodwin, I., Gore, D. B., Greenwood, S. L., Hall, B. L., Hall, K., Hedding, D. W., Hein, A. S., Hocking, E. P., Jakobsson, M., Johnson, J. S., Jomelli, V., Jones, R. S., Klages, J. P., Kristoffersen, Y., Kuhn, G., Leventer, A., Licht, K., Lilly, K., Lindow, J., Livingstone, S. J., Massé, G., McGlone, M. S., McKay, R. M., Melles, M., Miura, H., Mulvaney, R., Nel, W., Nitsche, F. O., O'Brien, P. E., Post, A. L., Roberts, S. J., Saunders, K. M., Selkirk, P. M., Simms, A. R., Spiegel, C., Stolldorf, T. D., Sugden, D. E., van der Putten, N., van Ommen, T., Verfaillie, D., Vyverman, W., Wagner, B., White, D. A., Witus, A. E., and Zwartz, D.: A community-based geological reconstruction of Antarctic Ice Sheet deglaciation since the Last Glacial Maximum, Quaternary Science Reviews, 100, 1–9, https://doi.org/10.1016/j.quascirev.2014.06.025, 2014.

Berger, S., Drews, R., Helm, V., Sun, S., and Pattyn, F.: Detecting high spatial variability of ice shelf basal

mass balance, Roi Baudouin Ice Shelf, Antarctica, The Cryosphere, 11, 2675–2690, https://doi.org/10.5194/tc-11-2675-2017, 2017.

Boxall, K., Christie, F. D., Willis, I. C., Wuite, J., Nagler, T., and Scheiblauer, S.: Drivers of Seasonal Land-Ice-Flow Variability in the Antarctic Peninsula, Journal of Geophysical Research: Earth Surface, 129, https://doi.org/10.1029/2023JF007378, 2024.

Cai, W., Jia, F., Li, S., Purich, A., Wang, G., Wu, L., Gan, B., Santoso, A., Geng, T., Ng, B., Yang, Y., Ferreira, D., Meehl, G. A., and McPhaden, M. J.: Antarctic shelf ocean warming and sea ice melt affected by projected El Niño changes, Nature Climate Change, 13, 235–239, https://doi.org/10.1038/s41558-023-01610-x, 2023.

Chartrand, A. M. and Howat, I. M.: Basal Channel Evolution on the Getz Ice Shelf, West Antarctica, Journal of Geophysical Research: Earth Surface, 125, https://doi.org/10.1029/2019JF005293, 2020.

Chartrand, A. M., Howat, I. M., Joughin, I. R., and Smith, B. E.: Thwaites Glacier thins and retreats fastest where ice-shelf channels intersect its grounding zone, The Cryosphere, 18, 4971–4992, https://doi.org/10.5194/tc-18-4971-2024, 2024.

Chartrand, R.: Numerical Differentiation of Noisy, Nonsmooth Data, ISRN Applied Mathematics, 2011, 1–11, https://doi.org/10.5402/2011/164564, 2011.

Chartrand, R.: Numerical differentiation of noisy, nonsmooth, multidimensional data, in: 2017 IEEE Global Conference on Signal and Information Processing (GlobalSIP), vol. 2018-Janua, pp. 244–248, IEEE, https://doi.org/10.1109/GlobalSIP.2017.8308641, 2017.

Cuffey, K. M. and Paterson, W.: The Physics of Glaciers, Elsevier, 4 edn., URL https://www.elsevier.com/books/the-physics-of-glaciers/cuffey/978-0-12-369461-4, 2010.

Cuffey, K. M. and Paterson, W. S. B.: The Physics of Glaciers, Academic Press, 4 edn., 2006.

Davison, B. J., Hogg, A. E., Gourmelen, N., Jakob, L., Wuite, J., Nagler, T., Greene, C. A., Andreasen, J., and Engdahl, M. E.: Annual mass budget of Antarctic ice shelves from 1997 to 2021, Science Advances, 9, https://doi.org/10.1126/sciadv.adi0186, 2023.

de Roda Husman, S., Lhermitte, S., Bolibar, J., Izeboud, M., Hu, Z., Shukla, S., van der Meer, M., Long, D., and Wouters, B.: A high-resolution record of surface melt on Antarctic ice shelves using multi-source remote sensing data and deep learning, Remote Sensing of Environment, 301, 113 950, https://doi.org/10.1016/j.rse.2023.113950, 2024.

Dehecq, A., Gourmelen, N., Shepherd, A., Cullen, R., Trouv, E., Dehecq, A., Gourmelen, N., Shepherd, A., Cullen, R., and Trouv, E.: Evaluation of CryoSat-2 for height retrieval over the Himalayan range, CryoSat-2 third user workshop, Dresden, Germany, URL https://hal.science/hal-00973393, 2013.

Doemgaard, M., Millan, R., Andersen, J., Scheuchl, B., Rignot, E., Izeboud, M., and Bjørk, A.: Half a century of extensive acceleration and grounding line retreat following the ocean driven collapse of Wordie Ice Shelf, https://doi.org/10.21203/rs.3.rs-4778150/v1, 2024.

Dow, C. F., Lee, W. S., Greenbaum, J. S., Greene, C. A., Blankenship, D. D., Poinar, K., Forrest, A. L., Young, D. A., and Zappa, C. J.: Basal channels drive active surface hydrology and transverse ice shelf fracture, Science Advances, 4, https://doi.org/10.1126/sciadv.aao7212, 2018.

Drews, R.: Evolution of ice-shelf channels in Antarctic ice shelves, The Cryosphere, 9, 1169–1181, https://doi.org/10.5194/tc-9-1169-2015, 2015.

Drews, R., Schannwell, C., Ehlers, T. A., Gladstone, R., Pattyn, F., and Matsuoka, K.: Atmospheric and Oceanographic Signatures in the Ice Shelf Channel Morphology of Roi Baudouin Ice Shelf, East Antarctica, Inferred From Radar Data, Journal of Geophysical Research: Earth Surface, 125, https://doi.org/10.1029/2020JF005587, 2020.

Dutrieux, P., Vaughan, D. G., Corr, H. F. J., Jenkins, A., Holland, P. R., Joughin, I., and Fleming, A. H.: Pine Island glacier ice shelf melt distributed at kilometre scales, The Cryosphere, 7, 1543–1555, https://doi.org/10.5194/tc-7-1543-2013, 2013.

Dutrieux, P., Stewart, C., Jenkins, A., Nicholls, K. W., Corr, H. F. J., Rignot, E., and Steffen, K.: Basal terraces on melting ice shelves, Geophysical Research Letters, 41, 5506–5513, https://doi.org/10.1002/2014GL060618, 2014.

Favier, L., Jourdain, N. C., Jenkins, A., Merino, N., Durand, G., Gagliardini, O., Gillet-Chaulet, F., and Mathiot, P.: Assessment of sub-shelf melting parameterisations using the ocean–ice-sheet coupled model NEMO(v3.6)–Elmer/Ice(v8.3), Geoscientific Model Development, 12, 2255–2283, https://doi.org/10.5194/gmd-12-2255-2019, 2019.

Francis, D., Mattingly, K. S., Lhermitte, S., Temimi, M., and Heil, P.: Atmospheric extremes caused high oceanward sea surface slope triggering the biggest calving event in more than 50 years at the Amery Ice Shelf, The Cryosphere, 15, 2147–2165, https://doi.org/10.5194/tc-15-2147-2021, 2021.

Fretwell, P., Pritchard, H. D., Vaughan, D. G., Bamber, J. L., Barrand, N. E., Bell, R., Bianchi, C., Bingham, R. G., Blankenship, D. D., Casassa, G., Catania, G., Callens, D., Conway, H., Cook, A. J., Corr, H. F. J., Damaske, D., Damm, V., Ferraccioli, F., Forsberg, R., Fujita, S., Gim, Y., Gogineni, P., Griggs, J. A., Hindmarsh, R. C. A., Holmlund, P., Holt, J. W., Jacobel, R. W., Jenkins, A., Jokat, W., Jordan, T., King, E. C., Kohler, J., Krabill, W., Riger-Kusk, M., Langley, K. A., Leitchenkov, G., Leuschen, C., Luyendyk, B. P., Matsuoka, K., Mouginot, J., Nitsche, F. O., Nogi, Y., Nost, O. A., Popov, S. V., Rignot, E., Rippin, D. M., Rivera, A., Roberts, J., Ross, N., Siegert, M. J., Smith, A. M., Steinhage, D., Studinger, M., Sun, B., Tinto, B. K., Welch, B. C., Wilson, D., Young, D. A., Xiangbin, C., and Zirizzotti, A.: Bedmap2: improved ice bed, surface and thickness datasets for Antarctica, The Cryosphere, 7, 375–393, https://doi.org/10.519 4/tc-7-375-2013, 2013.

Fürst, J. J., Durand, G., Gillet-Chaulet, F., Tavard, L., Rankl, M., Braun, M., and Gagliardini, O.: The safety band of Antarctic ice shelves, Nature Climate Change, 6, 479–482, https://doi.org/10.1038/nclimate2912, 2016.

Gagliardini, O., Zwinger, T., Gillet-Chaulet, F., Durand, G., Favier, L., de Fleurian, B., Greve, R., Malinen, M., Martín, C., Råback, P., Ruokolainen, J., Sacchettini, M., Schäfer, M., Seddik, H., and Thies, J.: Capabilities and performance of Elmer/Ice, a new-generation ice sheet model, Geoscientific Model Development, 6, 1299–1318, https://doi.org/10.5194/gmd-6-1299-2013, 2013.

Gardner, A., Fahnestock, M., and Scambos., T.: MEaSUREs ITS_LIVE Regional Glacier and Ice Sheet Surface Velocities, Version 1, NASA National Snow and Ice Data Center Distributed Active Archive Center, https://doi.org/10.5067/6II6VW8LLWJ7, 2022.

Gladish, C. V., Holland, D. M., Holland, P. R., and Price, S. F.: Ice-shelf basal channels in a coupled ice/ocean model, Journal of Glaciology, 58, 1227–1244, https://doi.org/10.3189/2012JoG12J003, 2012.

Gorelick, N., Hancher, M., Dixon, M., Ilyushchenko, S., Thau, D., and Moore, R.: Google Earth Engine: Planetary-scale geospatial analysis for everyone, Remote Sensing of Environment, 202, 18–27, https://doi.org/10.1016/j.rse.2017.06.031, 2017.

Gourmelen, N., Goldberg, D. N., Snow, K., Henley, S. F., Bingham, R. G., Kimura, S., Hogg, A. E., Shepherd, A., Mouginot, J., Lenaerts, J. T. M., Ligtenberg, S. R. M., and Berg, W. J.: Channelized Melting Drives Thinning Under a Rapidly Melting Antarctic Ice Shelf, Geophysical Research Letters, 44, 9796–9804, https://doi.org/10.1002/2017GL074929, 2017.

Gourmelen, N., Escorihuela, M., Shepherd, A., Foresta, L., Muir, A., Garcia-Mondéjar, A., Roca, M., Baker, S., and Drinkwater, M.: CryoSat-2 swath interferometric altimetry for mapping ice elevation and elevation change, Advances in Space Research, 62, 1226–1242, https://doi.org/10.1016/j.asr.2017.11.014, 2018.

Gray, L., Burgess, D., Copland, L., Cullen, R., Galin, N., Hawley, R., and Helm, V.: Interferometric swath processing of Cryosat data for glacial ice topography, The Cryosphere, 7, 1857–1867, https://doi.org/10.519 4/tc-7-1857-2013, 2013.

Helm, V., Humbert, A., and Miller, H.: Elevation and elevation change of Greenland and Antarctica derived from CryoSat-2, The Cryosphere, 8, 1539–1559, https://doi.org/10.5194/tc-8-1539-2014, 2014.

Holland, P. R., Jenkins, A., and Holland, D. M.: Ice and ocean processes in the Bellingshausen Sea, Antarctica, Journal of Geophysical Research: Oceans, 115, 1–16, https://doi.org/10.1029/2008JC005219, 2010.

Howat, I., Porter, C., Noh, M.-J., Husby, E., Khuvis, S., Danish, E., Tomko, K., Gardiner, J., Negrete, A., Yadav, B., Klassen, J., Kelleher, C., Cloutier, M., Bakker, J., Enos, J., Arnold, G., Bauer, G., and Morin, P.: The Reference Elevation Model of Antarctica - Strips, Version 4.1, https://doi.org/10.7910/DVN/X7NDNY, 2022.

Howat, I. M., Porter, C., Smith, B. E., Noh, M.-J., and Morin, P.: The Reference Elevation Model of Antarctica, The Cryosphere, 13, 665–674, https://doi.org/10.5194/tc-13-665-2019, 2019.

Huguenin, M. F., Holmes, R. M., Spence, P., and England, M. H.: Subsurface Warming of the West Antarctic Continental Shelf Linked to El Niño-Southern Oscillation, Geophysical Research Letters, 51, https://doi.org/10.1029/2023GL104518, 2024.

Humbert, A., Christmann, J., Corr, H. F. J., Helm, V., Höyns, L.-S., Hofstede, C., Müller, R., Neckel, N., Nicholls, K. W., Schultz, T., Steinhage, D., Wolovick, M., and Zeising, O.: On the evolution of an ice shelf melt channel at the base of Filchner Ice Shelf, from observations and viscoelastic modeling, The Cryosphere, 16, 4107–4139, https://doi.org/10.5194/tc-16-4107-2022, 2022.

Hyogo, S., Nakayama, Y., and Mensah, V.: Modeling Ocean Circulation and Ice Shelf Melt in the Bellingshausen Sea, Journal of Geophysical Research: Oceans, 129, 1–19, https://doi.org/10.1029/2022JC019275, 2024.

IPCC: Climate Change 2021 – The Physical Science Basis, Cambridge University Press, https://doi.org/10.101 7/9781009157896, 2023.

Izeboud, M., Lhermitte, S., de Roda Husman, S., and Wouters, B.: Antarctic ice shelves vulnerable to damage in future climate warming, Nature Climate Change [in review], NCLIM-24010280-T, 2024.

Jacobs, S., Helmer, H., Doake, C. S. M., Jenkins, A., and Frolich, R. M.: Melting of ice shelves and the mass balance of Antarctica, Journal of Glaciology, 38, 375–387, https://doi.org/10.1017/S0022143000002252, 1992.

Jenkins, A. and Jacobs, S.: Circulation and melting beneath George VI Ice Shelf, Antarctica, Journal of Geophysical Research: Oceans, 113, 1–18, https://doi.org/10.1029/2007JC004449, 2008.

Jenkins, A., Dutrieux, P., Jacobs, S., Steig, E. J., Gudmundsson, G. H., Smith, J., and Heywood, K. J.: Decadal ocean forcing and Antarctic ice sheet response: Lessons from the Amundsen Sea, Oceanography, 29, 106–117, https://doi.org/10.5670/oceanog.2016.103, 2016.

Jenkins, A., Shoosmith, D., Dutrieux, P., Jacobs, S., Kim, T. W., Lee, S. H., Ha, H. K., and Stammerjohn, S.: West Antarctic Ice Sheet retreat in the Amundsen Sea driven by decadal oceanic variability, Nature Geoscience, 11, 733–738, https://doi.org/10.1038/s41561-018-0207-4, 2018.

Jesse, F., Lambert, E., and van de Wal, R.: Sub-shelf melt pattern; does detail matter?, in: Vienna, EGU General Assembly 2024, https://doi.org/10.5194/egusphere-egu24-5804, 2024.

Kalnay, E., Kanamitsu, M., Kistler, R., Collins, W., Deaven, D., Gandin, L., Iredell, M., Saha, S., White, G., Woollen, J., Zhu, Y., Leetmaa, A., Reynolds, R., Chelliah, M., Ebisuzaki, W., Higgins, W., Janowiak, J., Mo, K. C., Ropelewski, C., Wang, J., Jenne, R., and Joseph, D.: The NCEP/NCAR 40-Year Reanalysis Project, Bulletin of the American Meteorological Society, 77, 437–471, https://doi.org/10.1175/1520-0477(1996)077<0437:TNYRP>2.0.CO;2, 1996.

Lambert, E. and Burgard, C.: Brief Communication: Sensitivity of Antarctic ice-shelf melting to ocean warming across basal melt models, https://doi.org/10.5194/egusphere-2024-2358, 2024.

Lambert, E., Jüling, A., Wal, R. S. W. V. D., and Holland, P. R.: Modeling Antarctic ice shelf basal melt patterns using the one-Layer Antarctic model for Dynamical Downscaling of Ice – ocean Exchanges (LADDIE), The Cryosphere Discuss. [preprint], 2022, 1–39, https://doi.org/10.5194/tc-2022-225, 2022.

Lambert, E., Jüling, A., van de Wal, R. S. W., and Holland, P. R.: Modelling Antarctic ice shelf basal melt patterns using the one-layer Antarctic model for dynamical downscaling of ice–ocean exchanges (LADDIE v1.0), The Cryosphere, 17, 3203–3228, https://doi.org/10.5194/tc-17-3203-2023, 2023.

Lazeroms, W. M. J., Jenkins, A., Gudmundsson, G. H., and van de Wal, R. S. W.: Modelling present-day basal melt rates for Antarctic ice shelves using a parametrization of buoyant meltwater plumes, The Cryosphere, 12, 49–70, https://doi.org/10.5194/tc-12-49-2018, 2018.

Lhermitte, S., Sun, S., Shuman, C., Wouters, B., Pattyn, F., Wuite, J., Berthier, E., and Nagler, T.: Damage accelerates ice shelf instability and mass loss in Amundsen Sea Embayment, Proceedings of the National Academy of Sciences, 117, 24 735–24 741, https://doi.org/10.1073/pnas.1912890117, 2020.

Lilien, D. A., Joughin, I., Smith, B., and Shean, D. E.: Changes in flow of Crosson and Dotson ice shelves, West Antarctica, in response to elevated melt, The Cryosphere, 12, 1415–1431, https://doi.org/10.5194/tc-12-1415-2018, 2018.

Lindbäck, K., Moholdt, G., Nicholls, K. W., Hattermann, T., Pratap, B., Thamban, M., and Matsuoka, K.: Spatial and temporal variations in basal melting at Nivlisen ice shelf, East Antarctica, derived from phase-sensitive radars, The Cryosphere, 13, 2579–2595, https://doi.org/10.5194/tc-13-2579-2019, 2019.

Lomb, N. R.: Least-squares frequency analysis of unequally spaced data, Astrophysics and Space Science, 39, 447–462, https://doi.org/10.1007/BF00648343, 1976.

Mankoff, K. D., Jacobs, S. S., Tulaczyk, S. M., and Stammerjohn, S. E.: The role of Pine Island Glacier ice shelf basal channels in deep-water upwelling, polynyas and ocean circulation in Pine Island Bay, Antarctica, Annals of Glaciology, 53, 123–128, https://doi.org/10.3189/2012AoG60A062, 2012.

Matsuoka, K., Skoglund, A., Roth, G., de Pomereu, J., Griffiths, H., Headland, R., Herried, B., Katsumata, K., Le Brocq, A., Licht, K., Morgan, F., Neff, P. D., Ritz, C., Scheinert, M., Tamura, T., Van de Putte, A., van den Broeke, M., von Deschwanden, A., Deschamps-Berger, C., Van Liefferinge, B., Tronstad, S., and Melvær, Y.: Quantarctica, an integrated mapping environment for Antarctica, the Southern Ocean, and sub-Antarctic islands, Environmental Modelling & Software, 140, 105 015, https://doi.org/10.1016/j.envsoft.2021.105015, 2021.

Millan, R., Jager, E., Mouginot, J., Wood, M. H., Larsen, S. H., Mathiot, P., Jourdain, N. C., and Bjørk, A.: Rapid disintegration and weakening of ice shelves in North Greenland, Nature Communications, 14, 6914, https://doi.org/10.1038/s41467-023-42198-2, 2023.

Mobasher, M. E., Duddu, R., Bassis, J. N., and Waisman, H.: Modeling hydraulic fracture of glaciers using continuum damage mechanics, Journal of Glaciology, 62, 794–804, https://doi.org/10.1017/jog.2016.68, 2016.

Moholdt, G., Padman, L., and Fricker, H. A.: Basal mass budget of Ross and Filchner-Ronne ice shelves, Antarctica, derived from Lagrangian analysis of ICESat altimetry, Journal of Geophysical Research: Earth Surface, 119, 2361–2380, https://doi.org/10.1002/2014JF003171, 2014.

Morlighem, M.: MEaSUREs BedMachine Antarctica, Version 3 [Data Set]. Boulder, Colorado USA. NASA National Snow and Ice Data Center Distributed Active Archive Center., https://doi.org/https://doi.org/10.5067/FPSU0V1MWUB6, 2022.

Morlighem, M., Williams, C. N., Rignot, E., An, L., Arndt, J. E., Bamber, J. L., Catania, G., Chauché, N., Dowdeswell, J. A., Dorschel, B., Fenty, I., Hogan, K., Howat, I., Hubbard, A., Jakobsson, M., Jordan, T. M., Kjeldsen, K. K., Millan, R., Mayer, L., Mouginot, J., Noël, B. P., O'Cofaigh, C., Palmer, S., Rysgaard, S., Seroussi, H., Siegert, M. J., Slabon, P., Straneo, F., van den Broeke, M. R., Weinrebe, W., Wood, M., and Zinglersen, K. B.: BedMachine v3: Complete Bed Topography and Ocean Bathymetry Mapping of Greenland From Multibeam Echo Sounding Combined With Mass Conservation, Geophysical Research Letters, 44, 051–11, https://doi.org/10.1002/2017GL074954, 2017.

Morlighem, M., Rignot, E., Binder, T., Blankenship, D., Drews, R., Eagles, G., Eisen, O., Ferraccioli, F., Forsberg, R., Fretwell, P., Goel, V., Greenbaum, J. S., Gudmundsson, H., Guo, J., Helm, V., Hofstede, C., Howat, I., Humbert, A., Jokat, W., Karlsson, N. B., Lee, W. S., Matsuoka, K., Millan, R., Mouginot, J., Paden, J., Pattyn, F., Roberts, J., Rosier, S., Ruppel, A., Seroussi, H., Smith, E. C., Steinhage, D., Sun, B., Broeke, M. R. v. d., Ommen, T. D. v., Wessem, M. v., and Young, D. A.: Deep glacial troughs and stabilizing ridges unveiled beneath the margins of the Antarctic ice sheet, Nature Geoscience, 13, 132–137, https://doi.org/10.1038/s41561-019-0510-8, 2020.

Morlighem, M., Goldberg, D., Dias dos Santos, T., Lee, J., and Sagebaum, M.: Mapping the Sensitivity of the Amundsen Sea Embayment to Changes in External Forcings Using Automatic Differentiation, Geophysical Research Letters, 48, 1–8, https://doi.org/10.1029/2021GL095440, 2021.

Nakayama, Y., Menemenlis, D., Zhang, H., Schodlok, M., and Rignot, E.: Origin of Circumpolar Deep Water intruding onto the Amundsen and Bellingshausen Sea continental shelves, Nature Communications, 9, 1–9, https://doi.org/10.1038/s41467-018-05813-1, 2018.

Naughten, K. A., Holland, P. R., and De Rydt, J.: Unavoidable future increase in West Antarctic ice-shelf melting over the twenty-first century, Nature Climate Change, 13, 1222–1228, https://doi.org/10.1038/s41558-023-01818-x, 2023.

Nilsson, J., Gardner, A., Sandberg Sørensen, L., and Forsberg, R.: Improved retrieval of land ice topography from CryoSat-2 data and its impact for volume-change estimation of the Greenland Ice Sheet, The Cryosphere, 10, 2953–2969, https://doi.org/10.5194/tc-10-2953-2016, 2016.

Noble, T. L., Rohling, E. J., Aitken, A. R. A., Bostock, H. C., Chase, Z., Gomez, N., Jong, L. M., King, M. A., Mackintosh, A. N., McCormack, F. S., McKay, R. M., Menviel, L., Phipps, S. J., Weber, M. E., Fogwill, C. J., Gayen, B., Golledge, N. R., Gwyther, D. E., Hogg, A. M., Martos, Y. M., Pena-Molino, B., Roberts, J., Flierdt, T., and Williams, T.: The Sensitivity of the Antarctic Ice Sheet to a Changing Climate: Past, Present, and Future, Reviews of Geophysics, 58, 1–89, https://doi.org/10.1029/2019RG000663, 2020.

Noël, B., van Wessem, J. M., Wouters, B., Trusel, L., Lhermitte, S., and van den Broeke, M. R.: Higher Antarctic ice sheet accumulation and surface melt rates revealed at 2 km resolution, Nature Communications, 14, 7949, https://doi.org/10.1038/s41467-023-43584-6, 2023.

Paolo, F. S., Padman, L., Fricker, H. A., Adusumilli, S., Howard, S., and Siegfried, M. R.: Response of Pacific-sector Antarctic ice shelves to the El Niño/Southern Oscillation, Nature Geoscience, 11, 121–126, https://doi.org/10.1038/s41561-017-0033-0, 2018.

Park, T., Nakayama, Y., and Nam, S.: Amundsen Sea circulation controls bottom upwelling and Antarctic Pine Island and Thwaites ice shelf melting, Nature Communications, 15, 2946, https://doi.org/10.1038/s41467-024-47084-z, 2024.

Pattyn, F. and Morlighem, M.: The uncertain future of the Antarctic Ice Sheet, Science, 367, 1331–1335, https://doi.org/10.1126/science.aaz5487, 2020.

Pattyn, F., Ritz, C., Hanna, E., Asay-Davis, X., DeConto, R., Durand, G., Favier, L., Fettweis, X., Goelzer, H., Golledge, N. R., Kuipers Munneke, P., Lenaerts, J. T. M., Nowicki, S., Payne, A. J., Robinson, A., Seroussi, H., Trusel, L. D., and van den Broeke, M.: The Greenland and Antarctic ice sheets under 1.5 °C global warming, Nature Climate Change, 8, 1053–1061, https://doi.org/10.1038/s41558-018-0305-8, 2018.

Pavlis, N. K., Holmes, S. A., Kenyon, S. C., and Factor, J. K.: The development and evaluation of the Earth Gravitational Model 2008 (EGM2008), Journal of Geophysical Research: Solid Earth, 117, n/a–n/a, https://doi.org/10.1029/2011JB008916, 2012.

Pritchard, H. D., Ligtenberg, S. R. M., Fricker, H. A., Vaughan, D. G., van den Broeke, M. R., and Padman, L.: Antarctic ice-sheet loss driven by basal melting of ice shelves, Nature, 484, 502–505, https://doi.org/10.1038/nature10968, 2012.

Reed, B., Green, J. A. M., Jenkins, A., and Gudmundsson, G. H.: Recent irreversible retreat phase of Pine Island Glacier, Nature Climate Change, 14, 75–81, https://doi.org/10.1038/s41558-023-01887-y, 2024.

Rignot, E., Jacobs, S., Mouginot, J., and Scheuchl, B.: Ice-shelf melting around antarctica, Science, 341, 266–270, https://doi.org/10.1126/science.1235798, 2013.

Ritz, C., Edwards, T. L., Durand, G., Payne, A. J., Peyaud, V., and Hindmarsh, R. C. A.: Potential sea-level rise from Antarctic ice-sheet instability constrained by observations, Nature, 528, 115–118, https://doi.org/10.1038/nature16147, 2015.

Roberts, J., Galton-Fenzi, B. K., Paolo, F. S., Donnelly, C., Gwyther, D. E., Padman, L., Young, D., Warner, R., Greenbaum, J., Fricker, H. A., Payne, A. J., Cornford, S., Le Brocq, A., van Ommen, T., Blankenship, D., and Siegert, M. J.: Ocean forced variability of Totten Glacier mass loss, Geological Society, London, Special Publications, 461, 175–186, https://doi.org/10.1144/SP461.6, 2018.

Scambos, T., Fricker, H. A., Liu, C.-C., Bohlander, J., Fastook, J., Sargent, A., Massom, R., and Wu, A.-M.: Ice shelf disintegration by plate bending and hydro-fracture: Satellite observations and model results of the 2008 Wilkins ice shelf break-ups, Earth and Planetary Science Letters, 280, 51–60, https://doi.org/10.1016/j.epsl.2008.12.027, 2009.

Scargle, J. D.: Studies in astronomical time series analysis. II - Statistical aspects of spectral analysis of unevenly spaced data, The Astrophysical Journal, 263, 835–853, https://doi.org/10.1086/160554, 1982.

Schmidt, B. E., Washam, P., Davis, P. E., Nicholls, K. W., Holland, D. M., Lawrence, J. D., Riverman, K. L., Smith, J. A., Spears, A., Dichek, D. J., Mullen, A. D., Clyne, E., Yeager, B., Anker, P., Meister, M. R., Hurwitz, B. C., Quartini, E. S., Bryson, F. E., Basinski-Ferris, A., Thomas, C., Wake, J., Vaughan, D. G., Anandakrishnan, S., Rignot, E., Paden, J., and Makinson, K.: Heterogeneous melting near the Thwaites Glacier grounding line, Nature, 614, 471–478, https://doi.org/10.1038/s41586-022-05691-0, 2023.

Schoof, C.: Ice sheet grounding line dynamics: Steady states, stability, and hysteresis, Journal of Geophysical Research, 112, F03S28, https://doi.org/10.1029/2006JF000664, 2007.

Sergienko, O. V.: Basal channels on ice shelves, Journal of Geophysical Research: Earth Surface, 118, 1342–1355, https://doi.org/10.1002/jgrf.20105, 2013.

Seroussi, H., Nowicki, S., Payne, A. J., Goelzer, H., Lipscomb, W. H., Abe-Ouchi, A., Agosta, C., Albrecht, T., Asay-Davis, X., Barthel, A., Calov, R., Cullather, R., Dumas, C., Galton-Fenzi, B. K., Gladstone, R., Golledge, N. R., Gregory, J. M., Greve, R., Hattermann, T., Hoffman, M. J., Humbert, A., Huybrechts, P., Jourdain, N. C., Kleiner, T., Larour, E., Leguy, G. R., Lowry, D. P., Little, C. M., Morlighem, M., Pattyn, F., Pelle, T., Price, S. F., Quiquet, A., Reese, R., Schlegel, N.-J., Shepherd, A., Simon, E., Smith, R. S., Straneo, F., Sun, S., Trusel, L. D., Van Breedam, J., van de Wal, R. S. W., Winkelmann, R., Zhao, C., Zhang, T., and Zwinger, T.: ISMIP6 Antarctica: a multi-model ensemble of the Antarctic ice sheet evolution over the 21st century, The Cryosphere, 14, 3033–3070, https://doi.org/10.5194/tc-14-3033-2020, 2020.

Shean, D. E., Joughin, I. R., Dutrieux, P., Smith, B. E., and Berthier, E.: Ice shelf basal melt rates from a high-resolution digital elevation model (DEM) record for Pine Island Glacier, Antarctica, The Cryosphere, 13, 2633–2656, https://doi.org/10.5194/tc-13-2633-2019, 2019.

Silvano, A., Rintoul, S., and Herraiz-Borreguero, L.: Ocean-Ice Shelf Interaction in East Antarctica, Oceanography, 29, 130–143, https://doi.org/10.5670/oceanog.2016.105, 2016.

Smith, J. A., Bentley, M. J., Hodgson, D. A., and Cook, A. J.: George VI Ice Shelf: past history, present behaviour and potential mechanisms for future collapse, Antarctic Science, 19, 131–142, https://doi.org/10.1017/S0954102007000193, 2007.

Stanton, T. P., Shaw, W. J., Truffer, M., Corr, H. F. J., Peters, L. E., Riverman, K. L., Bindschadler, R., Holland, D. M., and Anandakrishnan, S.: Channelized ice melting in the ocean boundary layer beneath Pine Island Glacier, Antarctica., Science (New York, N.Y.), 341, 1236–9, https://doi.org/10.1126/science.1239373, 2013.

Sun, S. and Gudmundsson, G. H.: The speedup of Pine Island Ice Shelf between 2017 and 2020: reevaluating the importance of ice damage, Journal of Glaciology, pp. 1–9, https://doi.org/10.1017/jog.2023.76, 2023.

Sun, S., Cornford, S. L., Moore, J. C., Gladstone, R., and Zhao, L.: Ice shelf fracture parameterization in an ice sheet model, The Cryosphere, 11, 2543–2554, https://doi.org/10.5194/tc-11-2543-2017, 2017.

Trusel, L. D., Pan, Z., and Moussavi, M.: Repeated Tidally Induced Hydrofracture of a Supraglacial Lake at the Amery Ice Shelf Grounding Zone, Geophysical Research Letters, 49, 1–11, https://doi.org/10.1029/2021 GL095661, 2022.

van de Wal, R. S. W., Nicholls, R. J., Behar, D., McInnes, K., Stammer, D., Lowe, J. A., Church, J. A., DeConto, R., Fettweis, X., Goelzer, H., Haasnoot, M., Haigh, I. D., Hinkel, J., Horton, B. P., James, T. S., Jenkins, A., LeCozannet, G., Levermann, A., Lipscomb, W. H., Marzeion, B., Pattyn, F., Payne, A. J., Pfeffer, W. T., Price, S. F., Seroussi, H., Sun, S., Veatch, W., and White, K.: A High-End Estimate of Sea Level Rise for Practitioners, Earth's Future, 10, 1–24, https://doi.org/10.1029/2022EF002751, 2022.

van Wessem, J. M., van de Berg, W. J., Noël, B. P. Y., van Meijgaard, E., Amory, C., Birnbaum, G., Jakobs, C. L., Krüger, K., Lenaerts, J. T. M., Lhermitte, S., Ligtenberg, S. R. M., Medley, B., Reijmer, C. H., van Tricht, K., Trusel, L. D., van Ulft, L. H., Wouters, B., Wuite, J., and van den Broeke, M. R.: Modelling the climate and surface mass balance of polar ice sheets using RACMO2 – Part 2: Antarctica (1979–2016), The Cryosphere, 12, 1479–1498, https://doi.org/10.5194/tc-12-1479-2018, 2018.

van Wessem, J. M., van den Broeke, M. R., Wouters, B., and Lhermitte, S.: Variable temperature thresholds of melt pond formation on Antarctic ice shelves, Nature Climate Change, 13, 161–166, https://doi.org/10.1038/s41558-022-01577-1, 2023.

van Westen, R. M. and Dijkstra, H. A.: Ocean eddies strongly affect global mean sea-level projections, Science Advances, 7, 1–11, https://doi.org/10.1126/sciadv.abf1674, 2021.

Vaughan, D. G., Corr, H. F. J., Bindschadler, R. A., Dutrieux, P., Gudmundsson, G. H., Jenkins, A., Newman, T., Vornberger, P., and Wingham, D. J.: Subglacial melt channels and fracture in the floating part of Pine Island Glacier, Antarctica, Journal of Geophysical Research: Earth Surface, 117, 1–10, https://doi.org/10.1029/2012JF002360, 2012.

Vaňková, I. and Nicholls, K. W.: Ocean Variability Beneath the Filchner-Ronne Ice Shelf Inferred From Basal Melt Rate Time Series, Journal of Geophysical Research: Oceans, 127, 1–20, https://doi.org/10.1029/2022 JC018879, 2022.

Veldhuijsen, S. B. M., van de Berg, W. J., Brils, M., Kuipers Munneke, P., and van den Broeke, M. R.: Characteristics of the 1979–2020 Antarctic firn layer simulated with IMAU-FDM v1.2A, The Cryosphere, 17, 1675–1696, https://doi.org/10.5194/tc-17-1675-2023, 2023.

Wåhlin, A., Alley, K. E., Begeman, C., Hegrenæs, , Yuan, X., Graham, A. G. C., Hogan, K., Davis, P. E. D., Dotto, T. S., Eayrs, C., Hall, R. A., Holland, D. M., Kim, T. W., Larter, R. D., Ling, L., Muto, A., Pettit, E. C., Schmidt, B. E., Snow, T., Stedt, F., Washam, P. M., Wahlgren, S., Wild, C., Wellner, J., Zheng, Y., and Heywood, K. J.: Swirls and scoops: Ice base melt revealed by multibeam imagery of an Antarctic ice shelf, Science Advances, 10, 1–14, https://doi.org/10.1126/sciadv.adn9188, 2024.

Walker, C. and Gardner, A.: Evolution of ice shelf rifts: Implications for formation mechanics and morphological controls, Earth and Planetary Science Letters, 526, 115 764, https://doi.org/10.1016/j.epsl.2019.115764, 2019.

Watkins, R. H., Bassis, J. N., and Thouless, M. D.: Roughness of Ice Shelves Is Correlated With Basal Melt Rates, Geophysical Research Letters, 48, 1–8, https://doi.org/10.1029/2021GL094743, 2021.

Wearing, M. G., Stevens, L. A., Dutrieux, P., and Kingslake, J.: Ice-Shelf Basal Melt Channels Stabilized by Secondary Flow, Geophysical Research Letters, 48, 1–11, https://doi.org/10.1029/2021GL094872, 2021.

Wingham, D., Francis, C., Baker, S., Bouzinac, C., Brockley, D., Cullen, R., de Chateau-Thierry, P., Laxon, S., Mallow, U., Mavrocordatos, C., Phalippou, L., Ratier, G., Rey, L., Rostan, F., Viau, P., and Wallis, D.: CryoSat: A mission to determine the fluctuations in Earth's land and marine ice fields, Advances in Space Research, 37, 841–871, https://doi.org/10.1016/j.asr.2005.07.027, 2006.

Winstrup, M., Ranndal, H., Hillerup Larsen, S., Simonsen, S. B., Mankoff, K. D., Fausto, R. S., and Sandberg Sørensen, L.: PRODEM: an annual series of summer DEMs (2019 through 2022) of the marginal areas of the Greenland Ice Sheet, Earth System Science Data, 16, 5405–5428, https://doi.org/10.5194/essd-16-5405-2024, 2024.

Wunsch, C.: Bermuda sea level in relation to tides, weather, and baroclinic fluctuations, Reviews of Geophysics, 10, 1–49, https://doi.org/10.1029/RG010i001p00001, 1972.

Yang, H. W., Kim, T.-W., Dutrieux, P., Wåhlin, A. K., Jenkins, A., Ha, H. K., Kim, C. S., Cho, K.-H., Park, T., Lee, S. H., and Cho, Y.-K.: Seasonal variability of ocean circulation near the Dotson Ice Shelf, Antarctica, Nature Communications, 13, 1138, https://doi.org/10.1038/s41467-022-28751-5, 2022.

Zinck, A.-S.: BURGEE, GitHub [code], URL https://github.com/aszinck/BURGEE, 2023.

Zinck, A.-S, Lhermitte, S., Wearing, M., and Wouters, B.: Dataset belonging to the article: Exposure to Underestimated Channelized Melt in Antarctic Ice Shelves, https://doi.org/10.4121/4e2ba9a9-7b1b-4837-b 52d-036f8c876e67, 2024a.

Zinck, A.-S., Lhermitte, S., Wearing, M., and Wouters, B.: Exposure to Underestimated Channelized Melt in Antarctic Ice Shelves, Nature Climate Change [in review], NCLIM-24071992, pp. 0–26, https://doi.org/ 10.21203/rs.3.rs-4806463/v1, 2024b.

Zinck, A.-s. P. and Grinsted, A.: Brief communication: Estimating the ice thickness of the Müller Ice Cap to support selection of a drill site, The Cryosphere, 16, 1399–1407, https://doi.org/10.5194/tc-16-1399-2022, 2022.

Zinck, A.-S. P., Wouters, B., Lambert, E., and Lhermitte, S.: Unveiling spatial variability within the Dotson Melt Channel through high-resolution basal melt rates from the Reference Elevation Model of Antarctica, The Cryosphere, 17, 3785–3801, https://doi.org/10.5194/tc-17-3785-2023, 2023.

Acknowledgments

A PhD defense can be rather boring – especially if you are not that familiar with the topic. I have, therefore, prepared something for all of you who might find it a rather long hour of questions. In the little word puzzle below, I hope to have captured everyone who has made the past four years memorable to me.

Thank you to:

ALASKA	BEER	BERT	COLLEAGUES
COMMITTEE	DEMI	EGU	FAMILY
FRIENDS	GRS	HIRISE	HOEMBA
IMAU	PARANYMPHS	PSG	PUCK
RRD	STEF	TINDER	WIFE

P	U	C	K	U	Y	H	A	I	C	H	S
S	E	I	R	L	O	X	B	O	U	I	H
T	N	T	I	E	C	M	L	E	I	R	P
E	I	M	M	M	W	L	G	J	Y	I	M
F	A	B	Z	Y	E	P	L	N	B	S	Y
F	A	A	L	A	S	K	A	R	E	E	N
B	O	U	G	U	A	M	I	V	R	Y	A
D	E	U	Z	Z	I	F	Y	W	T	D	R
G	E	E	T	T	I	M	M	O	C	E	A
S	R	G	R	E	U	K	E	P	R	F	P
W	S	S	R	E	G	R	E	D	N	I	T
P	G	F	R	I	E	N	D	S	V	W	X

ALASKA: To all the people who joined or organized the International Summer School in Glaciology in McCarthy, Alaska in 2022. A special thank you to Morag and Johanna for a wonderful road trip in Alaska after the summer school.

BEER: No need to say more.

BERT: For the numerous hours of supervision and for always remembering my birthday.

COLLEAGUES: See IMAU, GRS, PSG, and HIRISE.

COMMITTEE: For being in my PhD committee and for reading my thesis.

DEMI: For being my personal social worker, coach, supporter, comfort, and many more things. Thank you for always being there for me. (See WIFE)

EGU: To the entire European Geoscience Union (EGU) Cryopheric Division (CR) Early Career Scientist (ECS) team for supporting me in my time as ECS (co-)representative.

FAMILY: To my family in Denmark for always being supportive and to my family-in-law for welcoming me into the family. An extra special thank you to Muddi for just being Muddi.

FRIENDS: You most likely belong to one of the other categories as well. And if not - thank you!

GRS: To the entire Geoscience and Remote Sensing Department and for your willingness to change for the better through more inclusion. A special thank you to the entire PhD/PostDoc community.

HIRISE: To the entire team HiRISE in both the Netherlands and Belgium for fostering a small ice shelf community with journal clubs, knowledge exchange and collaborations. A huge thank you as well to the semi-HiRISE people such as my lovely old office mate Maaike.

HOEMBA: To the wonderful Ice and Climate PhD support group at IMAU for both hour regular support meetings, but especially also for the numerous social activities.

IMAU:	To everybody at IMAU for welcoming me when I just moved to the Nehterlands and especially to the Ice and Climate group for fostering an inclusive working environment with weekly group meetings.
PARANYMPHS:	Raise your glass for Tim and Franka! Thank you both for a lot of good memories in the past four years including beer, patatje oorlog, Foute Feestjes, beer, for organizing my bachelorette party and for being so much more than just colleagues.
PSG:	To the Physical and Space Geodesy section for the past two years of section meetings.
PUCK:	For being the best cat in the world and for choosing me as your favorite human.
RRD:	To all the people at Rotterdam Roller Derby for being my mental break from work.
STEF:	For many hours of supervision and for encouraging me to aim higher.
TINDER:	For allowing me to find my wife and for giving me and Tim many good hours of Tinder-gossiping.
WIFE:	For everything! I am very grateful for everything you do for me and especially for you moving to Copenhagen with me.

List of Publications

First Author, Peer Reviewed:

Zinck, A.-S. P., Wouters, B., Lambert, E., and Lhermitte, S.: Unveiling spatial variability within the Dotson Melt Channel through high-resolution basal melt rates from the Reference Elevation Model of Antarctica, The Cryosphere, 17, 3785–3801, `https://doi.org/10.5194/tc-17-3785-2023`, 2023.

Zinck, A.-S. P. and Grinsted, A.: Brief communication: Estimating the ice thickness of the Müller Ice Cap to support selection of a drill site, The Cryosphere, 16, 1399–1407, `https://doi.org/10.5194/tc-16-1399-2022`, 2022.

First Author, In Review:

Zinck, A.-S., Lhermitte, S., Wearing, M., and Wouters, B.: Exposure to Underestimated Channelized Melt in Antarctic Ice Shelves, Nature Climate Change [in review], NCLIM-24071992, `https://doi.org/10.21203/rs.3.rs-4806463/v1`, 2024.

Zinck, A.-S. P., Wouters, B., Jesse, F., and Lhermitte, S.: Ocean-Induced Weakening of George VI Ice Shelf, EGUsphere [preprint], `https://doi.org/10.5194/egusphere-2025-573`, 2025.

Co-Author, Peer Reviewed:

Alerskans, E., Zinck, A.-S. P., Nielsen-Englyst, P., and Høyer, J. L.: Exploring machine learning techniques to retrieve sea surface temperatures from passive microwave measurements, Remote Sensing of Environment, Volume 281, 113220, ISSN 0034-4257, `https://doi.org/10.1016/j.rse.2022.113220`, 2022.

List of Presentations

Oral presentations:

Joint IAPSO/IACS Commission on Ice-Ocean Interactions (JCIOI) workshop *(invited)*, 2024, online.

British Antarctic Survey (BAS) - The Netherlands (NL) Science Days, 2024, Cambridge, England.

Forum for Research into Ice Shelf Processes (FRISP), 2024, Bremerhaven, Germany.

European Geosciences Union (EGU) General Assembly, 2024, Vienna, Austria.

Nederlands Aardwetenschappelijk Congres (NAC), 2023, Utrecht, The Netherlands.

Internatiol Glaciological Society (IGS) Global Seminar *(invited)*, 2023, online.

Buys Ballot Research School (BBOS) Autumn Symposium, 2022, Heerenveen, The Netherlands.

European Geosciences Union (EGU) General Assembly, 2022, Vienna, Austria.

European Geosciences Union (EGU) General Assembly, 2021, Online.

Poster presentations:

European Polar Science Week, 2024, Copenhagen, Denmark.

Forum for Research into Ice Shelf Processes (FRISP), 2023, Stalheim, Norway.

American Geophysical Union (AGU) Fall Meeting, 2021, online.

Buys Ballot Research School (BBOS) Autumn Symposium, 2021, Soesterberg, The Netherlands.

Curriculum Vitae

Ann-Sofie Priergaard Zinck

1994-04-18	Born in Odense (Denmark)
2010 - 2013	Tornbjerg Gymnasium, Odense, Denmark
2014 - 2017	Bachelor of Science in Physics, Niels Bohr Insitute, University of Copenhagen, Denmark Bachelor thesis title: *Greenland Ice Sheet Evolution and Contribution to Sea Level*
2017	Semester abroad, Arctic Geophysics, University Centre in Svalbard (UNIS), Svalbard, Norway
2018 - 2020	Master of Science in Physics with specialization in Geophysics, Niels Bohr Insitute, University of Copenhagen, Denmark Master thesis title: *Surface velocity and ice thickness of the Müller Ice Cap, Axel Heiberg Island*
2018	Student Research Assistant in oceanography, Danish Meteorological Institute, Denmark
2020 - 2021	Research Assistant at Physics of Ice, Climate, and Earth (PICE), Niels Bohr Insitute, University of Copenhagen, Denmark
2021 - 2025	PhD 2021 - 2022: Institute for Marine and Atmospheric research Utrecht (IMAU), Utrecht University, The Netherlands 2023 - 2025: Department of Geoscience and Remote Sensing, Delft University of Technology, The Netherlands Thesis title: *Revealing hidden patterns -A study on ice shelf basal melting*